Development and performance assessment of a Plasma Focus electron beam generator for Intra-Operative Radiation Therapy

Presentata da: Elisa Ceccolini

Coordinatore Dottorato:
Prof. Antonio Barletta

Relatore:
Prof. Domiziano Mostacci

Contents

Preface

The Plasma Focus is a device designed to generate a plasma sheet between two coaxial electrodes by means of a high voltage difference. The energy of a capacitor bank (between a few and a few tens of kilojoule) is instantly transferred to the electrodes producing a plasma sheet which is then pushed toward the open end of the electrodes by $\vec{J} \times \vec{B}$ force. The sheet implodes into a very dense magnetized plasma pinch. The pinched plasma may reach temperatures of several tens of keV and thermo-nuclear reactions may take place and charged particles be emitted.

The charged particles emission has two main components: an ion beam peaked forward and an electron beam directed backward.

For this project, it was thought to use the electron beam to produce x-rays by interaction with appropriate targets (through bremsstrahlung and characteristic emission) for medical applications.

A characteristic of the dense plasma focus is that even the smallest device has essentially the same behavior as the larger machines, producing the same plasma characteristics and the same radiation products and characteristics. This stimulated the idea on small table-top-sized plasma focus machines that do not require large facilities, and thus could be used for IntraOperative RadioTherapy (IORT), that would so became available in every operating room.

A dedicated Plasma Focus device has been designed, put in operation and tested by the research groups of the University of Bologna and of the University of Ferrara, coordinated by the Alma Mater s.r.l. of the University of Bologna, and with the financial support of ABO Project (Applicazione delle Biotecnologie in Oncologia, Biotechnology Applications for Oncology).

The pulse properties of plasma accelerated beams differ significantly from those commonly provided by medical accelerators in pulse duration and peak current, and correspondingly pulse dose rate and energy spectrum. Thus, among obvious properties such as operational stability, a reliable physical and dosimetric characterization of plasma focus accelerated particle beams has to be established.

The very high dose rate (several Gy per discharge less than 1 microsecond) is a peculiarity of this device that has to be investigated, as it can modify the relative biological effectiveness (RBE).

The RBE is a number that expresses the relative amount of damage, as compared to a

standard, that a fixed absorbed dose of ionizing radiation of a given type can produce in biological tissues. The higher that number, the more damaging the type of radiation, for the same amount of absorbed energy.

The biological effectiveness of Plasma Focus accelerated particles has to be determined and compared to that for established particle sources before starting any medical application. This task requires a sequence of extensive experiments, starting with systematic cell irradiation.

Aim of this Ph.D. project was to investigate the main physical properties of the low-energy x-ray beams produced by a Plasma Focus device and their potential medical applications to IORT treatments.

It was necessary to develop the optimal geometrical configuration; to evaluate the x-rays produced and their dose deposited; to estimate the energy electron spectrum produced in the "pinch phase"; to study an optimal target for the conversion of the x-rays; to conduct simulations to study the physics involved; and in order to evaluate the radio-biological features of the beam, cell holders had to be developed for both irradiations and cell growth conditions.

All of the above issues have been dealt with the present Ph.D. project, and the methods, procedures and results will be presented in the chapters to follow.

Chapter 1

Plasma Focus device

Over the past several decades, a particular class of dense magnetised plasmas has been produced by a device generally known as Dense Plasma Focus. It is a device in which plasmas can be generated, accelerated, compressed and confined.

Plasma Focus machines are able to produce pulsed electrical discharges in gases in which microinstabilities and turbulence lead to the generation of powerful beams of electrons and ions and to the emission of a large quantity of x-rays; and, when the filling gas is deuterium, also to the generation of fusion neutrons and protons.

1.1 Principles and general aspects

Two different chamber designs were developed independently by Filippov in the Soviet Union and Mather in the United States [1]. In the Mather configuration the symmetry axis of the device coincides with the axis of macroscopic motion of the plasma, while in the Filippov concept the symmetry axis is perpendicular to the axis of the macroscopic motion (Fig. 1.1).

The Plasma Focus device of Montecuccolino, named PFMA-3, is of the Mather type.
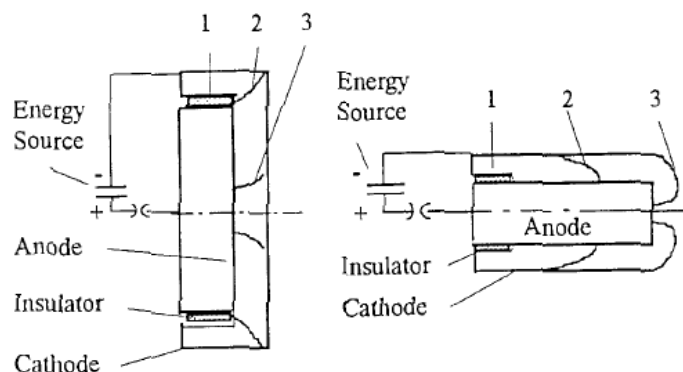
Figure 1.1 Left: Filippov design; righ: Mather design
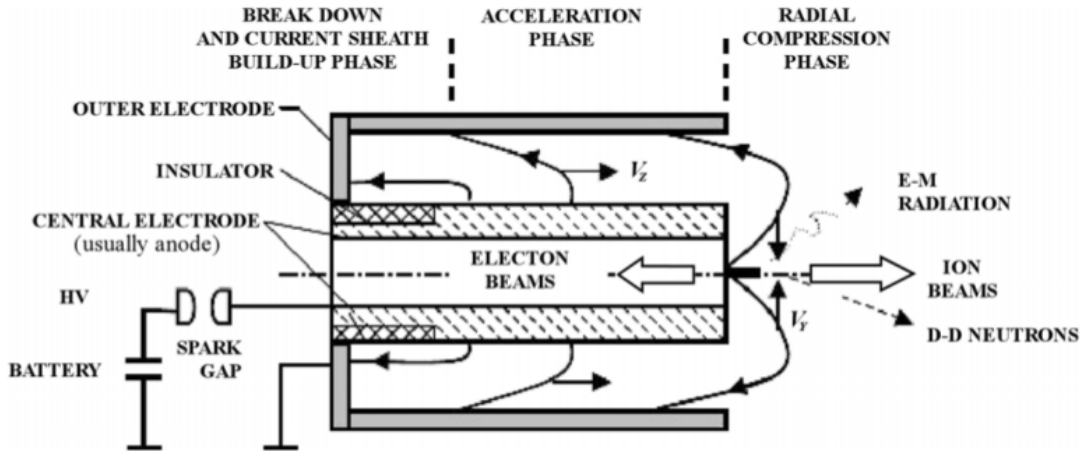
Figure 1.2   Plasma focus discharge described in four phases

A Mather type Plasma Focus is made of two cylindrical electrodes, closed at one end and open at the other. An insulating sleeve is placed around the base of the inner electrode. These electrodes are connected at the closed end, through a high-speed, high-current switch (usually of a spark gap type), to a capacitor bank where energy is stored. The electrodes are contained in a vacuum chamber filled with a few Torrs of a gas, chosen according to the purpose intended. For example: Hydrogen, Deuterium, Tritium, Argon, Neon, other pure gases and gas mixtures have been used [2, 3].

1.1.1   The four phases of Plasma Focus discharge

The Plasma Focus dynamics can be ideally separated in four main phases, (figure 1.2) [4].

- breakdown phase ($\sim 300\,\mathrm{ns}$)
- acceleration phase ($\sim 2 \div 3\,\mathrm{\mu s}$)
- compression phase ($\sim 2 \div 3\,\mathrm{ns}$)
- expansion phase

As soon as the spark-gap is triggered closing the circuit, an electrical discharge through the filling gas develops. The seed electrons present between the electrodes in the vacuum chamber are accelerated by the electric field, which is strongly enhanced by the presence of the insulator sleeve and by the cathode edge.

Once the ionization energy of the background gas is reached, multiple ionization avalanches make the free charge grow exponentially producing the electrical breakdown of the gas (*breakdown phase*); in a very short time (microsecond order of magnitude) the energy stored in the capacitor bank is discharged to the electrodes. The gas that fills the gap between inner and outer electrodes ionizes and forms a plasma, [5].

The electric field between the two electrodes is distorted due to the insulator sleeve and

the net effect are a current of ions moving towards the open end of the electrodes and a current of fast electrons moving towards the closed ends of the electrodes.

The macroscopic flow of charges connects the electrodes providing a low resistance path for the current flowing from the capacitor bank to the ground of the system.

The ionic current generates a poloidal magnetic field (Faraday-Neumann-Lenz-Henry Law) which, combined with the electric field, produces a $\vec{J} \times \vec{B}$ force that simultaneously moves the plasma towards the electrode open end and compresses it (magnetic pressure) on the surface of the inner electrode.

As soon as the current sheet is formed and carries the circuit current, the plasma detaches from the insulator and grows in size; its profile develops in a parabolic shape due to the dependence of the magnetic pressure from the radial position. The sheath is then pushed towards the open end of the electrodes (*acceleration phase*).

During this phase, the motion of the current sheet is characterized by a roughly constant axial velocity (about 10^7 cm/sec): the sheath sweeps the background neutral gas it meets and grows in density, but also looses part of the plasma in the region where its tail connects to the outer electrode.

As the open end of the electrodes is reached, the sheath is driven to collapse towards the symmetry axis (*collapse phase* or *pinch phase*). The current profile accelerates; the inductance grows rapidly lowering the peak current.

When the plasma sheath reaches the open end of the inner electrodes, it is very rapidly compressed radially upon itself by a pinching mechanism, the electromagnetic fields confining it in a small region (from about $1 \, mm^3$ to a few cubic centimeters in volume) usually named *focus*, in which fusion reactions may occur depending on the filling gas mixture. To maximize the compression effect of the pinching mechanism, this should coincide in time with the first maximum of the current. The gas trapped in the focus is estimated to be about 10% of that originally there.

After a very short time MHD instabilities (usually of mode $m = 0$, sausage, or $m = 1$, kink) destroy the confinement of the plasma, interrupting the life of the plasma itself (*expansion phase*).

The dynamics of the sheath is strictly related to the circuit discharge, since the evolution of the plasma modifies the inductance parameter of the equivalent circuit. The maximum of energy conversion is obtained if there is coincidence between the peak current and the radial collapse into the focus.

Typical time for the duration of the whole phenomena are of the order of a few microseconds.

1.1.2   RLC circuit

As in many pulsed electrical power systems, the equivalent circuit diagram of the plasma focus system is very simple, although the actual physical hardware is quite complex. Fig. 1.3 shows the equivalent circuit of the plasma focus device [1].
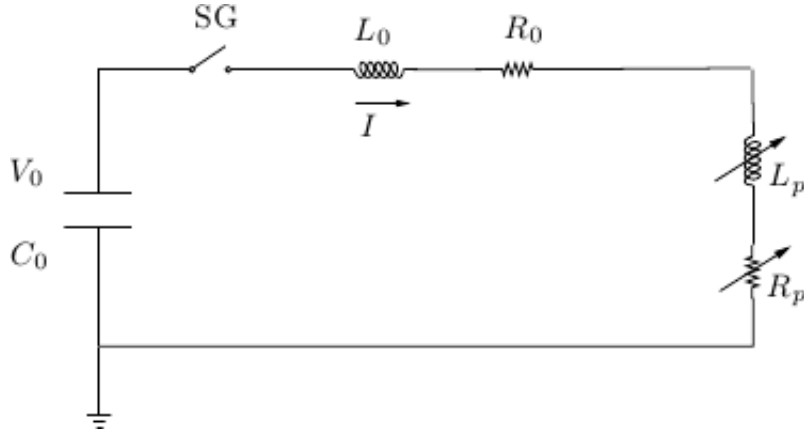
Figure 1.3   Equivalent electrical circuit of plasma focus discharge

The subscript "o" denote the initial values of various circuit parameters established by the choice of hardware design of capacitors, switches, inductance, and the initial charge voltage. The effect of the plasma discharge in the circuit can be characterized by the combination of a time varying inductance (L_P) and the time varying resistance (R_P). The plasma resistance can usually be neglected with respect to the external one. Neglecting the plasma resistance $R_P(t)$, the equation describing the lumped RLC circuit is

$$\frac{d}{dt}((L_0 + L_P(t))I) + R_0 I = V_0 - \frac{1}{C_0}\int_0^t I(t')dt' \tag{1.1}$$

assuming also (L_P) constant in time, the equation can be easily solved by means of Laplace transforms. Usually, the Plasma Focus device equivalent RLC circuit is strongly underdamped, that means $R_0 \ll 2\sqrt{\frac{L}{C_0}}$ with $L = L_0 + L_P$ the total inductance.
The typical current waveform of a Plasma Focus device in a short circuit test is, indeed, an exponentially damped sinusoid as obtainable by solving equation 1.1:

$$I(t) = \frac{V_0}{\omega L}exp(-\zeta t)\sin(\omega t) \tag{1.2}$$

where,

$$\zeta = \frac{R_0}{2L} \qquad \omega \simeq \frac{1}{\sqrt{LC_0}} \tag{1.3}$$

From the capacitor laws, under the simplifying hypothesis $R_0 \ll 2\sqrt{\frac{L}{C_0}}$ (equivalent to $\frac{\zeta}{\omega} \ll 1$), the voltage drop over the plasma is:

$$V(t) = V_0 exp\left(-\frac{R_0}{2L}t\right)\cos\left(\frac{t}{\sqrt{LC_0}}\right) \tag{1.4}$$

It is now well understood that only part of the total energy actually goes into the plasma pinch. The most widely used instrumentation involved with measurements of electrical quantities in Plasma Focus devices are high voltage probes and Rogowski coils. High

voltage probes are used for measuring the time evolution in the voltage during the discharge, at a given point of the circuit.

1.1.3 Rogowski coil

A special paragraph is dedicated to the Rogowski coil, because it is the instrumentation used to measure the current in the PFMA-3 and the electron beam current produced by PFMA-3 device.

Rogowski coils have been used for the detection and measurement of electric currents for decades. The theory of the Rogowski coil illustrates very well how a coil can be considered as an embodiment of Ampere's Law. A Rogowski coil works by sensing the magnetic field in the space around the conductor and Ampere's Law provides the relationship between the current flowing and the magnetic field around it.

If a line is drawn in a loop which totally encircles the current then, according to Ampere's Law, the line integral of the magnetic field around the loop is equal to the net current enclosed by it no matter what path the loop takes. If the loop encloses no net current the line integral is zero. Mathematically this is expressed as

$$\oint H \cos a \, dl = i \tag{1.5}$$

where "dl" is a small element of length along the loop, "H" is the magnetic field and a is the angle between the direction of the field and the direction of the element.

Figure 1.4 shows a long, thin helical coil, with "n" turns per meter and cross-sectional area "A" which encircles a conductor carrying a current "i". In a section of length "dl" the number of turns is "ndl" and the magnetic flux linking the section is

$$d\Phi = \mu_0 H A n \, dl \cos a \tag{1.6}$$

where "H" is the magnetic field and "a" is the angle between the direction of "H" and the axis of the coil section. The flux linking the entire coil is given by integrating along the coil:

$$\Phi = \int d\Phi = \mu_0 n A \int H \cos a \, dl = \mu_0 n A i \tag{1.7}$$

Ampere's Law has been used to evaluate the integral. For an alternating current the voltage output from the coil is given by the rate of change of flux:

$$v_{coil} = -\frac{d\Phi}{dt} = -\mu_0 n A \frac{di}{dt} \tag{1.8}$$

The Rogowski coil is a solenoidal conductive wire loop (coil) whose ends are brought around together to form a torus so that it can completely surround an element in which an electrical current (variable time) flows, [6]. The addition of an integrator to the coil completes the transducer to provide a voltage which reproduces the current waveform.
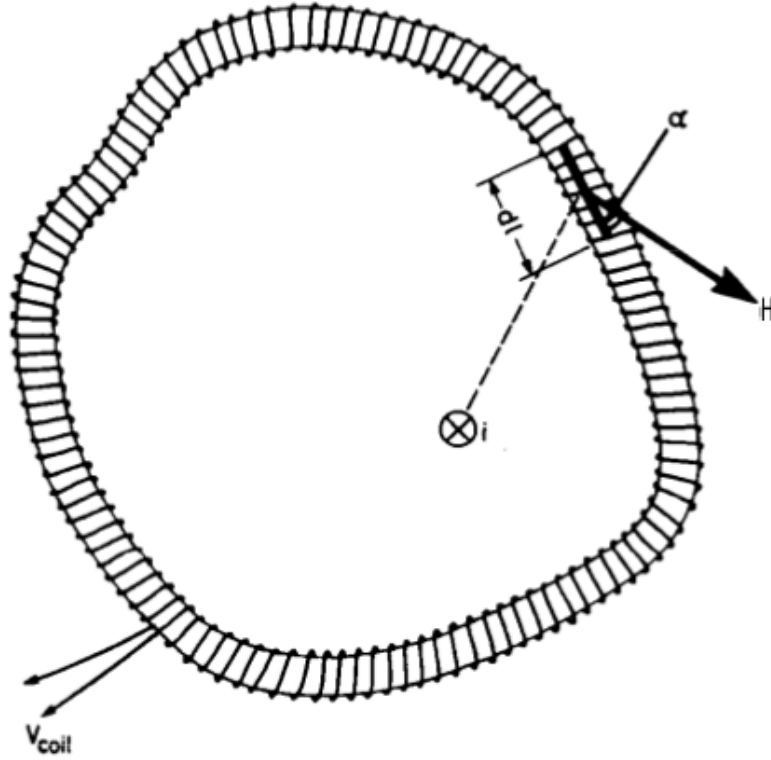
Figure 1.4   Equivalent electrical circuit of Rogowski coil

Figure 1.5 shows a typical active system using an inverting integrator. Other integrator designs, including passive integrators, can be used depending on the circumstances. Appropriate calibration is needed to evaluate the current.

The time variation of the current induces a voltage at the ends of the coil which is proportional to the time derivative of the current. If "M" is the mutual inductance between the Rogowski coil and the conductor, the output is given by

$$v_{coil} = -M\frac{di}{dt} \tag{1.9}$$

(see equation 1.8).

Rogowski coils are to date the sole device that can measure currents up to several thousands of kA which vary extremely rapidly with time.

The Rogowski coil for the PFMA-3 device is used to measure the signal from the derivative of the current (Idot coil). It is connected through a RG-058U cable with $50\,\Omega$ impedance and BNC connector with $50\,\Omega$ impedance to a Tektronix DPO 4032 oscilloscope with an attenuator of $20\,\text{dB}$; the calibration factor of the Idot coil is $46.8 \cdot 10^5$ $[\text{kA}\,\text{s}^{-1}\,\text{V}^{-1}]$.

An example of the current derivative signal, measured with the Idot coil for the PFMA-3, and its integral are shown in Fig. 1.6. The *pinch phase* corresponds to the large disturbance shown in the current derivative and the step in the graph of the current, occurring at the same time.
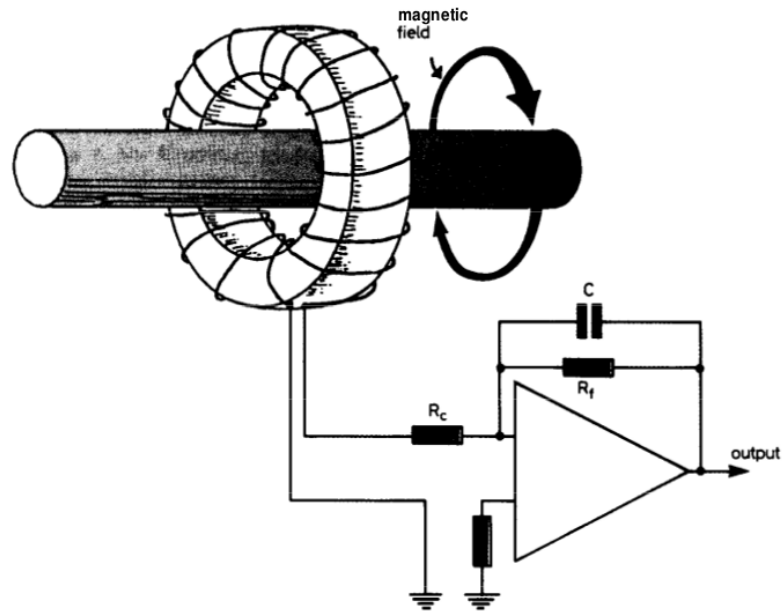
Figure 1.5   Arrangement of coil and integrator

To measure the electron beam exiting the drift tube of the PFMA-3 a Rogowski coil is also used. It is attached with a special shielded Huber-Suhner (SUCOFLEX 100 104/EM) cable to a Tektronix DPO 4032 oscilloscope without an attenuator, only with a BNC connector with $50\,\Omega$ impedance. The calibration factor for this Rogowski coil is 16.5 [kA V^{-1}]. Figure 1.7 represents the current of the electron beam, measured with the Rogowski coil, the measuring signal is seen to come in correspondence of the *pinch* phase.
The settings of the Rogowski coil for the electron beam measurements are described at the end of chapter 2.

1.1.4   Fields of Application of Plasma Focus devices

PF devices are widely used and studied as multiple radiation sources, they have the great advantage of being a controllable pulsed source of radiations [2].
Depending on the filling gas mixture, intense bursts of neutrons and charged particles beams (relativistic electron beams and ion beams), as well as hard and soft x-rays can be obtained.
Moreover, the ongoing research aims at demonstrating their potential application as x-ray sources for next generation micro-electronics lithography and surface micro-machining; their properties as pulsed x-ray and neutron source are under investigation for medical applications and security inspection analysis, while intense ion beams are of interest for materials implantation.
Other applications include nuclear explosion simulations (i.e. for testing of the electronic equipment) and non-contact discovery and/or inspection of nuclear materials by neutron activation analysis (NAA). In recent years, they have been also studied as possible com-
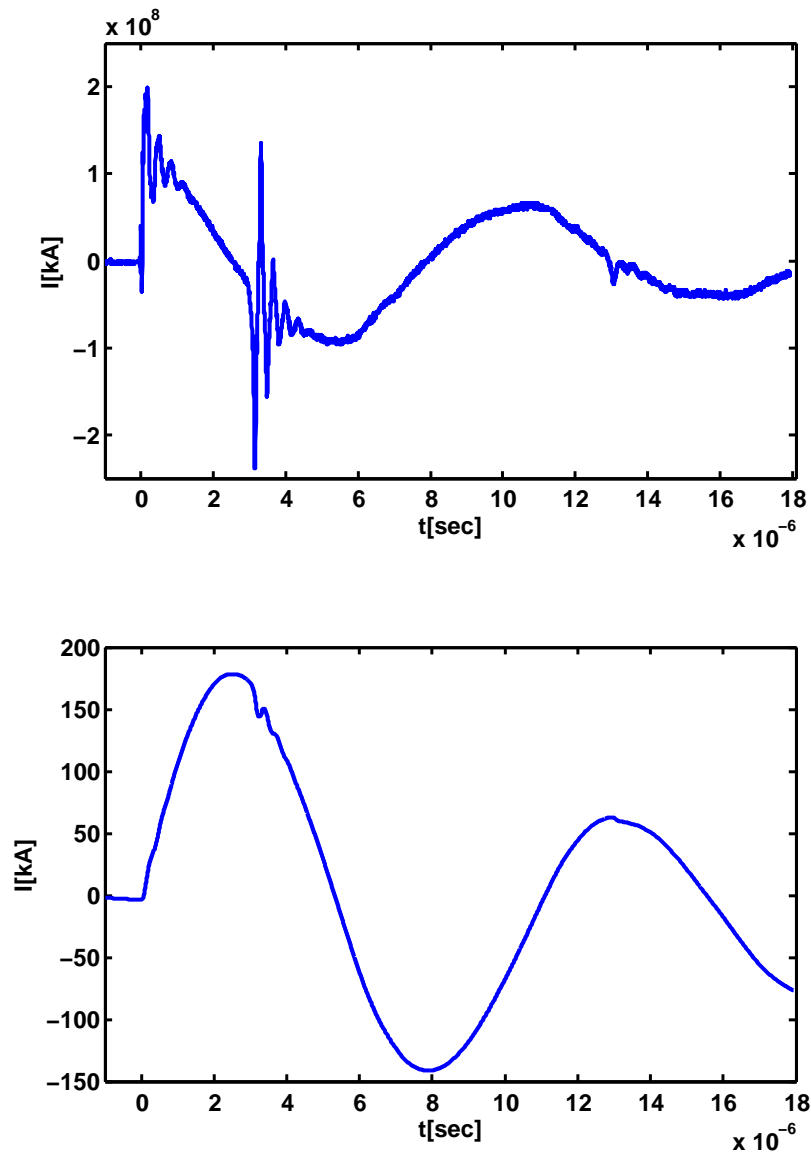
Figure 1.6   I-dot signal and current signal of PFMA-3

petitive breeder of short-lived radioisotopes (SLR).

The advantages of Plasma Focus devices as radiation sources are evident. Their main drawback is related to the repetition frequency, which usually make them less competitive than other devices. Indeed, in order to move their technology from the applied research environment to possible industrial application, Plasma Focus devices need to be operated at high pulse repetition rate. However at each discharge part of the device input energy is converted into thermal loads on the structural components of the machine itself, and this could be a major cause for mechanical failure. Apt cooling systems are therefore to be provided and installed on the devices to get them to operate repetitively. Thermal loads are not only critical from a macroscopic point of view due to the induced thermal strain and stress, but also from the microscopic point of view of plasma purity: metal particles
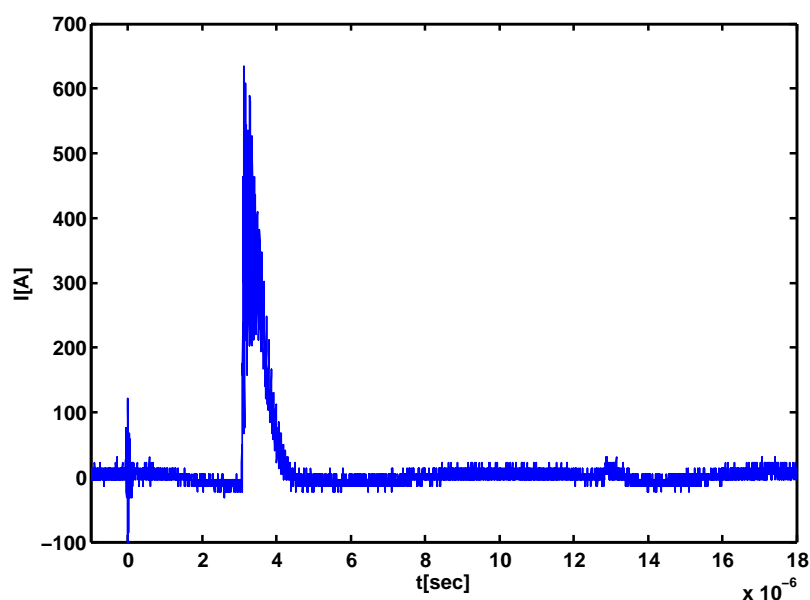
Figure 1.7 Electron current signal of PFMA-3

are ablated by the high temperature plasma from the electrodes and carried by the sheath into the pinch region where nuclear reactions occur. Many scientific and technological issues must be addressed for a high-energy Plasma Focus device to operate at high pulse repetition rates.

1.2   Development of the PFMA-3 device

Plasma Focus devices are well known, as described in the above paragraph, to emit during their pinch phase a collimated beam of electrons in the backward direction, i.e., the direction opposite to that of macroscopic motion of the plasma sheet between the electrodes.
It has been suggested that the beam be utilized as a source in radiation therapy, particularly in IORT (IntraOperative Radiation Therapy) applications [7, 8]; due to the short delivery time and to the possibility of a high repetition rate, large doses can be delivered in a very limited time, producing a very high dose rate. The very high dose rate can change the RBE (the relative biological effectiveness).
The beam is very intense (1.25×10^{25} particles per discharge for PFMA-3, as measured with the the Rogowski coil, see end part of chapter 2), and lasts the time of the pinch, typically a few tenths of nanoseconds.
Within the framework of a research project of the Alma Mater Foundation of the University of Bologna the prototype Plasma Focus, PFMA-3 (for: Plasma Focus for Medical Applications number 3), has been designed, built and put into operation, to investigate the possible application to IORT.

1.2.1 IntraOperative Radiation Therapy

IntraOperative Radiation Therapy (IORT) is an intensive radiation treatment that delivers a concentrated beam of radiation to tumors as they are exposed during surgery. IORT allows direct radiation to the tumor while sparing normal surrounding tissue. IORT is used for cancer that cannot be cured with surgery alone and for tumors that are either attached or close to vital tissues. It can be delivered by electron beams produced by linear accelerators (also called IOERT), or high-dose rate brachytherapy (HDR- IORT). Most clinical experience involves IOERT.

IORT is performed with applicators and cones that attach to the treatment head of high-energy medical linear accelerators that are designed to direct radiation to defined surface structures. Most patients are subsequently treated with external beam photon irradiation (EBRT).

The INTRABEAM® system was first approved for use by the U.S. Food and Drug Administration (FDA) for intracranial tumors in 1999 and was subsequently approved for whole body use in 2005. The INTRABEAM® spherical applicators are indicated for use with the INTRABEAM® system to deliver a prescribed dose of radiation to the treatment margin or tumor bed during intracavity or intraoperative radiotherapy treatments.

The treatment that it is possible to conduct with the Plasma Focus device may be compared with the TARGIT treatment (an example of IORT) [9]. The early breast cancer (that may not require radiotherapy) can be treated with a conservative treatment that encompasses the whole breast in all patients, this novel therapeutic approach is Targit, that allows to the treatments to be safely and accurately delivered in a standard operating room.

It employs a miniature electron-beam-driven x-ray source called INTRABEAMTM(PeC) that emits soft x-rays ($50\,$kV) within the breast. The x-rays are emitted from the tip of a $10\,$cm and $63.2\,$mm diameter probe, that is enclosed in a spherical applicator (available in $2.5 \pm 5\,$cm diameter sizes), which in turn is inserted in the tumor bed and intraoperative radiotherapy is delivered in about 25 min. The prescribed dose is 5 and 20 Gy at $1\,$cm and $0.2\,$cm respectively, from the tumor bed.

1.2.2 First configuration of the PFMA-3 device

The first configuration of the device has a different geometrical configuration with respect to the present one, figure 1.8.

It will be dedicated a short description to it, a more detailed description will be dedicated to the one that is in operation.

The configuration is asymmetric, with no possibility of a symmetrical configuration, instead in the new configuration this is possible, figure 1.14.

The material of the superior and inferior plates is copper. Discharge current flows in focus tube electrodes through these two plates. The PFMA-3 capacitor bank is made of two capacitors connected in parallel to give a total capacitance of about $22\,$µF. The fast switch is

Figure 1.8 Old geometrical configuration of the PFMA-3
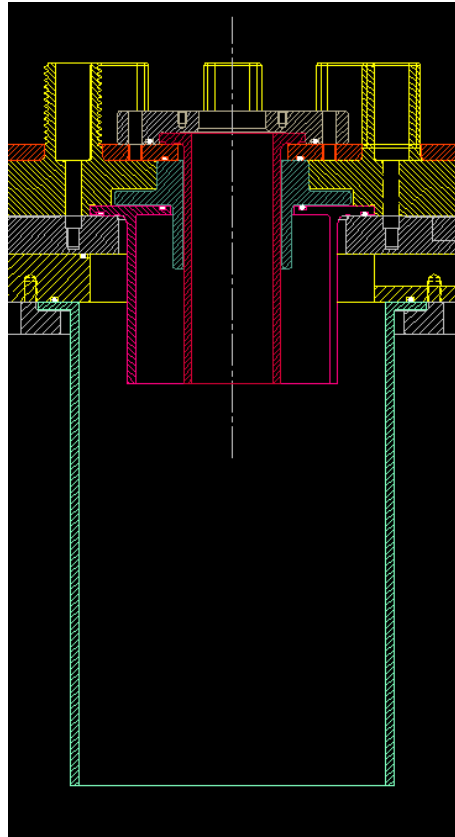
Figure 1.9   AutoCad representation of the electrodes and insulator of the Plasma Focus device

a spark-gap, that works with nitrogen at controlled pressure. The electrodes are in copper and they are 15.5 cm long, the internal electrode has a diameter of 6 5cm, the external one of 13cm; the insulator between the two coaxial electrodes was made of ceramics. Figure 1.9 shows the CAD drawing (the internal electrode is in red, the external one in purple and the insulator in blue).

To study the device a simulation with Comsol Multiphysics of the inductance was performed. The inductance is an important parameter to control the *pinch time* and the efficiency of the Plasma Focus device, so the electron beam produced.
The other two important parameters to control the efficiency of the electron beam produced are the voltage, especially because it is possible to increase the energy, so the strength to compress the plasma, and the pressure. Decreasing the pressure is more easy for the device to compress the plasma, but if it has decreased too much, it is possible not to have the compression phase. The important thing is to find a good trade-off between all the parameters.

1.2.3   Comsol Multiphysics simulations

Simulating the inductance of the PFMA-3 with Comsol-Multiphysics [10], it was possible to compare the measured results with the simulation and understand the good development

of the geometrical configuration of the device.

It was chosen the AC/DC module for this simulations, the problem is a 3D problem.

The AC/DC Module Model Library consists of a set of models from various areas of low-frequency electromagnetic field simulations.

The phenomena are very fast so it was chosen a magneto-static problem. This application mode handles problems for magnetic fields with currents sources.

First it was modeled the geometry simplifying the particulars, then the boundary conditions have to be set and the materials and the equation parameters have to be selected. The geometry has to be meshed and the solution have to be computed, so the solver parameters have to be chosen and finally the problem has to be post-processed to visualize the solution.

To model the inductance the lumped parameters are used. Lumped parameters are matrices describing electromagnetic properties such as resistance, capacitance, and inductance. In the time-harmonic case the lumped parameter matrix is either an impedance matrix or an admittance matrix. In a static calculation it possible to get the resistive, capacitive, or inductive part of the lumped parameter matrix.

To calculate the lumped parameters, there must be at least two electrodes in the system, one of which must be grounded. It is possible to force either a voltage or a current on the electrodes. After the simulation, it is possible to extract the other property or the energy and use it when calculating the lumped parameters. There are several available techniques to extract the lumped parameters. Which one to use depends on the application mode that it was used, what parameters are important, and how it is chosen to solve the model. If a system is specified where all terminals are ports, redundant matrix elements are obtained. This is better understood if it is possible to view a two-terminal system. If both terminals are declared as ports, 2-by-2 matrix is obtained for the system. This is clearly too many elements, because only one unique lumped parameter is allowed between the terminals. As soon as the other ground terminals are declared somewhere in the system, 3-terminal system is obtained and the lumped parameter matrix becomes a 2-by-2 matrix. There are the two point where the voltage is applied, where it is connected the capacitor bank near the spark-gap.

If voltages are applied to the ports, the extracted currents represent elements in the admittance matrix, Y. This matrix 1.10 determines the relation between the applied voltages and the corresponding currents with the formula:

$$\begin{bmatrix} I_1 \\ I_2 \end{bmatrix} = \begin{bmatrix} Y_{11} & Y_{12} \\ Y_{21} & Y_{22} \end{bmatrix} \begin{bmatrix} V_1 \\ V_2 \end{bmatrix} \tag{1.10}$$

so when V_1 is nonzero and all other voltages are zero, the vector I is proportional to the first column of Y.

In Electrostatics the current is replaced with charge and the admittance matrix is replaced with the capacitance matrix, see matrix 1.11. This is the calculation used to calculate the capacitance of the problem.
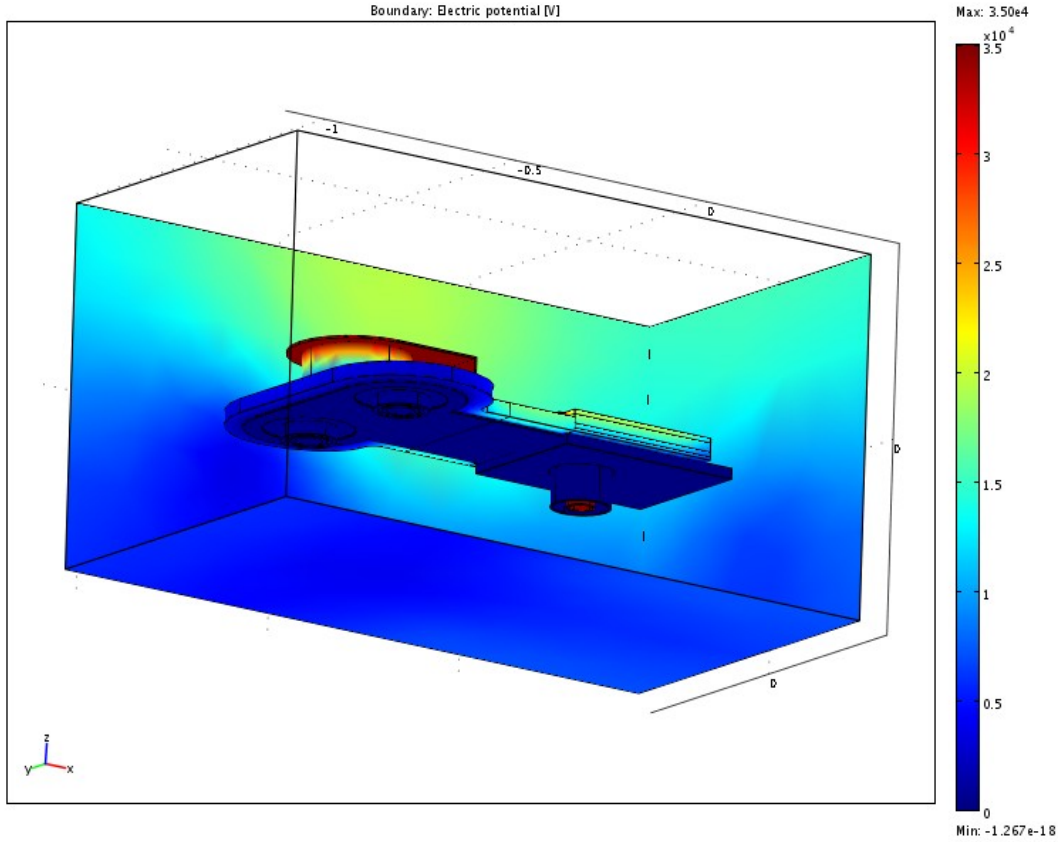
Figure 1.10   Electric potential of the Plasma Focus device

$$\begin{bmatrix} Q_1 \\ Q_2 \end{bmatrix} = \begin{bmatrix} C_{11} & C_{12} \\ C_{21} & C_{22} \end{bmatrix} \begin{bmatrix} V_1 \\ V_2 \end{bmatrix} \tag{1.11}$$

In fact the model of the problem is calculated in two part to obtained the inductance. First the electrostatic part so the electric potential, forcing the voltage from the capacitor bank, see results in figure.

It is possible to see that the inferior plate is at ground as it has to be, like the external electrode, instead the internal electrode, as the superior plate, at maximum electric potential. It might be necessary to calculate the Z-matrix in a more direct way. Similar to the Y calculation, the Z calculation can be done by forcing the current through one port at the time to a nonzero value while the others are set to zero. Then, the columns of the impedance matrix are proportional to the voltage values on all ports:

$$\begin{bmatrix} V_1 \\ V_2 \end{bmatrix} = \begin{bmatrix} Z_{11} & Z_{12} \\ Z_{21} & Z_{22} \end{bmatrix} \begin{bmatrix} I_1 \\ I_2 \end{bmatrix} \tag{1.12}$$

In magneto-static this option means that the "energy method" is used. When using this method the potential or the current is nonzero on one or two ports at a time and the energy density is extracted and integrated over the whole geometry. The following formulas show

how to calculate the capacitance matrix from the integral of the electric energy density.

$$C_{ii} = \frac{2}{V_i^2} \int_\Omega W_e d\Omega \qquad V_j = \begin{cases} 0 & j \neq i \\ V_i & j = i \end{cases} \qquad (1.13)$$

$$C_{ij} = \frac{1}{V_i V_j} \int_\Omega W_e d\Omega - \frac{1}{2}\left(\frac{V_i}{V_j}C_{ii} + \frac{V_j}{V_i}C_{jj}\right) \qquad V_k = \begin{cases} 0 & j \neq i, j \\ V_i & k = i \\ V_j & k = j \end{cases} \qquad (1.14)$$

It is possible to calculate the inductance matrix in the same way from the magnetic energy density:

$$L_{ii} = \frac{2}{I_i^2} \int_\Omega W_m d\Omega \qquad I_j = \begin{cases} 0 & j \neq i \\ I_i & j = i \end{cases} \qquad (1.15)$$

$$L_{ij} = \frac{1}{I_i I_j} \int_\Omega W_m d\Omega - \frac{1}{2}\left(\frac{I_i}{I_j}L_{ii} + \frac{I_j}{I_i}L_{jj}\right) \qquad I_k = \begin{cases} 0 & j \neq i, j \\ I_i & k = i \\ I_j & k = j \end{cases} \qquad (1.16)$$

This is the technique used when Fixed current or Fixed current density are selected in the Magneto-statics application mode. In fact to calculate the inductance it is applied a fix current on the two points attached at the capacitor bank, where the current begins to flow, and after the spark gap, in the bottom part of the superior plate.

What it is making the connection in the reality between the two electrodes is the the plasma, here it is simulated with a thin plate of the same material of the electrodes, that connects both.

The magnetic flux density is shown in the figure 1.11, the magnetic flux density from the point of view of the electrodes is shown in figure 1.12

Figure 1.13 is a representation of the current flow, as it should be, from the superior plate, inside the internal electrode, to the external one and finally to the inferior plate that is connected to the ground.

The total calculated inductance was 150nH.

To compare this result with the real measurements, this calculation has to be made. The oscillation of the RLC circuit of the Plasma Focus device, neglecting the resistance, in short-circuit configuration, is:

$$\omega = \frac{1}{\sqrt{LC}} \qquad (1.17)$$

where L is the inductance and the C capacitance, the oscillation ω is also:

$$\omega = \frac{2\pi}{T} \qquad (1.18)$$

measuring with the oscilloscope the period "T", 11.6 μs, the oscillation becomes 5.4×10^5 Hz. So it is possible to calculate the inductance, knowing that the capacitance of the Plasma
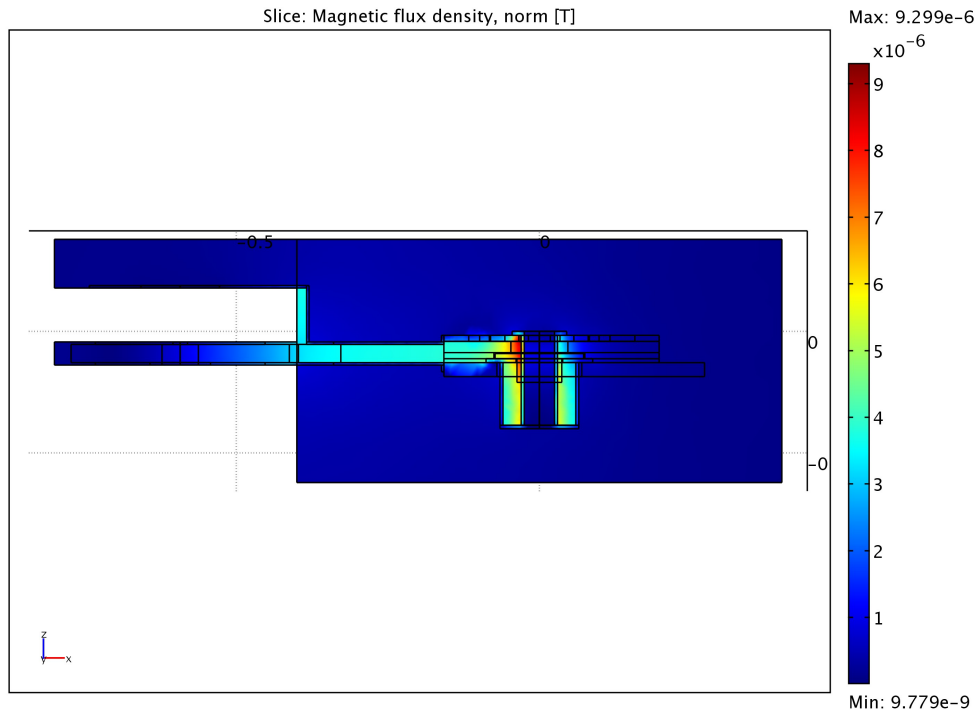
Figure 1.11   Magnetic flux density: global point of view
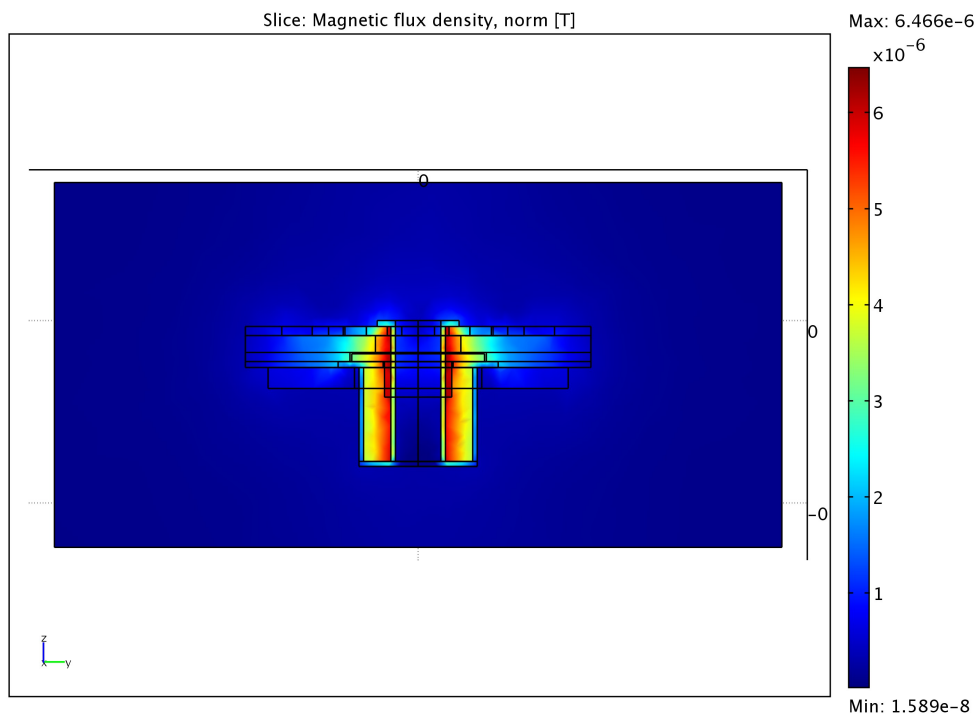
Figure 1.12   Magnetic flux density: electrodes point of view

Arrow: Total current density
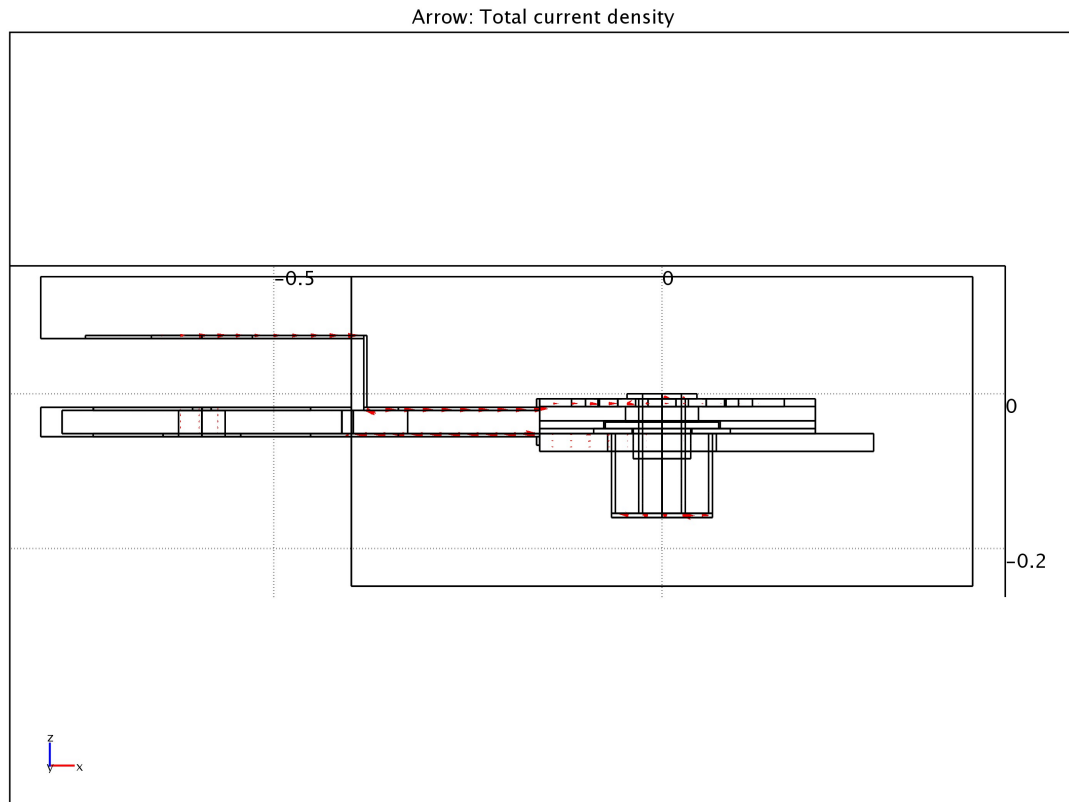
Figure 1.13   Current flow density in the Plasma Focus device

Focus device PFMA-3 is 22 μF. From the equation 1.19, that is an elaboration of equation 1.17:

$$L = \frac{1}{\omega^2 C} \tag{1.19}$$

the results of the inductance is 155.1 nH, comparable with the results obtained from the simulation with Comsol Multiphysics.

1.3   PFMA-3: Plasma focus For Medical Application number 3

The device like in figure 1.8 is not in the optimal geometrical configuration, because the *pinch time* comes not during the maximum of the current flowing in the device; it is necessary to improve the efficiency of the "pinch" changing the geometry of PFMA-3.
Figure (Fig. 1.14) shows the new configuration. This new configuration works in asymmetric way, but it is possible to work also in symmetric configuration.

Figure 1.14   PFMA-3: new geometrical configuration

1.3.1   Plasma Focus room and control room

The room where the Plasma Focus is positioned is visible in figure 1.15. The area has the dimensions of 5×10 m and is delimited by a gate. The control room, figure 1.16, is behind the glass window shown in figure 1.15.

In the control room the triggering unit is positioned, with a rapid safety dump to ground the capacitor bank if some residual voltage remains. The remote trigger unit, product of the R.E. Beverly III and Associates Pulsed Power Products Division, is used to initiate the discharge in the rail gap, which in turn acts as a switch to transfer energy from the capacitor to the plasma focus electrodes. The rapid safety dump is product of SAE group (SAE Remote Trigger HCK 2500-35000).

In the control room, there is also the acquiring data unit: the Tektronix DPO4032 Digital Phosphor Oscilloscope for the current measurements, where the RG-058U coaxial cables are connected.

Figure 1.15   PFMA-3 working room

1.3.2   Electrodes and insulator

The geometry of the electrodes are modified, to change the inductance of the Plasma Focus device. The relation that calculates the inductance of the electrodes is the following:

$$L = \frac{\mu_0 \mu_r}{2\pi} l \ln\left(\frac{R_2}{R_1}\right) \tag{1.20}$$

where "l" is the length of the electrodes and "R_2" and "R_1" the radii of the electrodes. They are always 15 cm long and made of copper, the external one being a squirrel cage-type electrode. The diameters of both were decreased: the internal one became 3.8 cm and the external one 6.8 cm, in this way the inductance of the electrodes decreased of ∼5 nH.

Between the two electrodes there is the insulator, also its diameter was decreased as consequence, and the material changed in Pyrex, figure 1.17.

The insulator is made of two parts: the central one is a hollow cylinder made in Pyrex, in contact with the plasma sheet; the external one is made of Delrin. The external one is made, in turn, by two hollow cylinder that have the same internal diameter, but different external one. The internal diameter is the same of the central part 3.6 cm, the external one is for the smaller cylinder 9.4 cm and for the bigger one 14.5 cm.

The inferior and superior plates are made of stainless steel: the fast switch is connected to the internal electrode through the anode collector plate, earth electrode (the external one) also connects to cathode collector plate. Discharge current flows in focus tube electrodes
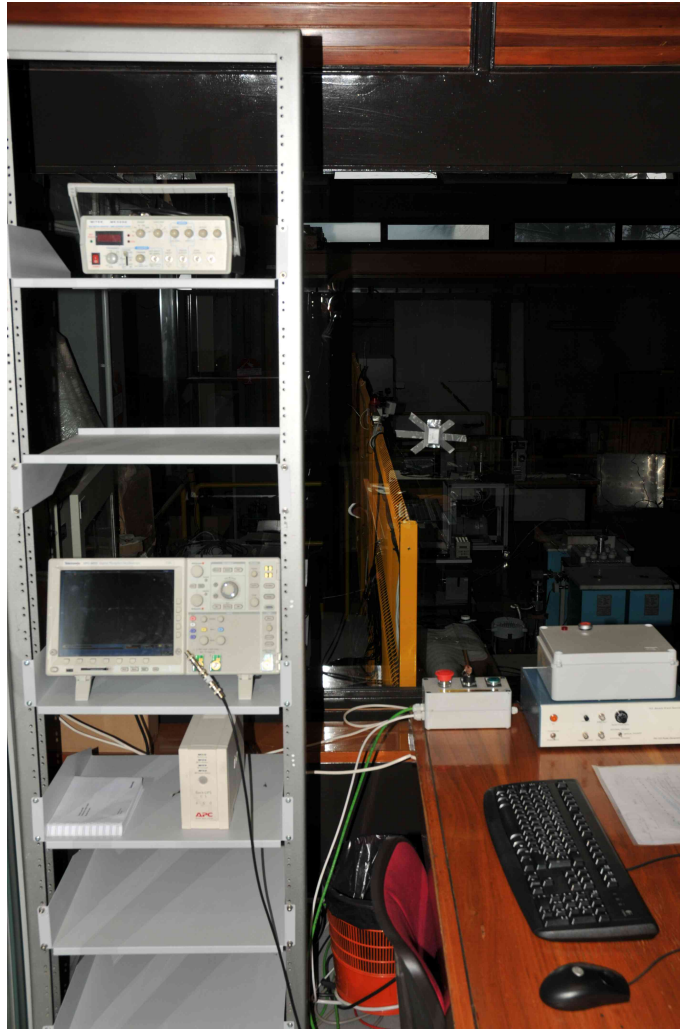
Figure 1.16   Control room

through these two plates. Besides, in common configurations for Mather type plasma focus devices, insulator spacers are needed between anode and cathode collector plates, in fact between the two plates there is 5 cm of Delrin.

1.3.3   Fast switch: Rail-gap

The fast switch able to discharge the bank capacitor is not any more a spark gap, but a rail-gap made by SAE GROUP (reproducing a Maxwell rail-gap switch [11]), figure 1.18. The method involves producing a glow discharge between the two copper electrodes (planar configuration), figure 1.19, the trigger discharge is arranged to extend to the full length of the rail electrode. The switch works with air at controlled pressure.

In the lower part of figure 1.18, it is possible to see the rail-gap opened and the two electrodes facing each other.

Figure 1.17   Insulator

1.3.4   Power Supply, Capacitor Bank and Gas Working Unit

The power supply shown in figure 1.20 is connected to the bank capacitor to charge it and to the trigger unit. The power supply is made by FUG Elektronik GmbH, type HCK 2500-35; the limits of output parameters are: $35\,kV$; $140\,mA$ and $2500\,J/\sec$.

The PFMA-3 capacitor bank is made of two capacitors connected in parallel to give a total capacitance of about $22\,\mu F$.

The capacitor bank comes from General Atomic (Energy Products), model GA32899; it is possible to charge them until $36\,kV$, each capacitor has a capacitance of $11.1\,\mu F \pm 10\%$, with a inductance of $0.03\,\mu H$.

The gas working system is visible in figure 1.21. The gas working system is used to fill the vacuum chamber with the inlet gas: nitrogen.

The nitrogen cylinders have these specific characteristic: $10\,m^3$ of compressed nitrogen at $200\,bar$ of charge. The impurities are: $H_2O < 3$ ppm, $O_2 < 2$ ppm and $C_nH_n < 0.5$ ppm. The vacuum chamber is in quartz, has the dimension of $30\,cm$ of height, $20\,cm$ of diameter and $5\,mm$ thickness and is electrically connected to laboratory ground.

1.3.5   Vacuum system

The vacuum system comprises a turbomolecular pump $(10^{-7}mbar)$ assisted by one scroll pump for the pre-vacuum $(10^{-3}mbar)$, the seals for the vacuum are copper gaskets and o-ring closed by clamps. The turbomolecular pump is a TURBO V-70 made by Varian; the scroll pump is a product of BOC EDWARDS, model XDS 10. Two pressure gauges, an active ion gauge (AIGX-S product of BOC EDWARDS) and a Barocel gauge (MKS baratron capacitance manometer) monitor the pressure in the chamber; while a flow-meter is connected to two electronic control valves to adjust the input of gases. Figure 1.22 shows the vacuum system of the PFMA-3 device.

1.3.6   Working parameters of the PFMA-3

The working voltage is $18\,kV$ and the working gas pressure is $45\,Pa$ of nitrogen; this means a bank energy of about $3.56\,kJ$.
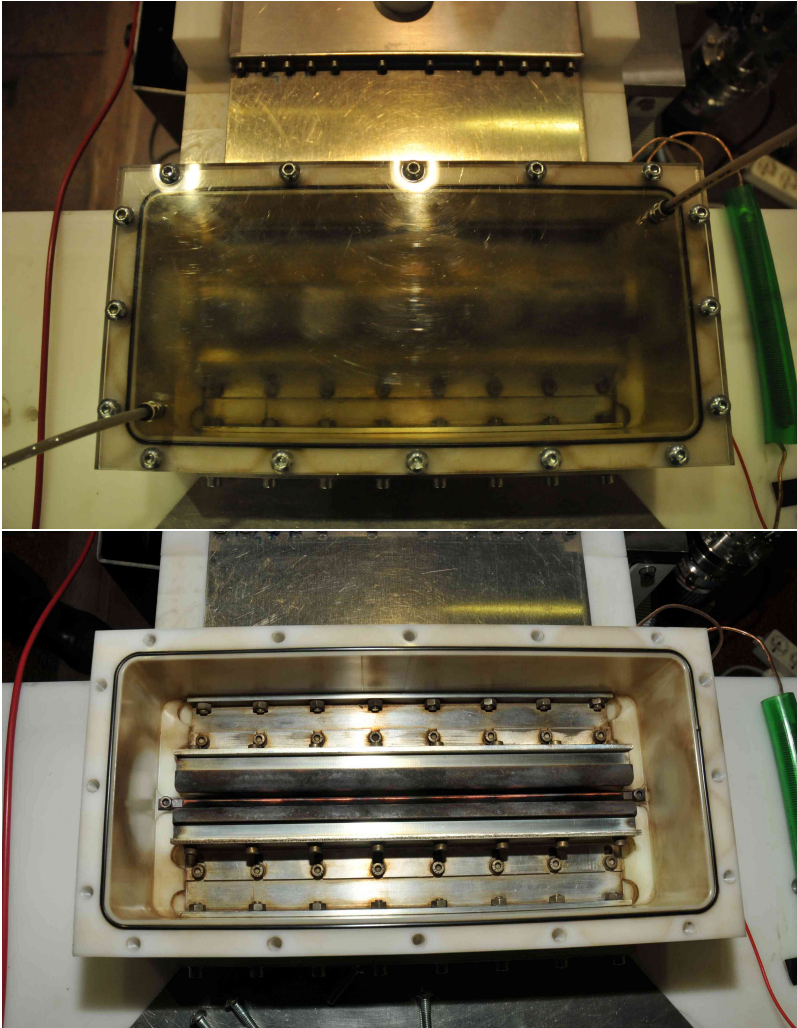
Figure 1.18   Rail-gap
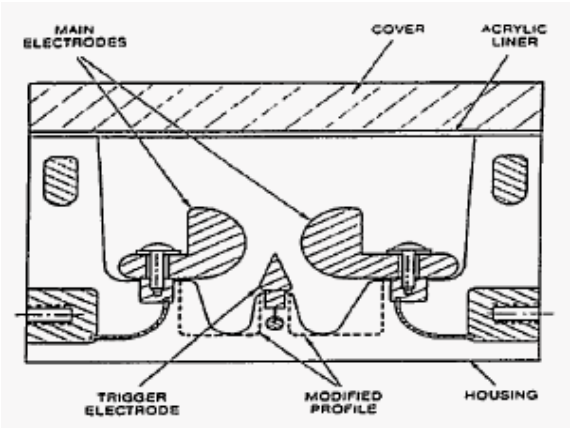
Figure 1.19   Schematic representation of the Rail-gap

Figure 1.20   Power Supply

The table 1.1 summarize all the principal parameters of PFMA-3.

From table 1.1 is possible to estimate, for example, the maximum total current for the Plasma Focus device; in the short circuit equations for the RLC equivalent circuit the resistance can be neglected and the inductance is constant and equal to the total inductance of the device, as it was said before; the total current can be estimate as:

$$I_{max} = \frac{V}{\sqrt{\frac{L}{C}}} \tag{1.21}$$

where V is the capacitor bank charging voltage. The total current results: $240\,\text{kA}$. A gross estimate of the plasma sheath macroscopic axial speed can be obtained experimentally with the simple $\tilde{u} \simeq \frac{4L}{\tau}$ where L is the electrode active length and τ is the pseudo-period.

Table 1.1   Characteristic of PFMA-3

	Value
Total Capacitance µF	22
Operating Voltage kV	18
Bank Energy kJ	3.6
Total Inductance nH	150
Pseudoperiod µs	10.3

Figure 1.21   Nitrogen cylinders

It is obtained $\tilde{u} \simeq 6.02 \frac{cm}{\mu s}$.

Figure 1.22   Vacuum system

Chapter 2

Electron beam produced by PFMA-3

The plasma focus device is being developed as a radiation source for intraoperative radiation therapy applications and there is a need for characterizing its electron beam, particularly, insofar as the energy spectrum is concerned. The instrument used is a magnetic spectrometer (Fig. 2.1) positioned at the end of the drift tube for the electrons produced by the PFMA-3.
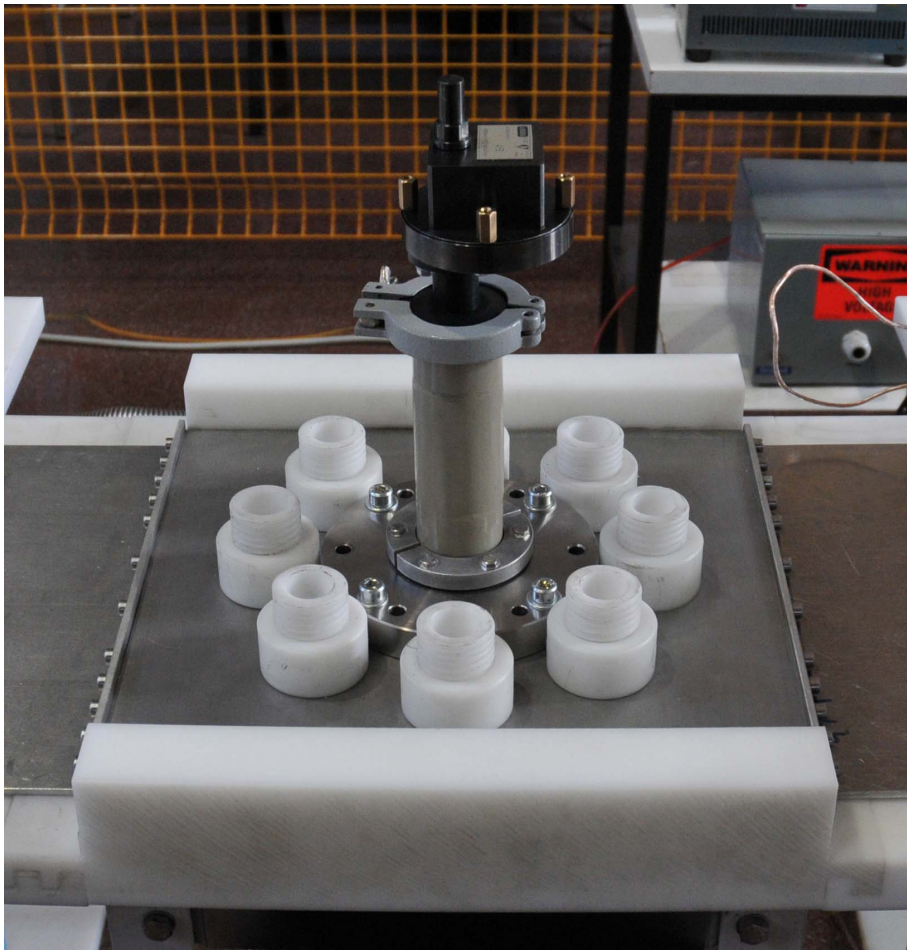
Figure 2.1   Magnetic spectrometer

2.1   Detector: Gafchromic film

The sensitive material used for the magnetic spectrometer to characterize the Plasma Focus device are the Gafchromic film: in particular the GAFCHROMIC® HD-810 film [12] and the GAFCHROMIC® EBT2 film [13]. The GAFCHROMIC® film are used because they have the important property of increasing its optical thickness proportionally to the adsorbed dose. To measure the electrons, in particular, the HD-810 film are used, for photons the EBT2 ones (characteristics of these film sheets will be discussed in chapter 3).
These two kinds of film are chosen because of the dose range, the sensible energy range and electron sensibility for the HD-810 GAFCHROMIC® film.
The procedure used throughout this campaign to read the films was as follows: samples were scanned on an HP Laser-Jet M1522 nf, at 300 dpi resolution, and the image converted to an 8-bit grey scale (256 shades of grey).
Every sample was first scanned before exposure to determine background optical density: the grey reading was averaged throughout the sample surface (i.e., over all the pixels) and a background value Z_b obtained. The sample was measured after exposure, the read-

ing averaged over the exposed surface and then the average background subtracted, thus generating the net reading Z_n.

2.2 Magnetic spectrometer

The spectrometer has a calibration, extending from 5 to 120 keV, evaluated on five energy values (5, 25, 70, 99 and 117 keV) interpolated with a 2nd order and with a 4nd order polynomial. The calibration points were obtained from an experimental campaign conducted in a foreign plasma focus laboratory. The two calibration curves are shown in Figure 2.2.

It should be observed that the two interpolating polynomials, once extrapolated to higher energies, differ significantly. For the purpose of the PFMA-3 IORT investigation, it was found necessary to extend the scale to higher energies and to obtain a finer resolution for a further validation.

Magnetic spectrometers are based on the gyration motion of charged particles in magnetic fields [14, 15]. The gyration radius increases monotonically with the kinetic energy of the particle, all other parameters (mass and charge of the particle and the strength of the B-field) being the same, with a univocal relationship between the two quantities. Therefore, after appropriate calibration, the energy of a particle can be inferred from its gyration radius, or more generally the deflection it undergoes in a known magnetic field. If collimated particles enter the magnetic field through an aperture and are then collected on a sensitive plate after a 180° turn, the elongation of the impact point from the aperture is, in turn, in univocal relation with the kinetic energy of the particle collected. When the magnetic field is not uniform, as is the case with all real spectrometers, the gyration radius for a particle of given mass and velocity changes from point to point, proportionally to the inverse of the modulus of the local magnetic induction; yet in a well designed spectrometer the elongation is still univocally tied to the energy: however, experimental calibration becomes necessary. This could conveniently be done with a tunable low energy electron gun; however, such an apparatus is not readily available in the majority of research laboratories, therefore, an alternative method has been devised, developed, and applied, as mentioned above, [16].

The spectrometer used in the present investigation is characterized by an average magnetic induction of 0.18 T. It is composed by two magnets facing each other. There are two kinds of magnetic spectrometer:

- single magnet facing a block of soft iron
- two magnets facing each other included in a casing of soft iron

The first configuration is the easier to produce, but is more inhomogeneous respect to the other. The role of the soft iron is to converge inside the strength lines of the B field, to make more homogeneous the B field. This effect is due the high magnetic permeability of the iron, even if the edge effects are still present.

With the second configuration the edge effects are minimized, but still present. These considerations can be more comprehensible analyzing the results of the two simulation with Comsol Multiphysics [10], figure 2.3.
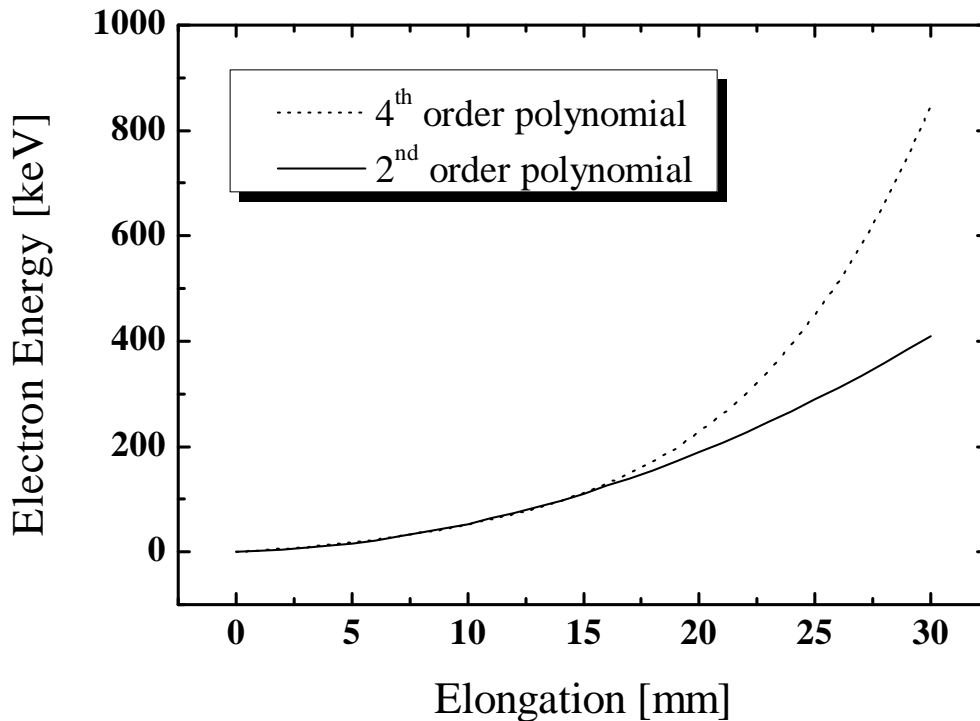
Figure 2.2   Calibration curve of the 2nd and 4nd order polynomial

The blue line represents the two magnets facing each other, second configuration; the red line is the case of one single magnet facing the block of soft iron, first configuration. The graph shows the trends in the middle of the transverse component of the magnetic field normalized to 1 between the two magnets, and between the magnet and the block of soft iron. The magnets and the soft iron block have a volume of $5 \times 5 \times 3$ *cm* and they are positioned at 2 cm of distance, around each configuration is positioned an envelope of a soft iron at 1 cm of distance from the magnet and from the soft iron block to reduce the B fields out the region of interest.

Figure 2.4 is the representation of the streamlines of the Magnetic flux density in the magnetic spectrometer with two magnets.

The experimental setup of the magnetic spectrometer is shown in Fig. 2.5.

The magnetic spectrometer is attached at the end of an extraction tube 15 cm long, made of iron, the seal is made with an o-ring and the clamp ensures the perfect electrical contact between the parts, as shown in figure 2.1. After the extraction tube the electrons emerge from a collimator, 3 cm long, with a 1 mm^2 aperture and enter the magnetic field, are deflected by a 180° angle and are finally collected on a sensitive material, described below, at a certain distance from the exit aperture of the collimator. The elongation from the collimator would be equal to twice the Larmor radius, if the magnetic induction were perfectly uniform. Still, the elongation depends univocally on the velocity (hence the kinetic energy) of the particles. Therefore, upon appropriate calibration, measurement of the elongation yields the energy of the particles collected at any particular distance.
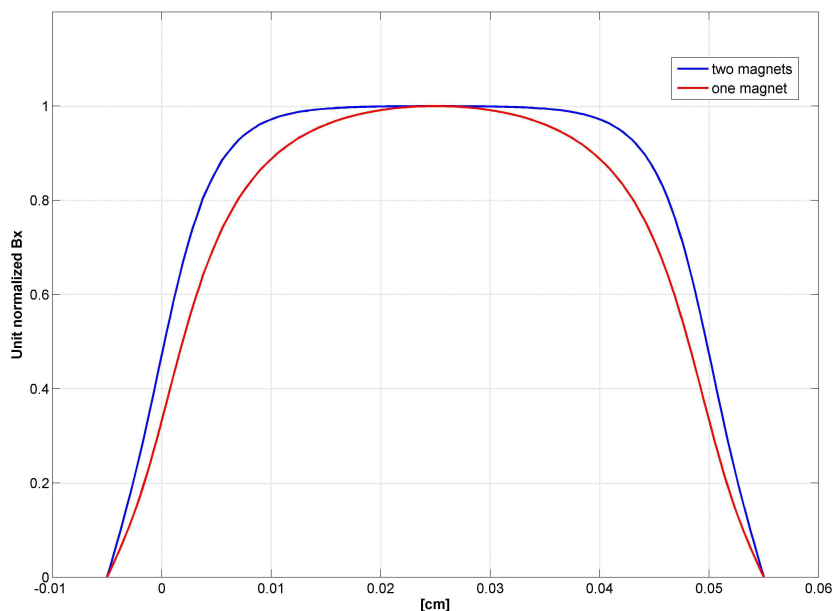
Figure 2.3 Difference in the B field between one and two magnets

It is to be stressed that the entire system is in the same atmosphere of nitrogen at 0.45 mbar mentioned in Chap. 1: therefore, collisions in flight by the electrons are negligible and like-wise the space charge effect. The net electron current delivered by PFMA-3 was measured to be about 0.4 kA (how the electron current is measured will be described later in this chapter), over an order of magnitude below the Alfvén-Lawson limit [17, 18]. However, e-beam currents of the order of 10 kA and more have been known to be produced in dense plasma focus devices: in those cases, the Alfvén-Lawson criterion may become an issue [1] and would needs accounting for. A real picture of the GAFCHROMIC® film setting is shown in figure 2.6.

Unlike its usual application, the film was used only to detect electrons, as no dose mea-surements were involved in the present investigation. This type of detector was used, rather than regular film, as it presents no need for the development with the related cumbersome and time consuming chemical procedure. The impinging electrons produce a blackening of the film, permitting to record the position of the impact point and hence its distance from the collimator.

2.2.1 Range calibration of the magnetic spectrometer

Electrically charged particles possess a range in matter, i.e., a mean distance that they can cross before coming to a stop: the range, for a given particle and material crossed, is a function solely of the particle energy. Conversely, knowing the range of a given particle in a given material yields the energy possessed by the particle (here reference is made to a
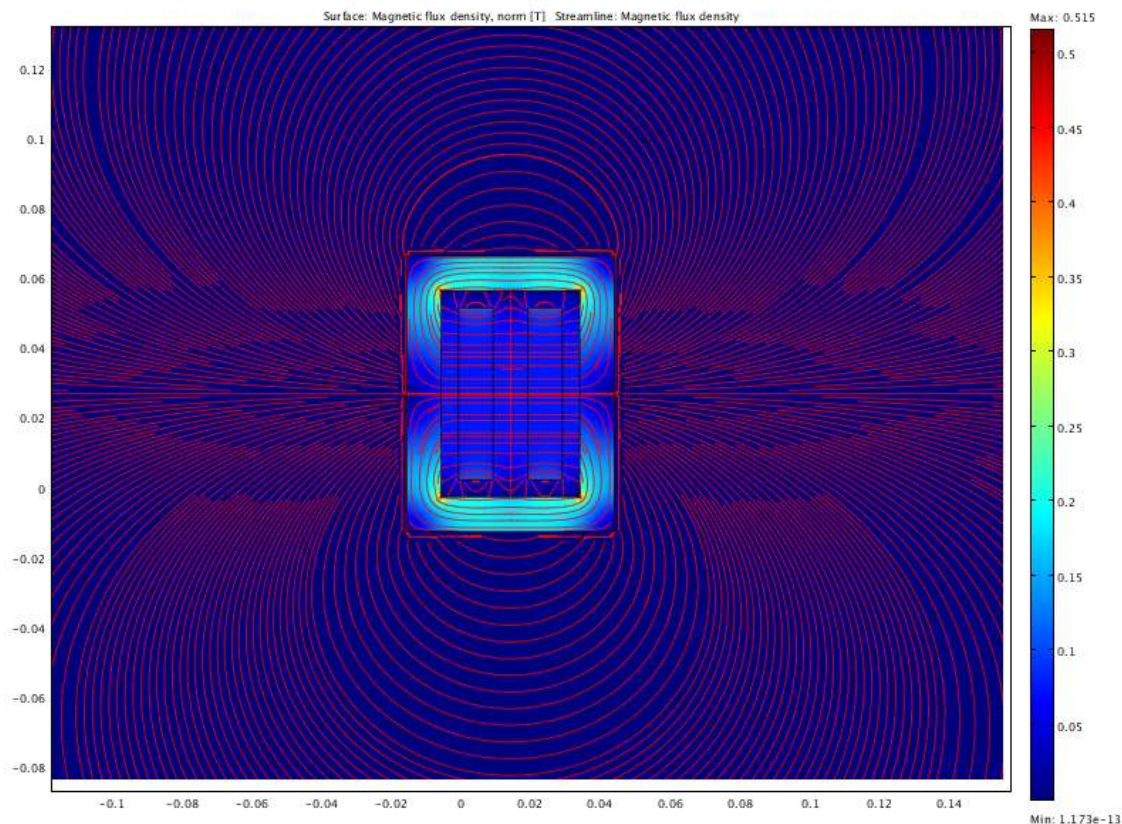
Figure 2.4   Strength lines of the B field inside the two magnets

representative particle: a statistical assembly is of course needed to assess the range).

Electron ranges in matter are tabulated for an array of energies and for many materials of interest [19]. This state of affairs can be exploited to determine the minimum energy that electrons must have possessed once it is known which thickness of the material they have been capable of crossing.

The sensitive material, the active layer of the GAFCHROMIC® film, described previously, has been covered with increasing thicknesses of the plastic material (including the own thickness of the insensitive coating of the film) to select higher and higher energies of the electrons and compare them with the distance from collimator detected. The assembly of the covering material and film was located at the end of the flight of the electrons in the spectrometer. The thicknesses crossed were connected to the minimum energy possessed by the electron through the NIST (National Institute of Standards and Technology) range-energy tables, interpolated with splines.

2.2.2   Range-energy determination

Two types of film were used: GAFCHROMIC® EBT2 film and HD-810.

The EBT2 film have the composition and the structure shown in figure 2.7. They are asymmetric on the two sides of the active layer. Details on the composing material
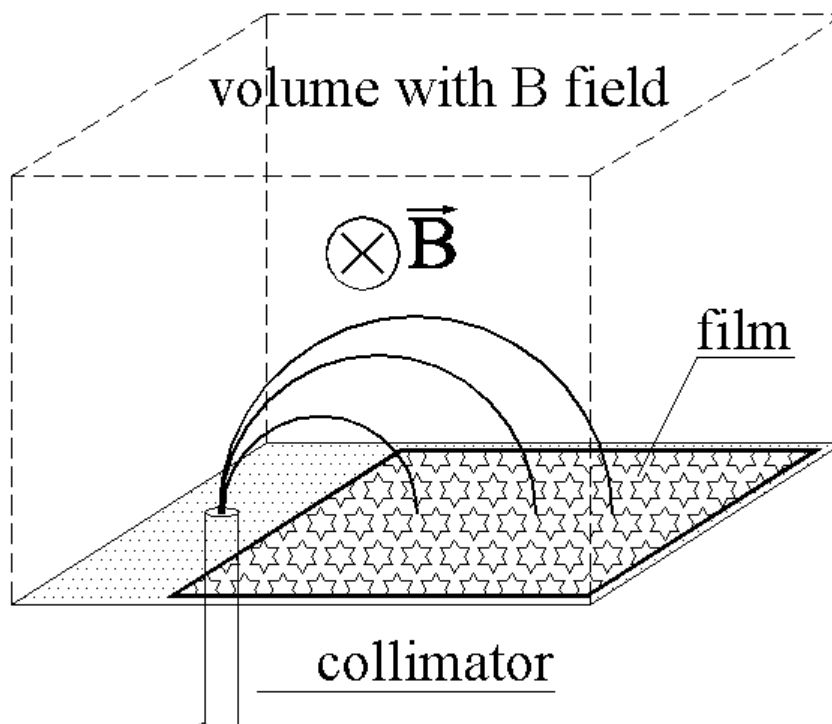
Figure 2.5 Experimental setup of the magnetic spectrometer

Table 2.1 Mass fraction composition of GAFCHROMIC®

	H	C	O	Li	Cl
Polyester	0.042	0.628	0.335		
Active layer	0.097	0.591	0.285	0.009	0.018
Adhesive Layer	0.094	0.651	0.255		
Surface Layer	0.058	0.310	0.250	0.063	0.320

for GAFCHROMIC® film are presented in table 2.1. The material that composed the GAFCHROMIC® EBT2 film are the same of the GAFCHROMIC® HD-810 film.

The compositions of the GAFCHROMIC® film described before are used to determine the contribution to the range. Polyester as a compound material is not present in the NIST tables, however, the composition of the polyester is essentially the same as that of Mylar®, and the density is very close ($1.35 \, \text{g/cm}^3$ for polyester to 1.39 for Mylar®). Details on the composing material for GAFCHROMIC® film are presented in Table 2.1.
Therefore, data for the latter, corrected for density, are used here in all calculations in place of those for polyester. For the adhesive layer, on the other hand, calculations have been performed introducing the actual composition in the procedure provided to this end in NIST tables.

As can be gathered from Figure 2.8, ranges in Mylar® and in the adhesive layer are
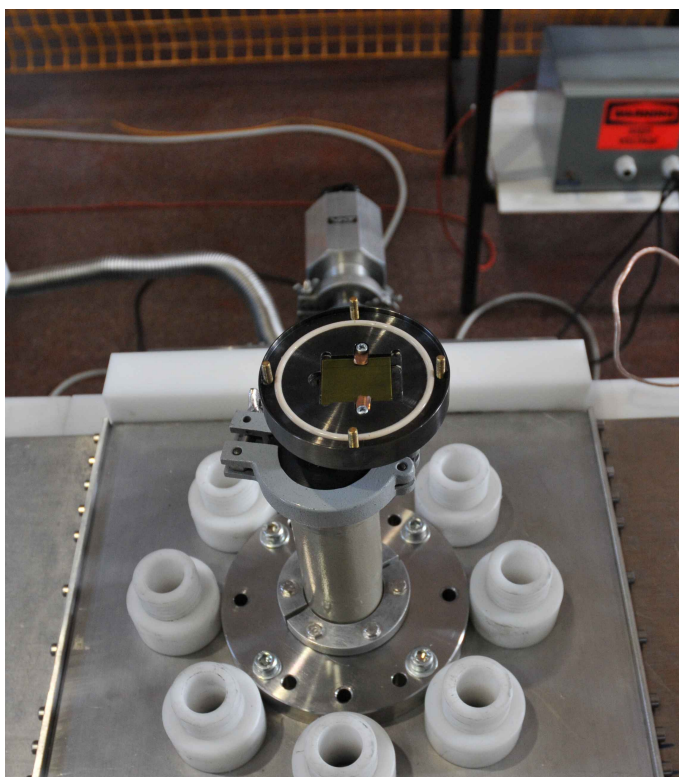
Figure 2.6   Gafchromic film position in the magnetic spectrometer

practically the same; therefore, films of either of the two types used will be treated, henceforth, as if comprised entirely of Mylar®.

GAFCHROMIC® film of both types present different thicknesses of the material on the two sides of the sensitive layer: this feature has been used, in conjunction with varying numbers of additional layers of $30\,\mu m$ thick Mylar® foil, to obtain the 13 different overall thicknesses used in the experiment as described in the following.

NIST range tables start at $10\,keV$: to obtain data for the lower energies it was necessary to resort to a different procedure. The values of NIST database are calculated and not the experimental.

Range for the electrons at low energies

The irradiation, consisting in 4 accumulated discharges, shown in figure 2.9 was performed on a GAFCHROMIC® HD-810 film and represents the electron spectrum produced by the PFMA-3 device.

In abscissa the values of the calibration curve in energy are reported as a function of distance. It is possible to notice a small unexposed area on the left side. This indicates that the electrons do not possess sufficient energy to pass through the substrate above the active layer of the GAFCHROMIC® HD-810 film.

The electrons have pass the surface layer of $0.75\,\mu m$ that it is possible to compare to
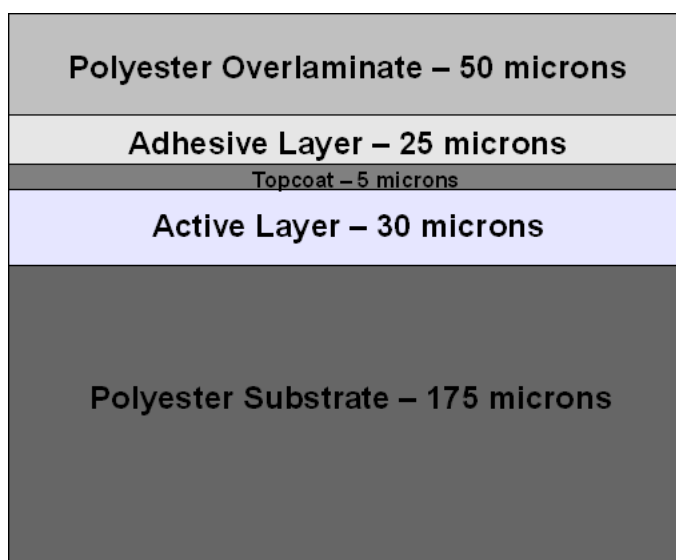
Figure 2.7   GAFCHROMIC® film: EBT2

Mylar® for the material composition. The energy of interest, as shown in the figure 2.9, is less than 10 keV, where the original calibration is used.

The following empirical formula for the range of electrons below 10 keV [20] is given in ref. [20]:

$$R = 0.0431 \cdot (E + 0.367)^{1.77} - 0.007 \tag{2.1}$$

where the energy E is expressed in keV and the Range R in µm. In figure 2.10 results from the above formula are shown in green, the data coming from the NIST database in blue.

As a first approximation, this formula can be accepted and it can be calculated that to cross 0.75 µm of Mylar®, 4.7 keV are necessary. As can be seen in figure 2.9 this result is consistent with the original calibration.

Articles were found in literature, reporting experimental measurements on the electron range at low energies.

Ref. [21] provides 13 experimental values from 1 keV to 10 keV for Mylar®. Ref. [22] reports an accurate experimental data for the stopping power in many plastic materials measured at 22 energy points. After spline interpolation the range was calculated from the following relation:

$$R = \int_{1eV}^{E_0} \frac{dE}{dx}^{-1} dE \tag{2.2}$$

where $\frac{dE}{dx}$ indicates the stopping power, R is the range and E_0 is the energy at which the range is to be assessed. Results for Mylar® are shown in Figure 2.11.

From the curve, in figure 2.11, it was calculated that at 0.75 µm correspond to 5.7 keV, this means that calibration at low energies is in good agreement with both: the original
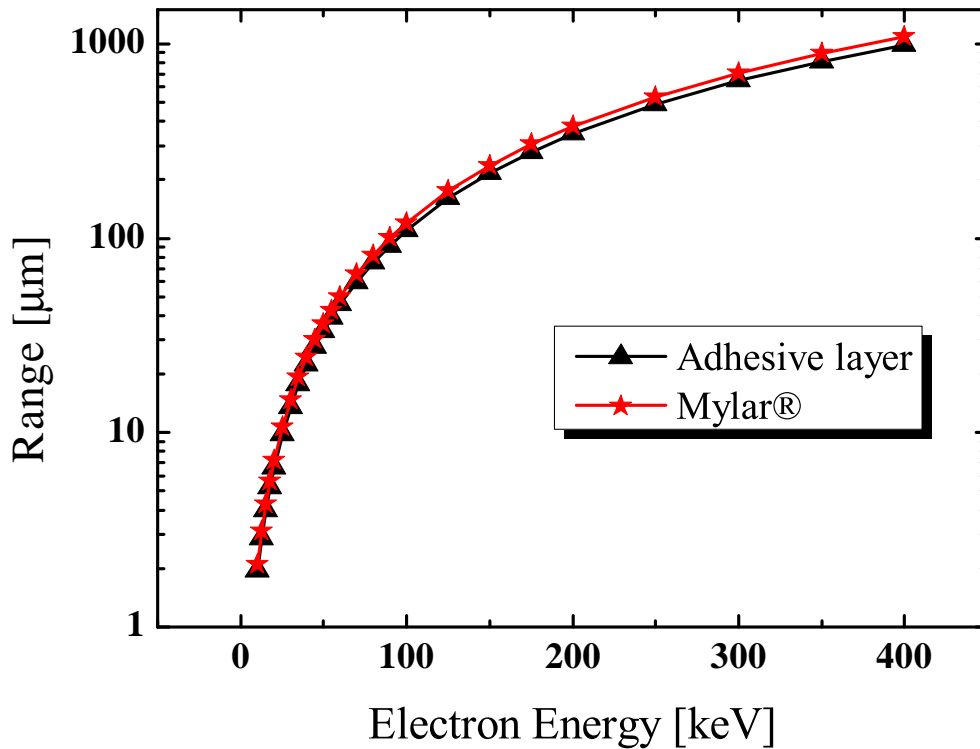
Figure 2.8   Comparison between the adhesive layer and Mylar®range

calibration and with the results of equation 2.1.

2.2.3   Experimental results and calibration curve

To investigate the energy response of the magnetic spectrometer, 13 different thicknesses of absorber were irradiated, as shown in Table 2.2.

The results obtained are shown in Fig. 2.12.

Both absorber thickness and offset from the collimator axis increase from left to right. Details of the experimental conditions and results are reported in table (2.3). The first number in column 1 refers to the total Mylar® thickness crossed by the electrons and is followed by the actual composition of the absorber pack, where (a) and (b) indicate which of the two sides of the film, falls the incoming beam: the one with the thinner or the other with the thicker coating, respectively. The second column presents the digitized image of the film after exposure; in the third column the optical density profile through the center of the image is presented. The following three columns report the experimental conditions: voltage, gas pressure, and number of discharges. The last column contains the elongation measured; the uncertainty of the measurement (1 s.d.) is ±0.5 mm.

The image on the film was scanned into an 8-bit gray scale. The resulting digital image was treated in MATLAB®: background (represented by the gray level of unexposed film) was subtracted and a profile through the center of the exposed area was extracted and
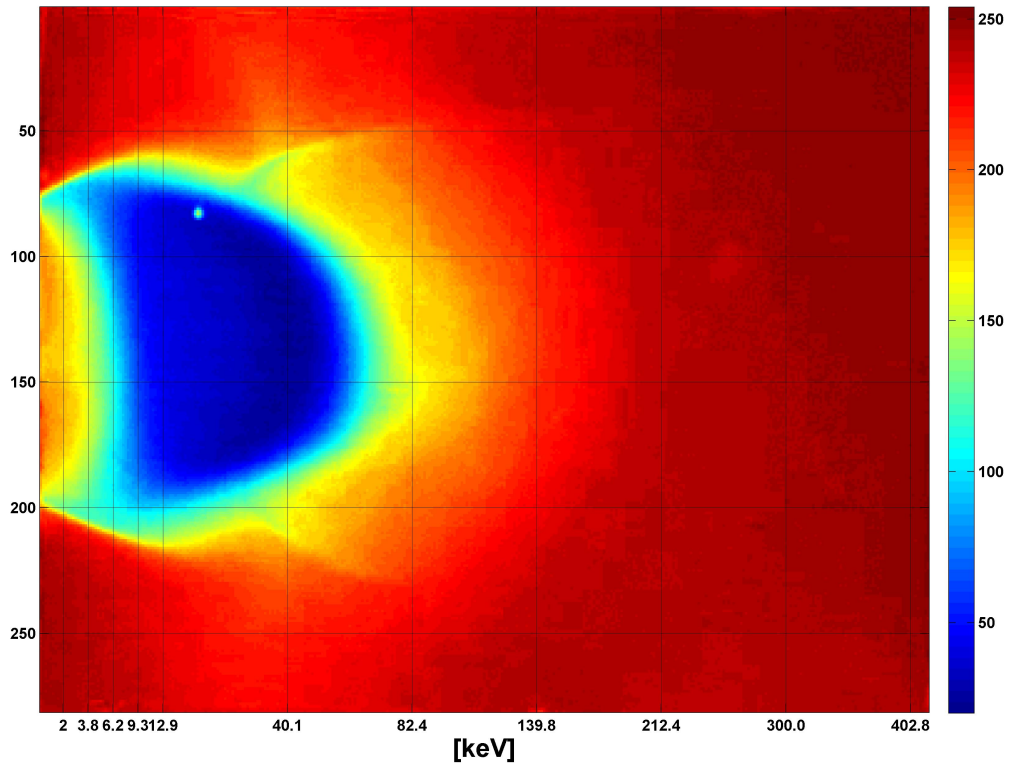
Figure 2.9 Spectrum of the electrons produced by the Plasma Focus device

smoothed taking a 9-point average.

Table 2.3 Experimental conditions and results

Thickness crossed *film type*	Sample	Profile	Voltage [kV]	Pressure [mbar]	Discharges	Offset from beam axis [mm]
0.75 µm 1HD-810 (*a*)			18	0.45	5	2.4
30 µm 1HD-810 (*a*) *1 Mylar®*			18	0.45	30	7.3
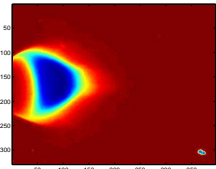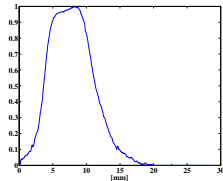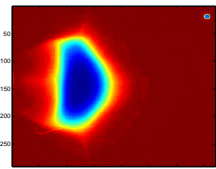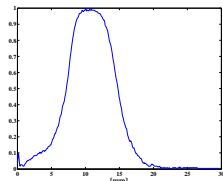
Continued in the next page

Continued from previous page

Thickness crossed *film type*	Sample	Profile	Voltage [kV]	Pressure [mbar]	Discharges	Offset from beam axis [mm]
60 µm 1HD-810 (*a*) *2 Mylar®*			18	0.45	35	9.6
80 µm 1EBT2 (*a*)			18	0.45	40	10.6
96 µm 1HD-810 (*b*)			18	0.45	60	11.0
110 µm 1EBT2 (*a*) *1 Mylar®*			18	0.45	45	11.7
126 µm 1HD-810 (*b*) *1 Mylar®*			18	0.45	80	12.2
140 µm 1EBT2 (*a*) *2 Mylar®*			18	0.45	50	13.2
156 µm 1HD-810 (*b*) *2 Mylar®*			18	0.45	100	13.7
175 µm 1EBT2 (*b*)			18	0.45	40	15
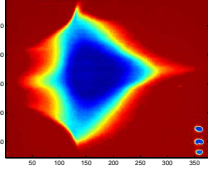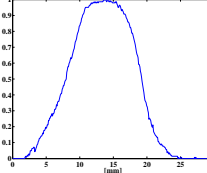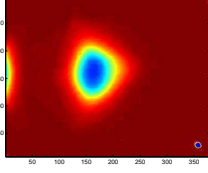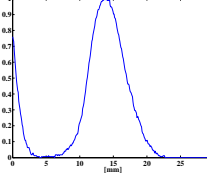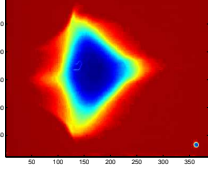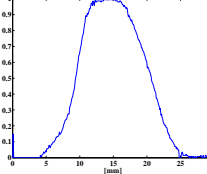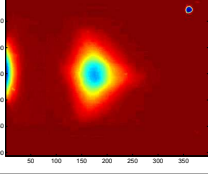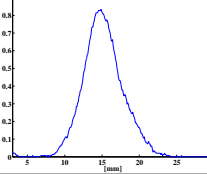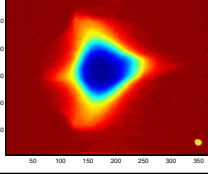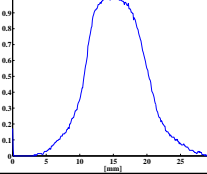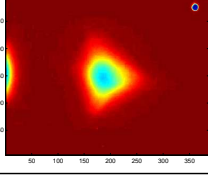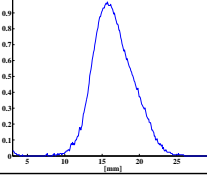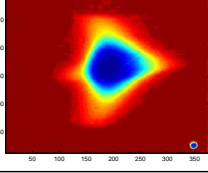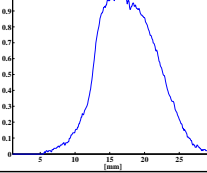
Continued in the next page

Continued from previous page

Thickness crossed film type	Sample	Profile	Voltage [kV]	Pressure [mbar]	Discharges	Offset from beam axis [mm]
205 µm 1EBT2 (b) 1 Mylar®			18	0.45	60	16
235 µm 1EBT2 (b) 2 Mylar®			18	0.45	80	16.9
256 µm 1EBT2 (b) 1 Mylar®			18	0.45	80	17.2
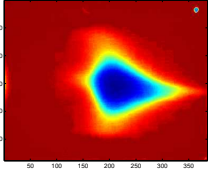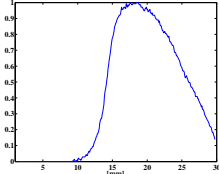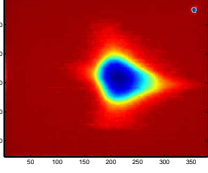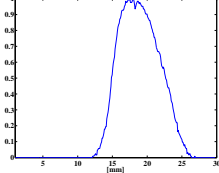
Concluded from the previous page

The profile obtained exhibits a steep increase corresponding to the transition between unexposed and exposed areas: the progressive increase, rather than a sudden jump, shows graphically the energy straggling, i.e., the energy interval spanned by the electrons with the same range. The central point of this segment is taken as representative of the energy corresponding to the particular range examined. Experimental results are summarized in Table 2.4.

The data were fitted with a 4$^\text{th}$ degree polynomials: the resulting calibration curve is shown in Fig. 2.13

The correlation factor ($R^2 = 0.9968$) and the scatter plot, Fig. 2.14, indicate a very good fitting.

The proposed method yields a reasonably accurate result with limited effort. It was possible to obtain a calibration curve, validated up to 170 keV of energy, corresponding to an elongation of ∼18 mm: this is expected to be sufficient for the present needs of qualification of the electron beam, but further extension is of course possible and will be investigated in the near future. Comparison with the original calibration (and with the 2$^\text{nd}$ order polynomial extrapolation) exhibits acceptable agreement, within 25%, showing, however, that the original calibration underestimates the energy for a given elongation. As the e-beam current in dense plasma focus devices may exceed the Alfvén-Lawson limit, there may be some uncertainty in extrapolating the present results to much higher beam intensities than measured in the present device. Simultaneous x-ray measurements may be a way to improve reliability [1].
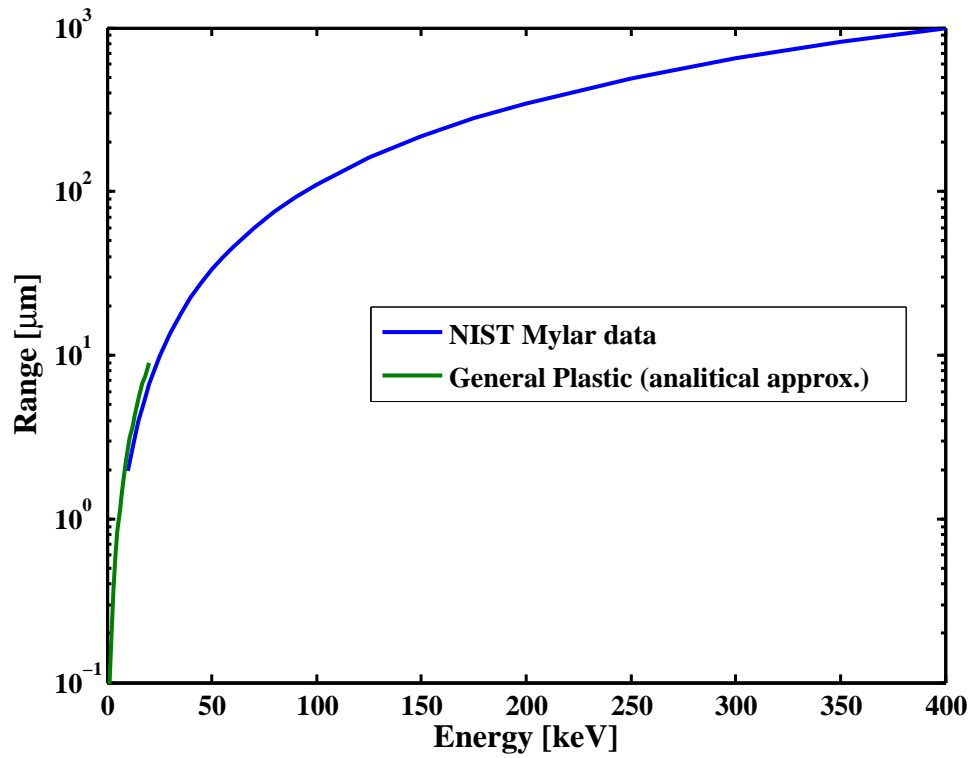
Figure 2.10   Empirical formula for general plastic for low energies and the NIST data for Mylar
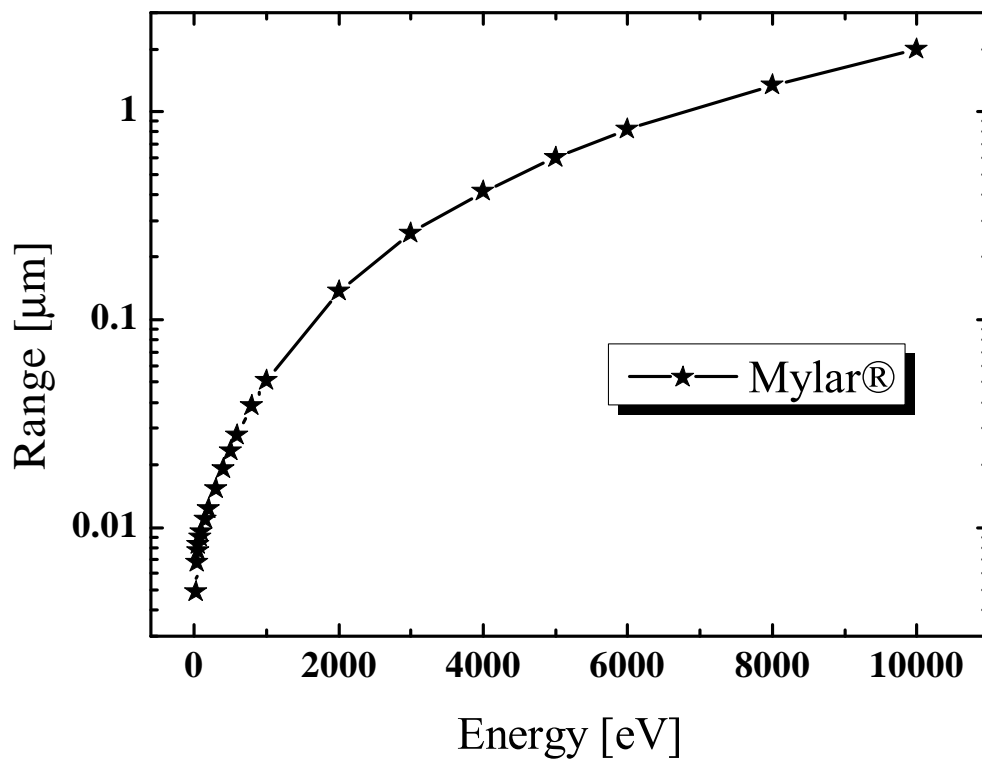
Figure 2.11   Range in Mylar®for impinging electrons with energies below 10 keV

Table 2.2 Experimental thicknesses and corresponding energies

Sample	Thickness of Mylar®[µm]	Electron Energy [keV]
1	0.75	5.7
2	30.0	47.9
3	60.0	70.8
4	80.0	83.1
5	96.0	92.7
6	110.0	100.1
7	126.0	108.8
8	140.0	115.5
9	156.0	123.6
10	175.0	132.0
11	205.0	145.2
12	235.0	157.9
13	256.0	170.0

Table 2.4 Correspondance between elongation from aperture and energies as determined from the measured range values

Elongation [mm]	Energy [keV]
0	0
2.4	5.691
7.3	47.88
9.60	70.78
10.60	83.06
11.00	92.69
11.70	100.12
12.20	108.76
13.20	115.50
13.70	123.57
15.00	131.98
16.00	145.25
16.90	157.86
17.30	169.96
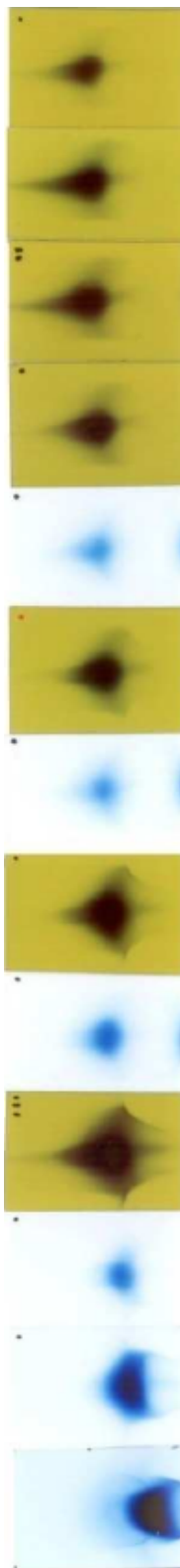
Figure 2.12   Irradiated samples

$$Y = 0.64319 - 2.7978\ X + 2.08475\ X^2 - 0.13303\ X^3 + 0.00311\ X^4$$
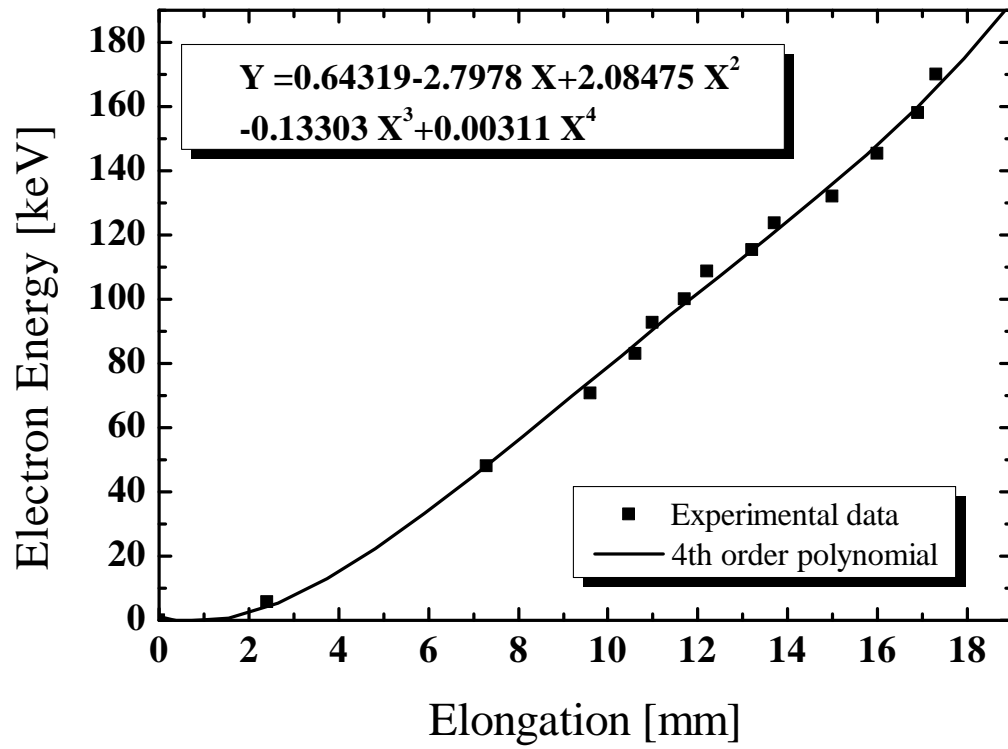
Figure 2.13 4th polynomial calibration curve
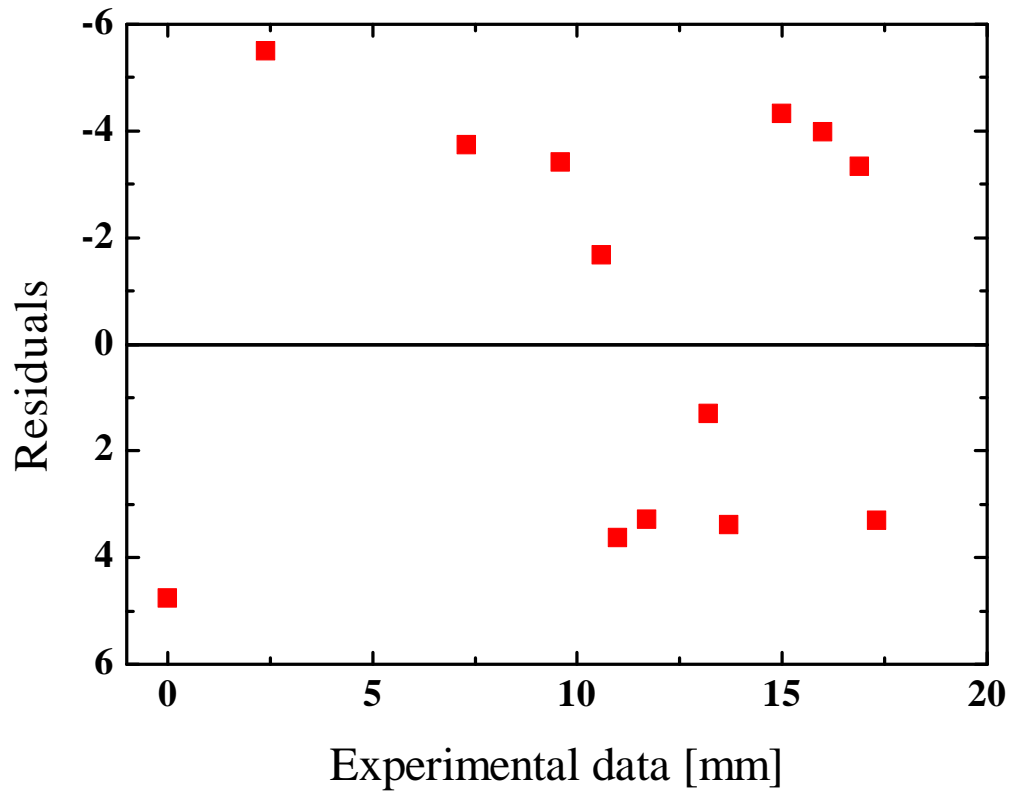
Figure 2.14 Scatter plot of the calibration curve

2.3   Energetic spectrum produced by PFMA-3

To obtain the electron spectrum the GAFCHROMIC® HD-810 film were always irradiated with 4 accumulated discharges of PFMA-3 (Fig. 2.15). It was chosen to accumulate 4 discharges to obtain more statistics, to reach the lower limit of the dosimetric range of the HD-810 GAFCHROMIC® film and yet not to saturate in the most exposed area.

The image was analyzed with the same procedure, described in the beginning of the chapter. The film was scanned into an 8-bit gray scale. The resulting digital image was treated in MATLAB®. In details it is reported the m-file of the analysis in MATLAB®.

```matlab
1  y1=double(y);
2  % Check the background
3  f=10;
4  %Background subtraction
5  y2=256-y1-f;
6  %Conversion from pixel to mm
7  x=(0:0.085:350*0.085);
8  %Elimination of disturbances
9  y3=y2(1:351);
10 for i=1:1:351
11     if y3(i)<0 y3(i)=0;
12     end;
13 end;
14 clear i;
15 %Calbration curve of 4th polynomial degree
16 x2=-0.1065+1.8638*x+0.4525*x.^2-0.0248*x.^3+0.0013*x.^4;
17 a=trapz(x2,y3)
18 y4=y3/a;
19 y5=x2.*y4;
```


Figure 2.15   Example: exposed film

```
20  %mean energy
21  em=trapz(x2,y5)
22  x3=x2−em;
23  x4=x3.^2;
24  y6=x4.*y4;
25  %standard deviation
26  sig=sqrt(trapz(x2,y6))
27  %%%%%%%%%%%%%%%%%%%%%%%%%%%p−Percentile%%%%%%%%%%%%%%%%%%%%%%%%%%%%%
28  z=cumtrapz(x2,y4);
29  p=0.01;
30  figure
31  %plot to check the background value
32  subplot(3,1,1), plot(256−y1)
33  subplot(3,1,2), plot(x2,y4)
34  %cumulate
35  subplot(3,1,3), plot(x2,z)
36  figureverbatim
37  %spectrum plot
38  plot(x,y4)
39  for i=1:1:351
40      if z(i)>p/2
41          emin=(x2(i)+x2(i−1))/2
42          break
43      end
44  end
45  for i=1:1:351
46      if z(i)>1−p/2
47          emax=(x2(i)+x2(i−1))/2
48          break
49      end
50  end
```

Background (indicated with letter "f") was subtracted and a profile through the center (center indicated with the letter "y") of the exposed area was extracted, then smoothed, taking a 9-point average, and finally the calibration curve ("x2" letter) obtained by the range method calibration was applied. The electron spectrum 3-D profile is represented in Fig. 2.16: on the z-axis is present the grey level, in the x and y axes the pixel values.

The electron spectrum is the one shown in Fig. 2.17; the mean energy is around $50\,\mathrm{keV}$ and it is possible to see tails up to $200\,\mathrm{keV}$.
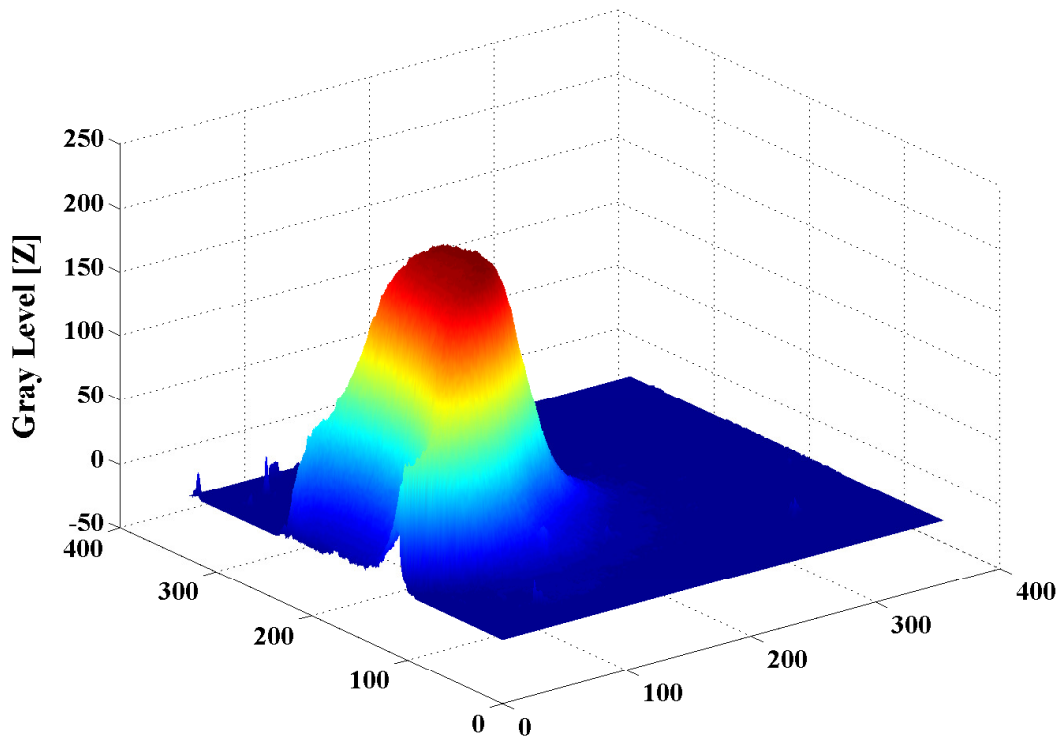
Figure 2.16   3D profile of the GAFCHROMIC® film
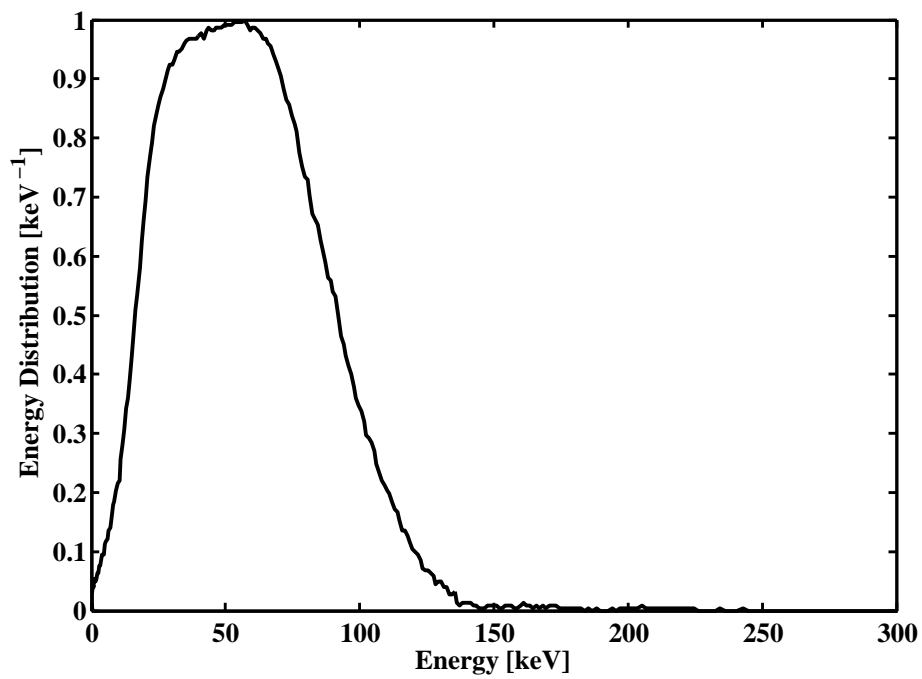
Figure 2.17   Electron spectrum produced by PFMA-3

2.4 Intensity of the electron beam

To measure the intensity of the electron beam a Rogowski coil was used.

The Rogowski coil, described in the first chapter, is based on the magnetic induction that generates an electromotive force in the coils due to the concatenation of the magnetic field variable in time, generated by the time-varying current flowing in the Plasma Focus device (Faraday Neumann Lenz law).

On the back of the electrodes an extraction tube was installed, around which is installed the Rogowski coil to measure the current of the electron beam generated by the Plasma Focus device, figure 2.18.

To measure the electron beam, as can be seen from figure 2.18, it was necessary to connect the end of the extraction tube, closed through a clamp with an iron plug, through bonding wires to the terminal part of the electrodes to make the surfaces equipotential. The Rogowski coil is connected to the oscilloscope through a shielded Huber-Suhner cable. The cable is connected in a way that it does not touch the other cables and the oscilloscope to which is the cable is connected is positioned 3 m away from the Plasma Focus device, to avoid possible electromagnetic disturbances.

The experimental measurements of the electron beam provided current value peak between 100 and 400 A and pulse durations (FWHM) of 0 1- 0.5 µs. The integration of the signal of the electron current gave an average charge value around 0.2 mC.

Figure 2.19 reports an example of signal from the electron beam (in the lower part of the figure) produced by the *pinch* shown in the upper part of the figure.

On the y-axis in the upper graph there is the time derivative of the current, in the lower graph the electron current beam. The two graphs peak simultaneously, as expected.

The intensity of the electron beam produced is calculated as:

$$0.2mC = \frac{0.001 \cdot 0.2}{1.6 \cdot 10^{-19}} = 1.25 \cdot 10^{15} [\frac{electrons}{discharge}] \tag{2.3}$$
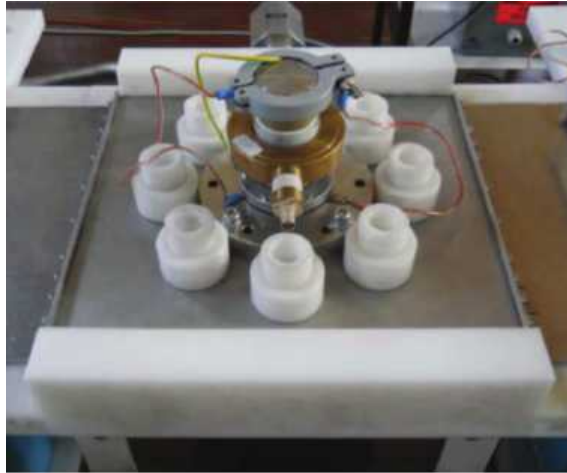
Figure 2.18   Rogowski coil positioned around an extraction tube to measure the electron beam
generated by PFMA-3 device
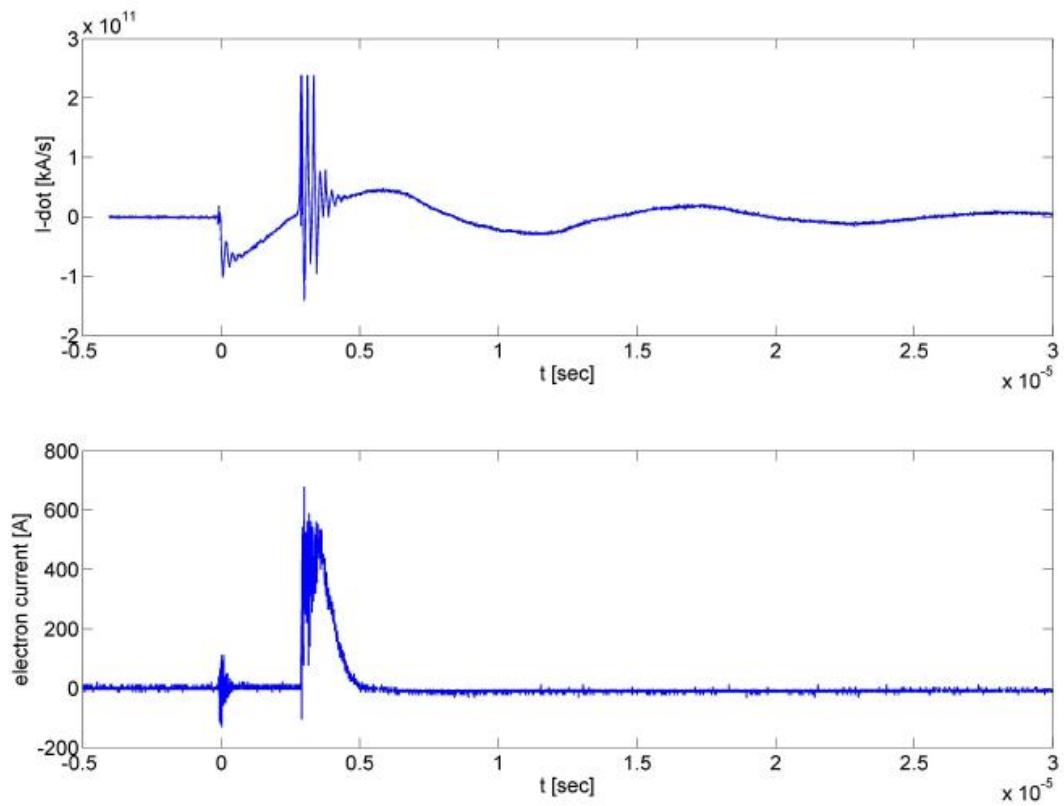
Figure 2.19   Electron beam signal: the first image is the derivative of the current of the PFMA-3,
the second one the electron beam current

Chapter 3

Dosimetry of X-rays produced by the electron beam

The electron beam emitted from the back of PFMA-3 is being studied as a radiation source for IORT, as described in chapter 1. After the drift tube positioned at the end of the electrodes, see figure 3.1, the electron beam is driven to impinge on $50\,\mu$m brass foil, where conversion x-rays are generated.

The drift tube is made of two main parts: a central steel pipe $\sim 10\,$cm long and a steel top piece. The top piece has a diameter of $11\,$cm and is $1\,$cm thick. In the center it has an aperture of $3.5\,$cm of diameter and $1\,$mm thickness. It is possible to remove this central part to change the target, it is fixed by four screws. The target has one side directed inside the vacuum chamber and the other side to the room atmospheric pressure, the sealing is realized with an o-ring.

The target has a diameter of $3.8\,$cm, but the area on which the electrons impinge has limited to $3.5\,$cm in diameter by the presence of the o-ring.

Measurements with GAFCHROMIC® film are conducted to analyze the attenuation of the x-ray beam and on the same time to assess the quality of the discharges as far as radiation production. The discharges produced by the PFMA-3 cannot be all consistently identical, and a fast, even if the working conditions are the same.

To analyze the radio-biological effectiveness of PFMA-3 device built for a medical application (see chapter 1) cell culture were irradiated.

In view of applying the device to cell irradiation, which is the object of the mentioned radio-biological investigation, a method for fast and reliable determination of the dose delivered was sought. GAFCHROMIC® film was identified as a convenient detector, and one of the aims, was to design and test a procedure, based on GAFCHROMIC® film, that would meet the expected requirements of speed and dependability. The two kind of film used for this purpose are:

- EBT2 GAFCHROMIC® film and
- HD-810 GAFCHROMIC® film
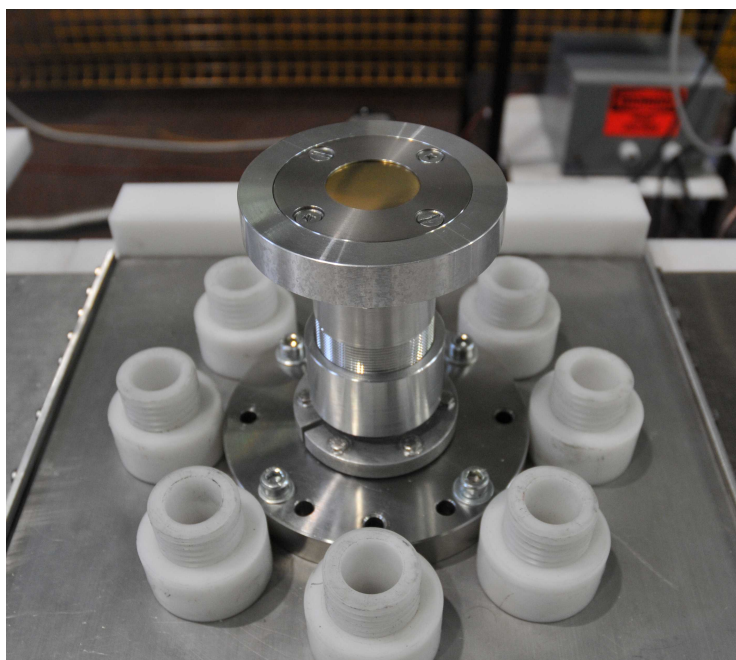
Figure 3.1   Drift tube for the electrons produced by the PFMA-3

Since some of the most energetic electrons cross the brass foil and impinge on the dosimetric material, it was found appropriate to interpose a filter, ideally one that would stop all the electrons without affecting the x-ray: the HD-810 film is apt to this purpose. The electron spectrum produced by the PFMA-3 device (chapter 2) has a mean energy around 50 keV and tails up to 200 keV; from NIST database [23] range curves can be obtained in any specified material for electrons. The material of the target is brass, in the ESTAR database [19] it is possible to choose only single material, not an alloy (with the exception of some compounds), so was selected copper. Brass in fact is an alloy made for the 64% of copper, with $Z = 29$, and for the 24% of zinc, $Z = 30$. The range curve for the electrons in copper is shown in figure 3.2.

As can be seen, electrons with energy above 153 keV are able to pass 50 μm of brass. This is why the HD-810 GAFCHROMIC® is used as a filter (it will be explained later on how). The HD-810 GAFCHROMIC® film meets the following needs: it stops all stray electrons attenuating only slightly the x-ray beam; and it affords a qualitative indication of the intensity of the mixed radiation field (electrons and x-rays) impinging on it. Since the film never saturates with the doses delivered in the present experiments, the intensity can be appraised visually by the operator from the degree of darkening of the film. Again, this appraisal cannot be but qualitative, and in relative terms: stronger or weaker discharges; yet it proves useful. No quantitative information can be drawn, given that the x-rays present have energies far below the recommended range, and anyhow the electron component is also present. Under these circumstances there is no question of calibrating this type of GAFCHROMIC® film.
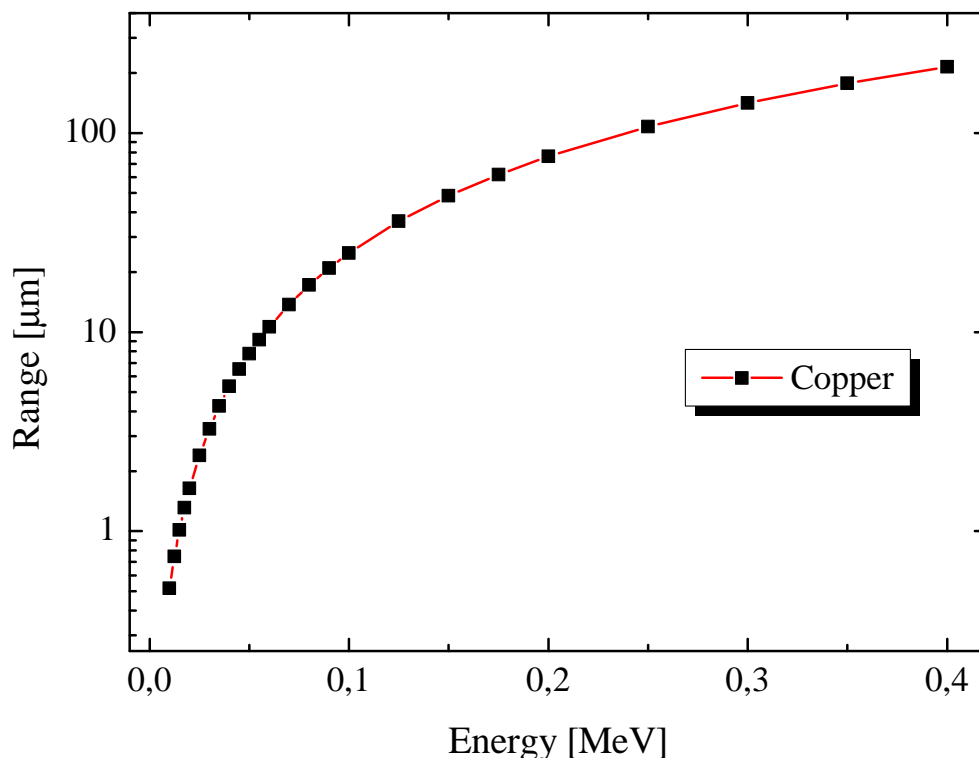
Figure 3.2 CSDA of the electrons in copper material

3.1 EBT2 Gafchromic film

These specific products have the important property of being tissue equivalent, the measurable dose range is 0.01 to 8 Gy [13]. The structure of these film sheets is already shown in chapter 2, figure 2.7, like the composition table 2.1.

The product comes in sheets, from which pieces of the appropriate dimensions (henceforth referred to as a "samples") were cut.

Care was taken to maintain the same orientation (with respect to the longitudinal direction of the original sheet) in reading all the samples, as recommended by the manufacturer.

EBT2 film can be read with a film scanner or digitizer [13]. The best response is obtained if the film is scanned in transmission mode and the spectral response of the scanner is matched to the absorbance of the film. An example of this is the Vidar DosimetryPRO Advantage (Red) scanner with the red LED light source. The LEDs in this scanner have maximum emission at a wavelength close to 630 nm and thus well matched to the spectral maximum in EBT2 GAFCHROMIC® film. It was verified that good results can be obtained scanning also in reflection mode on a flatbed scanner [24].

A calibration curve for the EBT2 film is necessary for this work: we recall that they are tissue equivalent, useful characteristic in investigating the dose deposited to the cell culture. Preliminarily a study of the energy response is needed.

Figure 3.3   Experimental set-up Comcer

Table 3.1   Sensitivity at low energy for GAFCHROMIC® EBT2 film

Beam	Energy [keV]	Z_b	Z_n	Dose [Gy]
H-30	19.7	60.0	64.6	1.01
H-60	37.3	60.8	67.5	1.00

3.1.1   Energy response of the GAFCHROMIC® EBT2 film

The producer rates the response to photons of this type of film as energy independent throughout the range 50 to 1000 keV, however its useful range can be extended to lower energies, as reported in [25].

For a further confirmation of this fact, two samples were irradiated with the same dose (1 Gy) at two different photon energies. The two irradiations were conducted at the Comecer calibration center (Centro di Taratura-COMECER SIT n.065/r Castel Bolognese, Italy), with a BALTEAU CSC320/70 x-ray tube.

The experimental setting of the Comcer center is shown in figure 3.3.

In figure 3.3 it is possible to see the x-ray tube and the plexiglas support where the film was positioned.

The ISO-4037 specified H-30 and H-60 beams (ISO-4037-1, 1998) were selected, because comparable to the x-rays produced by the PFMA-3 device. The working parameters of the H-30 beam are as follows: voltage: 30 kV; current: 14 mA; additional aluminum filter: 0.52 mm. These conditions produce a continuous spectrum with a mean energy of 19.7 keV, figure 3.4. The working parameters for the H-60 beam are: voltage: 60 kV; current: 11 mA; additional aluminum filter: 3.2 mm. The continuous spectrum produced has a mean energy of 37.3 keV, figure 3.4.

The results, in terms of levels of grey, are presented in table 3.1.

Z_b is the background grey level and Z_n the net grey level after subtraction of the background value. To calculate the sensitiveness it is necessary first to normalize the Z_n value of one beam with respect to the other. The H-30 beam was normalized with respect
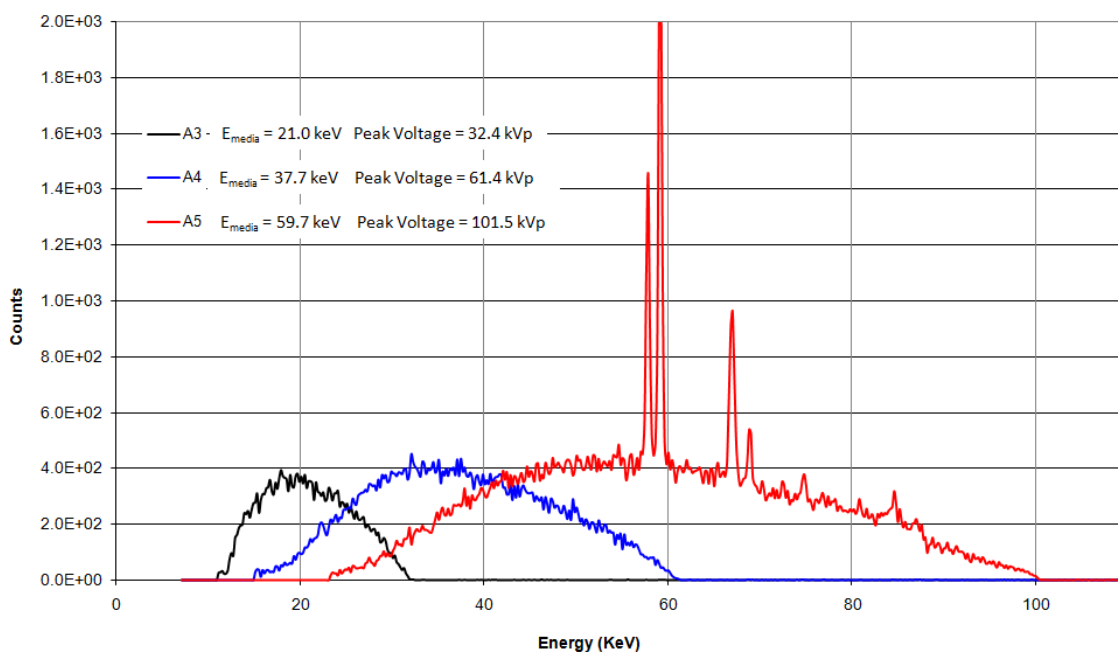
Figure 3.4 X-ray spectrum: H-30 H-60 beam

to H-60 beam, with the formula 3.1.

$$\frac{Z_{\text{bH-60}}}{Z_{\text{bH-30}}} \cdot \frac{D_{\text{H-60}}}{D_{\text{H-30}}} \cdot Z_{\text{nH-30}} = \frac{60.8}{60} \cdot \frac{1}{1.01} \cdot 64.6 = 64.8 \tag{3.1}$$

The difference found between the two beams is of the order of 4%, confirming further that GAFCHROMIC® film can be utilized at the energies, lower than 50 keV, of interest to the present work.

3.1.2   Dose calibration

The response of EBT2 GAFCHROMIC® film is not linear with dose, therefore a number of experimental points is needed to determine a calibration curve. To this end, measurements were performed with the Philips MG323 x-ray tube operated by the Radiation protection Institute of ENEA in Bologna (Centro di taratura-Istituto di Radioprotezione, ENEA, Bologna, Italy) [26].

The experimental setting of the film sheets irradiation is shown in figure 3.5.

The beam utilized is the above mentioned H-30, as the spectrum emitted compares well to the one produced by PFMA-3 (see chapter 4). Twenty samples of size 2×2 cm, were positioned on a plexiglas holder (Fig. 3.6) at 60 cm from the focus of the tube, and were given 20 different dose values.

Figure 3.7 shows the twenty irradiated samples.

The results are presented in Tab. 3.2, where Z_b and Z_n have the meaning already discussed, whereas $STD(Z_n)$ is the standard deviation calculated from the readings of all the pixels in the exposed surface.
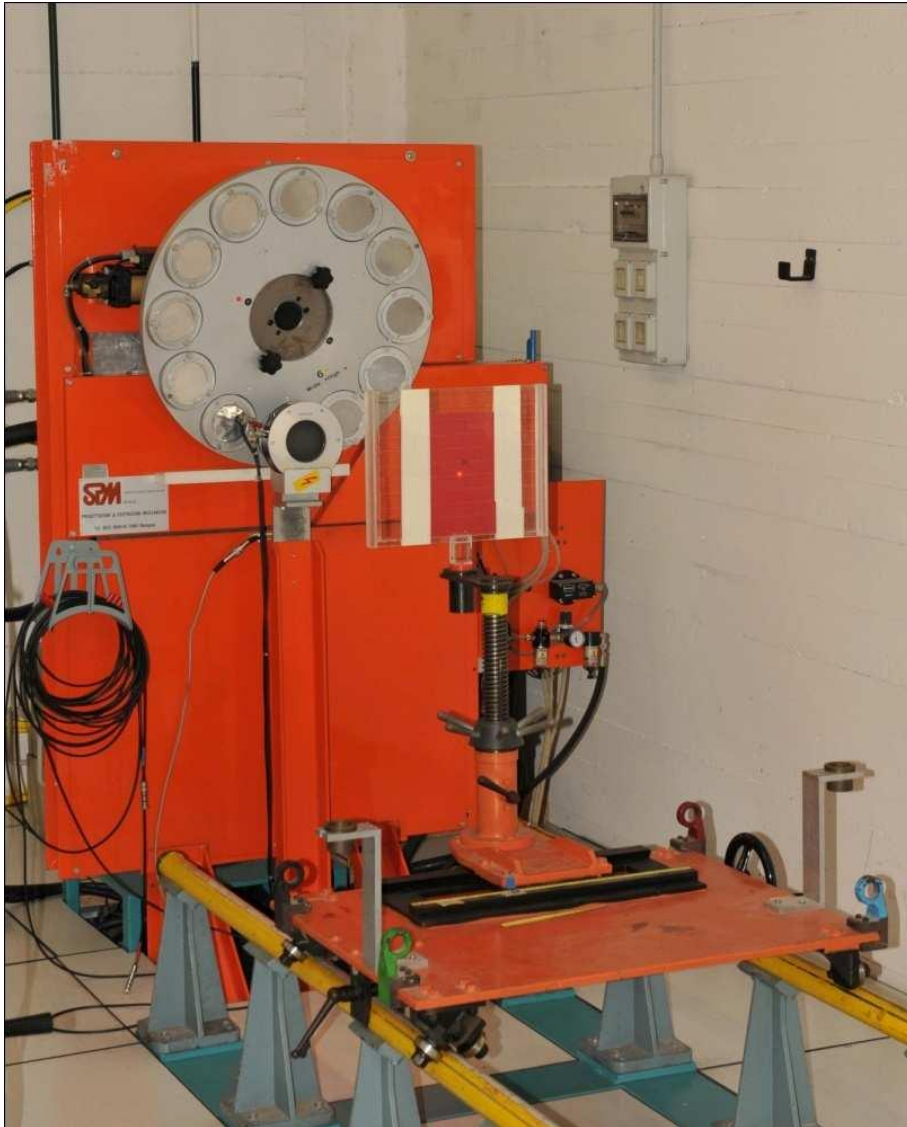
Figure 3.5   Experimental setting of the irradiations in the Enea centre

It was observed that doses of 7 and 8 Gy produce grey levels that are too close. Therefore, EBT2 film will not be used in the present work for doses above 7 Gy.
The calibration curve, shown in Figure 3.8, is obtained from the 20 experimental values fitted with a 4th order polynomial, as in the equation 3.2.

$$y = 0.12176 - 0.01296x + 8.21246 \cdot 10^{-04}x^2 - 9.03169 \cdot 10^{-06}x^3 + 4.12383 \cdot 10^{-08}x^4 \quad (3.2)$$

The dose "y" in equation 3.2 is expressed in gray, "x" is the Z_n level. At each value is associated an error bar of $\pm 2.5\%$ on the y-axis, which is the reported uncertainty in the dose delivered by the x-ray tube. The quantity on the horizontal axis is the net grey level value after subtraction of the background. The correlation factor ($R^2 = 0.9995$) and the scatter plot, Fig. 3.9, indicate a very good fitting.
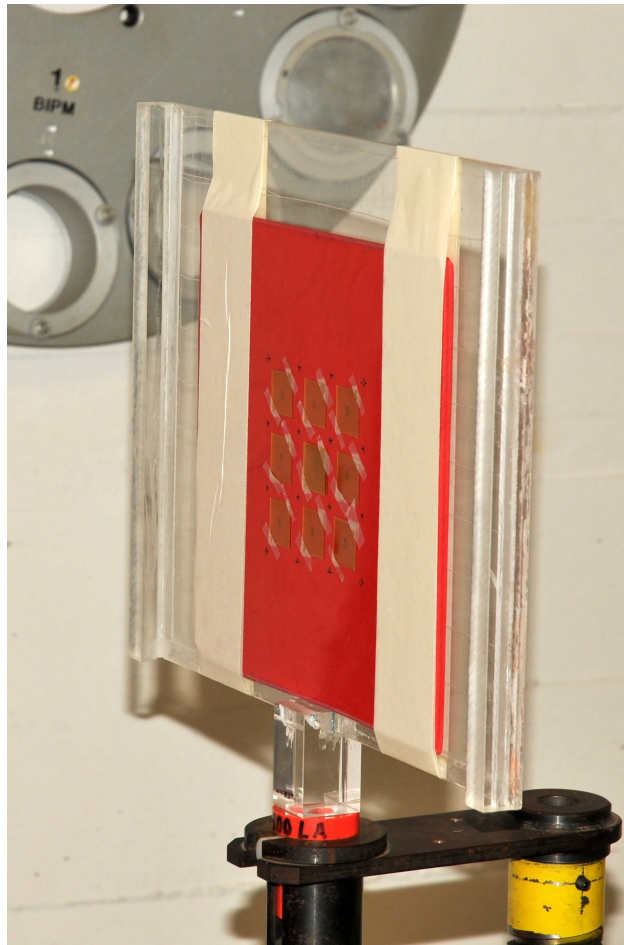
Figure 3.6   Plexiglas support for the irradiation of the GAFCHROMIC® film

An additional experiment was carried out: there are two irradiations at the same dose: 1 Gy, as it is possible to notice from table 3.2. The film samples were placed one above the other, to verify that at the energy of 20 keV, which is the average energy spectrum of the beam H-30 used for irradiations, the polyester material which is the main component of GAFCHROMIC® EBT2 film, would not produce beam attenuation (see transmission curves of Mylar,3.10).

It is possible also to make a comparison between the samples irradiated with the same doses (1 Gy), but in different calibration centers. For the Comecer center, the sample irradiated with the beam H-30, the same used for the calibration samples irradiated in the Enea center, was considered. The data are presented in table 3.3:

Making a comparison between the samples, it is possible to notice that the relative error between them is < 1%, proving that the irradiation method is appropriate and the dose reading is correct.
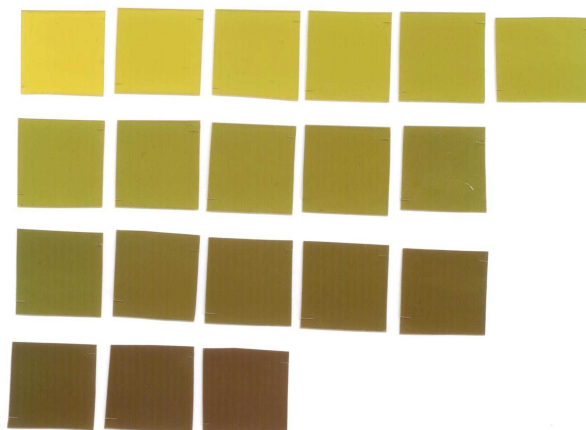
Figure 3.7   Twenty Gafchromic irradiated film for the calibration curve

Table 3.2   Grey values in the irradiated samples

Dose [Gy]	Z_b	Z_n	STD(Z_n)
0.05	55.9	6.9	0.19
0.1	56.1	15.6	0.26
0.3	58.7	29.7	0.21
0.5	56.1	44.7	0.31
0.6	54.2	46.6	0.35
0.7	55.8	53.2	0.09
1	56.9	64.7	0.23
1	54	65	0.21
1.3	56.2	76	0.36
1.5	55.3	84.4	0.37
1.7	56.7	88.6	0.21
2	55.1	98.1	0.18
2.5	56.3	105.5	0.32
3	56.1	115	0.38
3.5	55.3	122.3	0.34
4	55.7	127.3	0.27
4.5	55.1	132.4	0.29
5	54.6	136.9	0.39
6	55.9	144.1	0.25
7	55	149	0.33
8	54.5	150	0.19

Model	Polynomial
Adj. R-Square	0.99947
	Value
Intercept	0.12176
X1	-0.01296
X2	8.21246E-4
X3	-9.03169E-6
X4	4.12383E-8
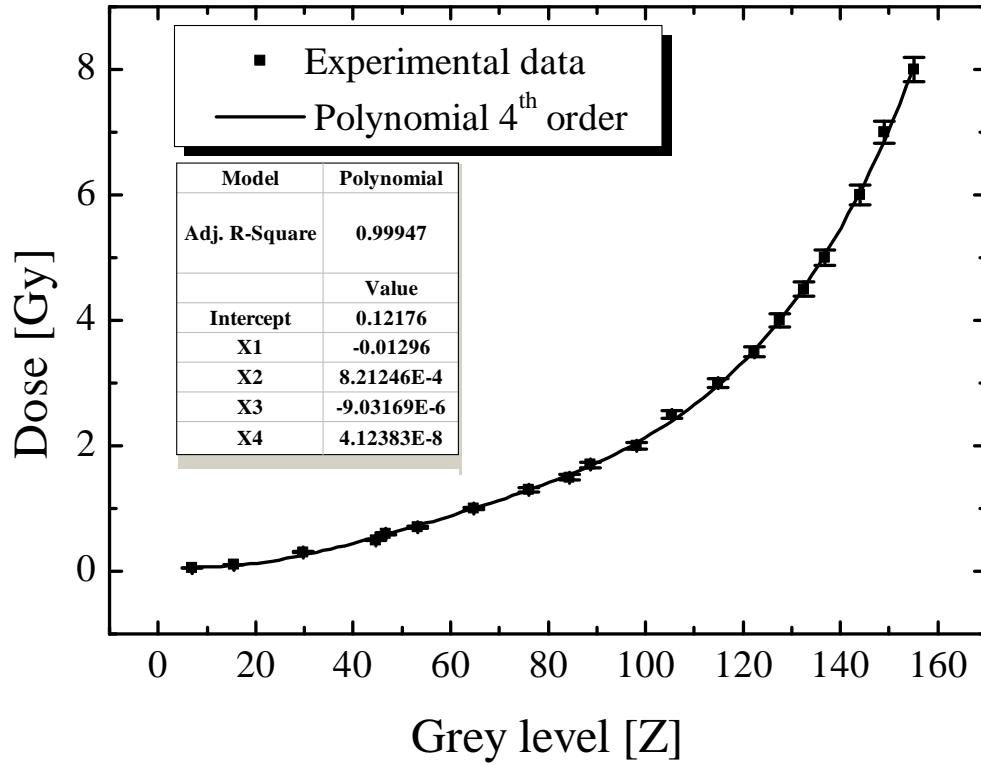
Figure 3.8 Calibration curve for GAFCHROMIC® EBT2 film
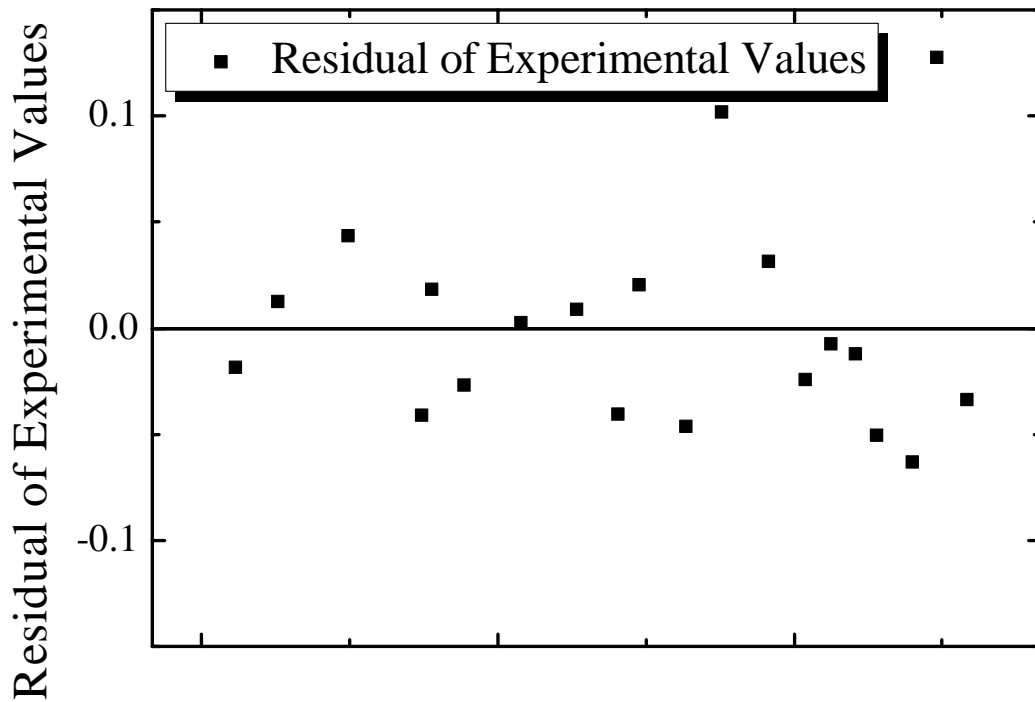
Figure 3.9 Residual values
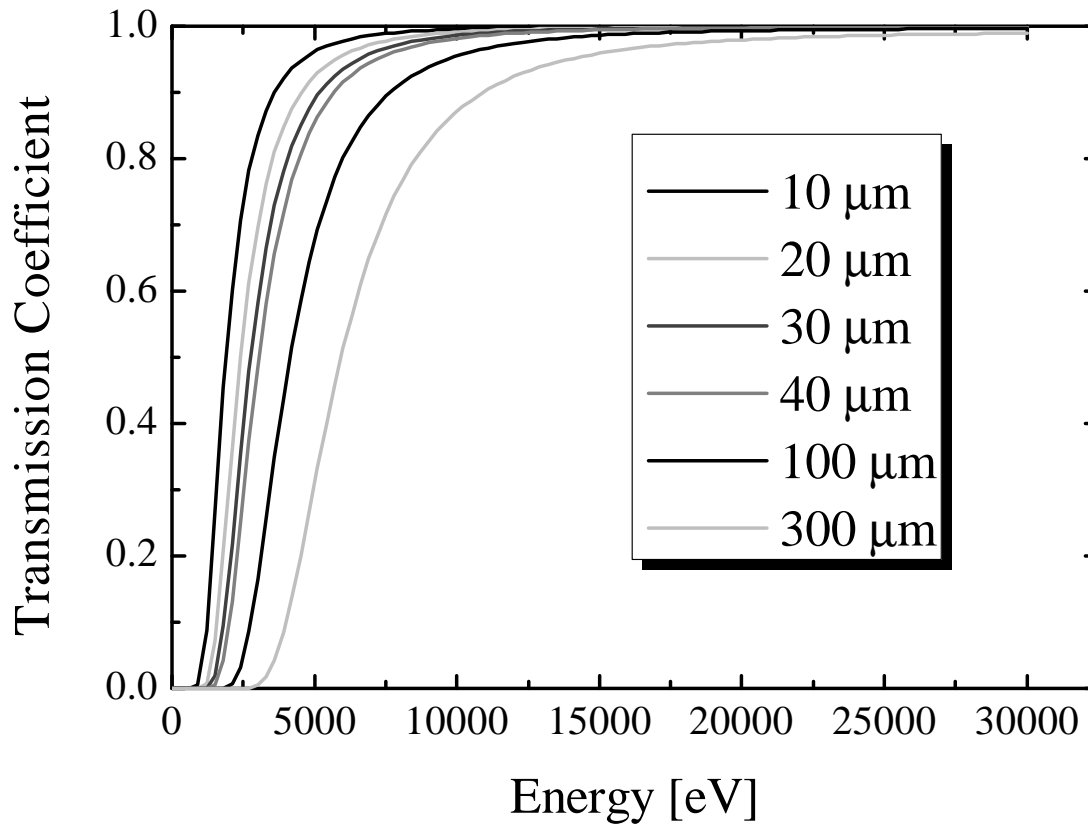
Figure 3.10   x-rays transmission coefficient for Mylar® foil of different thicknesses

Table 3.3   Comparison of the GAFCHROMIC® film irradiated with the same doses

Center	Dose [Gy]	Z_b	Z_n
Comecer	1	60.0	64.8
Enea 1	1	56.9	64.7
Enea 2	1	54.0	65.0

3.2 HD-810 Gafchromic film

The other GAFCHROMIC® film used in this campaign is the HD-810 film sheets that have the composition and the structure shown in Fig. 3.11 [12]. This type of film is designed to measure absorbed dose from high-energy photons or electrons. The response of this film is energy-independent for photons above 0.2 MeV and is linear with dose. The rated dose range is 10 to 250 Gy.

In the present work, however, this GAFCHROMIC® film is used with two different purposes: one in the attenuation measurements and radiobiological ones, since some of the most energetic electrons cross the brass foil and impinge on the dosimetric material, it was found appropriate to interpose a filter, ideally one that would stop all the electrons without affecting the X-rays, the second one, the most important, to measure with the magnetic spectrometer the electron spectrum, described in this chapter.

They have a privilege side, the one with 0.75 µm recognizable, for electrons, because the electrons have a small range. In these case they have to cross only 0.75 µm of thickness to blacking the film.
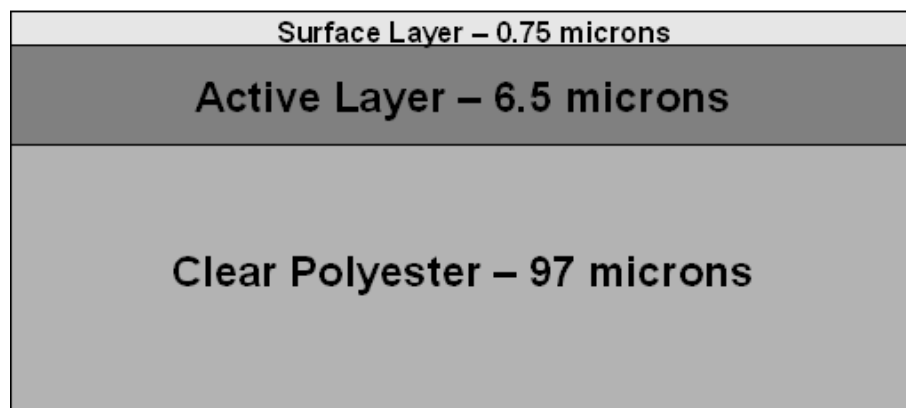
Figure 3.11   GAFCHROMIC® film: HD-810

3.3 Cell culture irradiations

For the radiobiological investigation planned, electrons produced in the pinch phase will be directed onto the brass target to produce x-rays, which will in turn irradiate a cell culture contained in a holder specifically designed, see figure 3.12, that is positioned at the end of the electron extraction tube, after the brass foil, see figure 3.13.

The holder is comprised of a hollow, cylindrical central piece 3 cm long and with a 3.9 cm inner diameter, threaded at both ends to accommodate sealing end pieces. All the parts of the cell holder are made of stainless steel. The end piece toward the brass converter has a 3.5 cm diameter aperture, and is sealed with a 30 µm Mylar® foil seated between the central body and the end piece. The cell culture is contained inside the holder, resting on
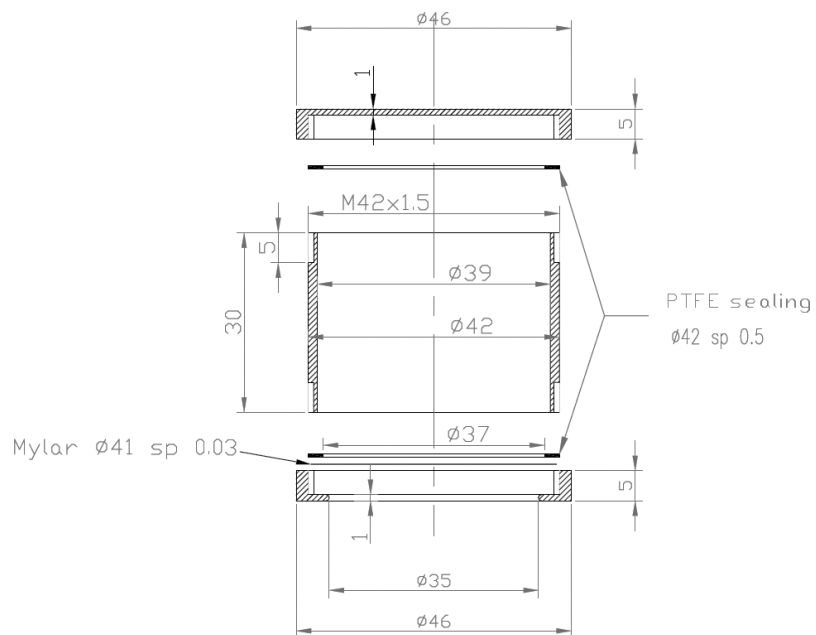
Figure 3.12 Cell culture holder
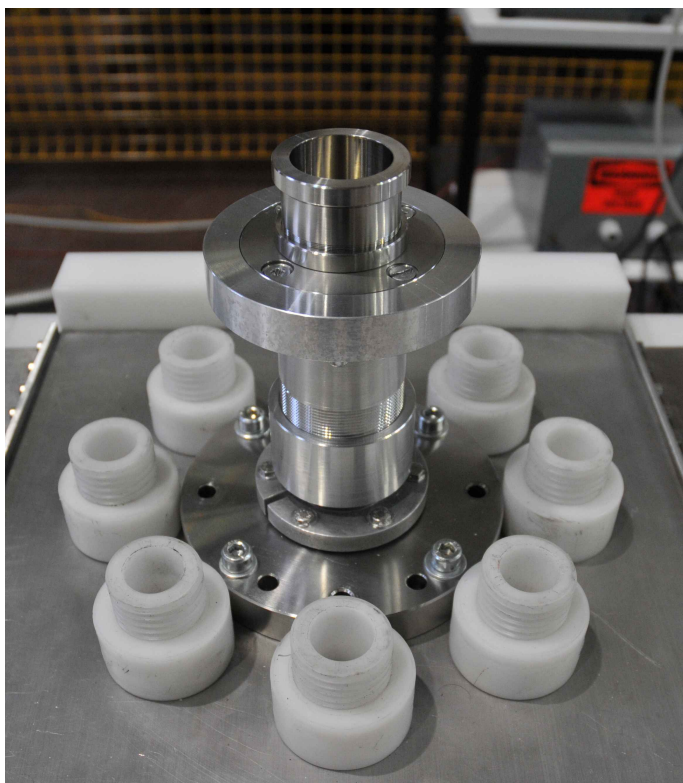
Figure 3.13 Cell culture holder positioned at the end of the extraction tube

the Mylar® foil. The central body and the end pieces are closed mechanically pressuring the Mylar® foil on a Teflon o-ring, which has a rectangular section. Chapter 6 will be dedicated to the design development of the cell culture holder.

To assess the dose delivered to the cells a stack of film was inserted between the brass foil and the cell holder. The idea was to measure the dose to the last GAFCHROMIC® film layer (the one immediately adjacent to the Mylar® foil of the holder) and from that infer the dose to the cell layer.

To this end the cell layer was simulated with a further film layer (the absorption in the Mylar® foil was neglected): so the layer could be added to the stack, this latter irradiated, and the doses to the film layers measured.

Repeating the experiment a sufficient number of times, the relationship between the dose to the extra layer and the dose to the layer immediately preceding it could be determined. Hence, determination of this latter dose will serve to appraise the dose to the cells [26].

3.3.1   Dosimetric Stack

Initially, a stack of 5 GAFCHROMIC® EBT2 films was used, as presented in figure 3.14, and series of 5 discharges were loaded on the stack. However, for the reasons discussed previously and because of the high doses present, the first two films were completely saturated, and occasionally also the third. It was chosen to limit the number of discharges per run to only 4 and to use as first layer the HD-810 film. This configuration is also shown in figure 3.14 on the right side.

   Both HD-810 and EBT2 films are all consistently positioned with the thinner coating (0.75 µm and 80 µm) facing toward the incoming beam. The sample area is 4.5×4.5 cm. On the left side, figure 3.15 shows the positioning of the film stack at the end of the electron drift tube, on the right side the blackening of the film sheets after the irradiation.

   Figure 3.16 presents an example of all the film sheets after an irradiation.

   The GAFCHROMIC® film, as usual, were scanned on an HP Laser-Jet M1522 nf in reflection mode, at 300 dpi resolution, the image converted to an 8-bit grey scale (256 shades of grey) and then analyzed in Matlab. The input of the analysis in Matlab of each dose evaluation is presented below:

```
1  close all
2  data1=double(data);
3  data2=256-data1;
4  % background calculation
5  % Selection of an area that represents the background
6  Mfondo=data2(10:50,10:50);
7  %
8  subplot(2,1,1), surf(data2), shading interp
9  %
10 subplot(2,1,2), surf(Mfondo), shading interp
```

```
11  %
12  % calculation of the background mean and
13  %the standard deviation of the background
14  fondo=mean(mean(Mfondo))
15  sigmafondo=std(std(Mfondo))
16  %subtraction of the background
17  d=data2-fondo;
18  %
19  %% EBT2 calibration curve
20  %
21  data3=0.00000004*(d.^4)-0.000009*(d.^3)+0.0008*(d.^2)-0.013*(d.^1)+0.122;
22  %
23  [M,N]=size(data3);
24  % removing of the negative values
25  for i=1:1:M
26      for j=1:1:N
27          if data3(i,j)<0 data3(i,j)=0;
28          end;
29      end;
30  end;
31  clear i
32  clear j
33  %smoothing of each value for the lines
34  for i=1:M
35      %for j=1:N
36      %    y(j)=data3(i,j);
37      %end
38      y = data3(i,:);
39      % Smooth each 7 points
40      y2=smooth(y,7);
41      %for j=1:N
42          %data3(i,j)=y2(j);
43      %end
44      data3(i,:)=y2;
45  end
46  %smooth for each values for the columns
47  for j=1:N
48      %for i=1:M
49      %    y(i)=data3(i,j);
50      %end
51      y=data3(:,j);
```

```
52        y2=smooth(y,7);
53        %for i=1:M
54            %data3(i,j)=y2(i);
55        %end
56        data3(:,j)=y2;
57    end
58    figure
59    %contourf to plot isodoses
60    contourf(data3,0:0.5:8.0), colorbar
61    figure
62    %3D graph
63    surf(data3), shading interp
```

In the first part of the input the background area, the mean of the background and the standard deviation are determined. After the average level of grey Z_n in the most exposed area was determined, with the calibration curve (equation 3.2) the Z_n values were converted to doses. Figure 3.17 and figure 3.18 represent the post-processing of the analysis in Matlab of the previous irradiation: the first image is the 3D representation of the dose deposited, while the second shows the isodose surfaces.

Figure 3.19 is a representation of the last three film with a more appropriate domisimetric scale.

It can be seen that the last three film sheets have less attenuation between them, this means that the energy of the x-ray beam is higher than the precedent film and because in the first and second film there is a mix field of irradiation: electrons and x-rays. These considerations will be found in a good agreement with the Monte Carlo simulations described in chapter 4.
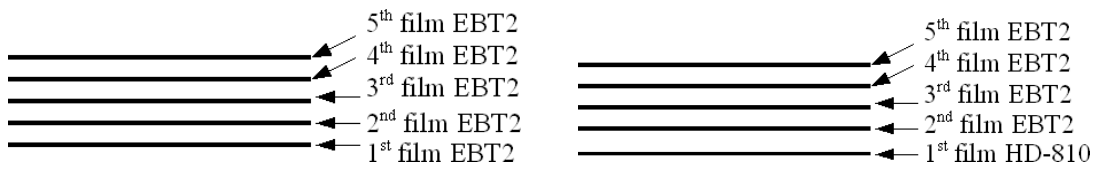
Figure 3.14   5 GAFCHROMIC® EBT2 film: 1st configuration of stack; 4 GAFCHROMIC® EBT2 plus 1 HD-810 film: 2nd configuration of stack
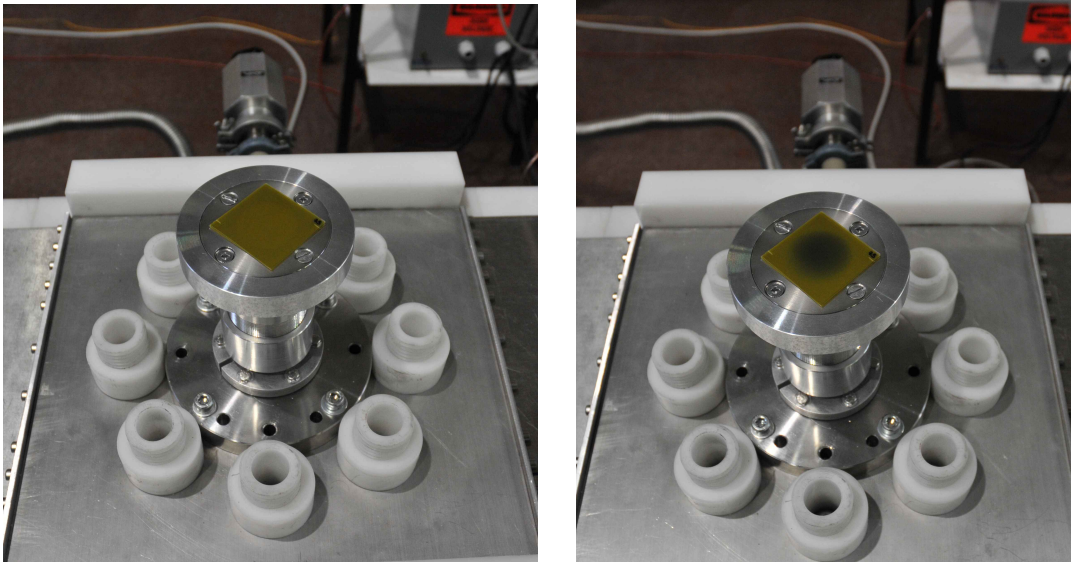
Figure 3.15   Positioning and irradiation of the Gafchromic film
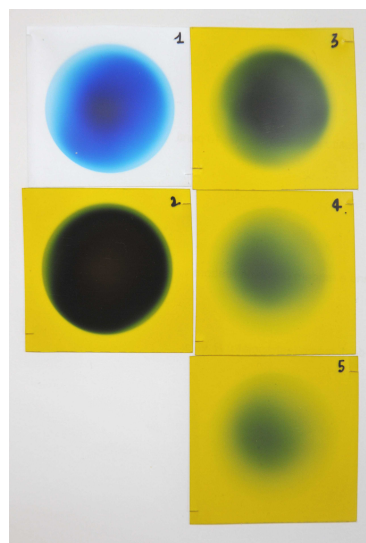
Figure 3.16   Irradiation example of 5 GAFCHROMIC® film: 1 HD-810 + 4 EBT2
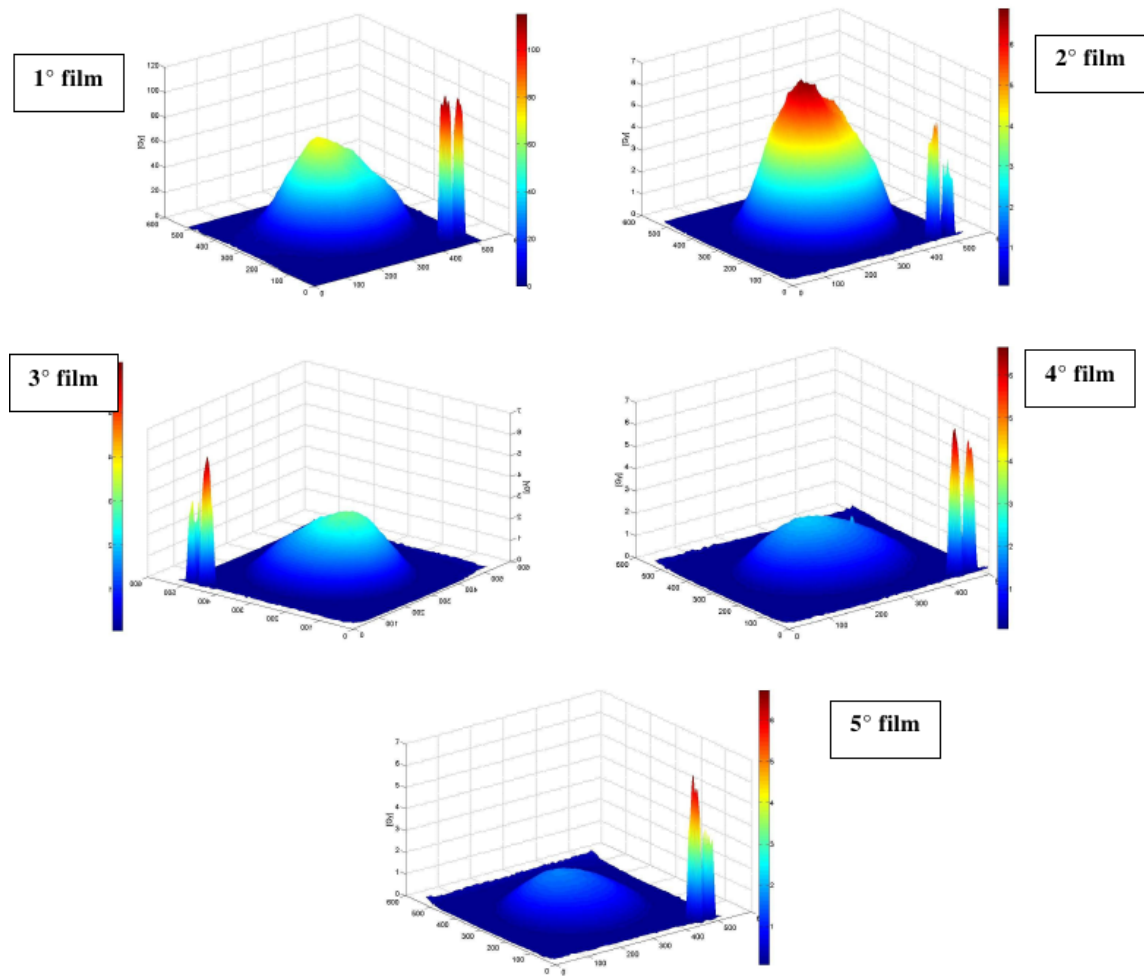
Figure 3.17   Matlab analysis: 3D Isodose level (dose expressed in gray)
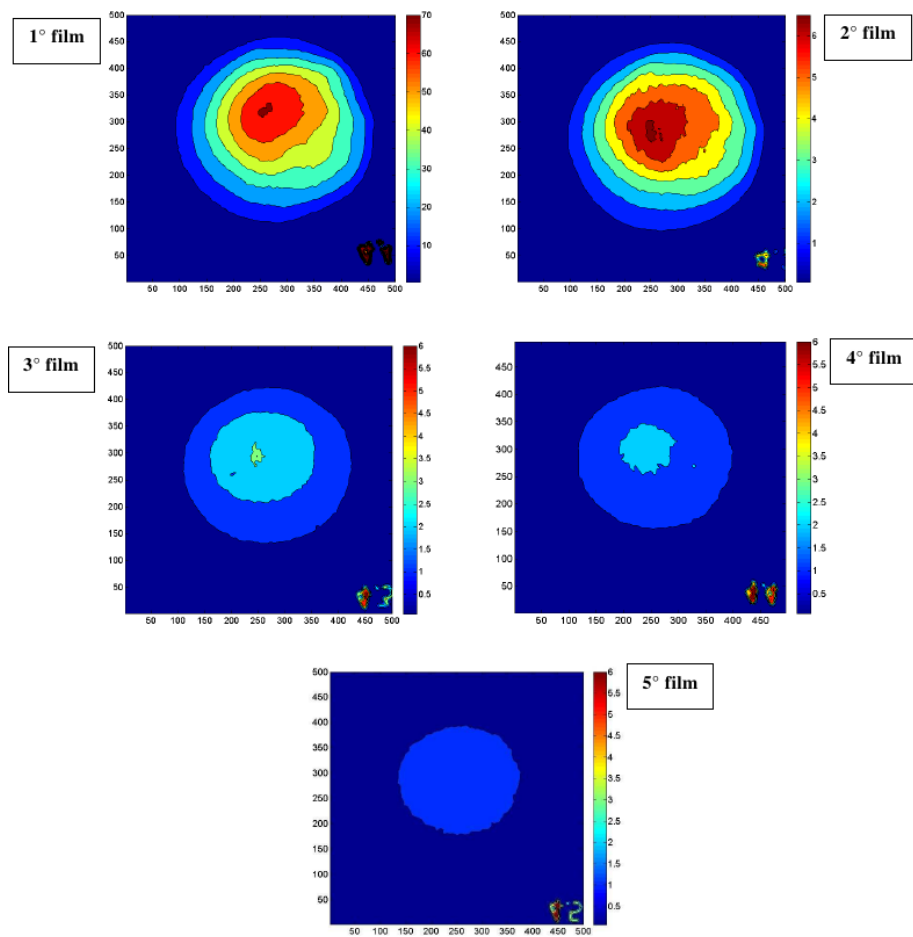
Figure 3.18   Matlab analysis: Isodose surfaces (dose expressed in gray)
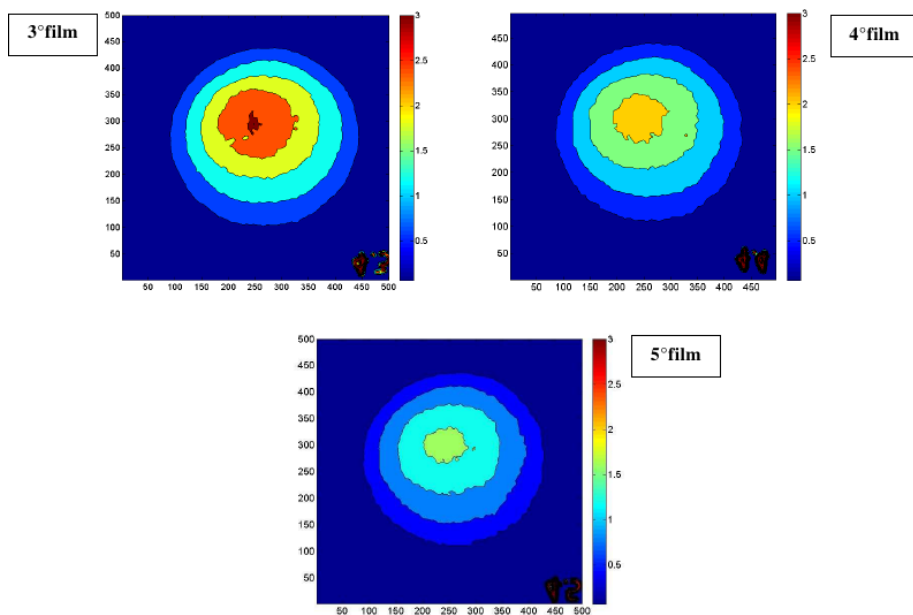
Figure 3.19   Matlab analysis: Isodose surfaces with a more proper dosimetric scale (dose expressed in gray)

3.4 Results of the attenuation measurements

Table 3.4 is an example of the results in dose value of an irradiation measurement.

Table 3.4 Results of one series of 4 discharges loaded on 5 GAFCHROMIC® film

	1st film (HD-810)	2nd film (EBT2)	3rd film (EBT2)	4th film (EBT2)	5th film (EBT2)
Z_b	1	88	90	89	90
Z_n	130	150	116	103	90
Dose [Gy]		7.1	3.0	2.2	1.8

Dose values for the first layer are not meaningful, since they receive a mixed field: electrons plus photons, as discussed in chapter 4.

The experimental campaign was conducted running 5 series of 9 repeated measurements (each of them counting 4 discharges), and a correlation between the doses to the 4th and 3rd film, as well as that between the doses to the 5th and 4th, was determined. Figure 3.20 presents the results of one such series (9 measurements), reporting the ratio between doses to the 4th and 3rd film and that between the doses to the 5th and 4th film.

It can be seen that the ratio of doses to films 4th to 3rd presents much less fluctuation, and was therefore chosen as the best configuration: one sheet of HD-810 film, used as a filter, followed by two sheets of EBT2 films, then the cell holder.

The same pattern was observed in all the measurements of the 5 series, and the overall average ratio between the doses to the 4th and 3rd film was calculated at 0.78 ± 0.03. Therefore the dose is read from the 3rd film, and multiplied by the average ratio to estimate the dose to the cell culture [26].
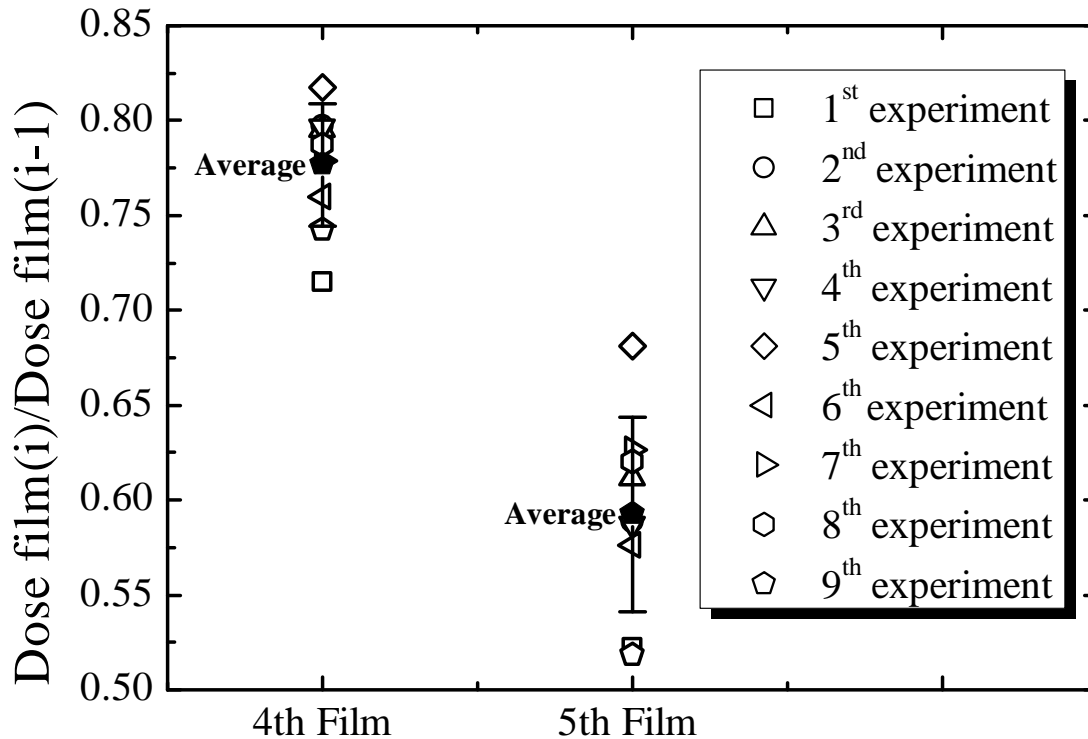
Figure 3.20   Example of measurements campaign

3.5   Attenuation in the Mylar foil

It remains to be ascertained that the attenuation in the Mylar® foil is indeed negligible. Figure 3.21 (Center for X-Ray Optics, [27]) shows the transmission coefficient for varying thicknesses of Mylar® as a function of photon energy. Of interest here the curve for $30 \, \mu m$ thickness of the foil used for the culture cell holder.

To investigate the attenuation in the Mylar® foil, two sets of experiments were conducted, with two different film stack schemes. In the first set the initial stack was used, 5 EBT2 type sheets to which a Mylar® foil disc was added between the 1th and the 2nd film, see figure 3.22.

The second set of measurements was conducted using the final stack, as described in the previous paragraph, in which the same Mylar® foil disc of $1.5 \, cm$ diameter was inserted between the 3rd and the 4th film, see figure 3.23.

The irradiation results of these measurements are shown in figure 3.24, for the first configuration.

Figure 3.25 shows quite clearly the difference in the grey level of the second film between the area covered by the foil and the rest of the exposed area.

The grey level values were averaged in the area covered by the disc and in the rest of the exposed area and the background subtracted from both values: the resulting Z_n within
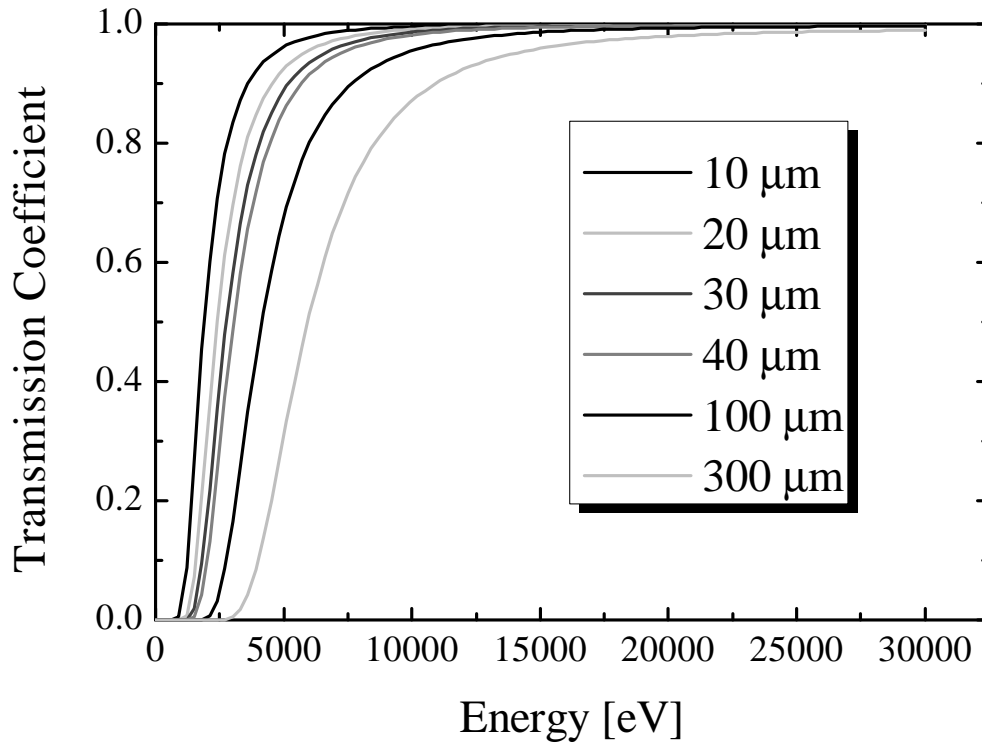
Figure 3.21 X-rays transmission coefficient for Mylar® foil for different thicknesses
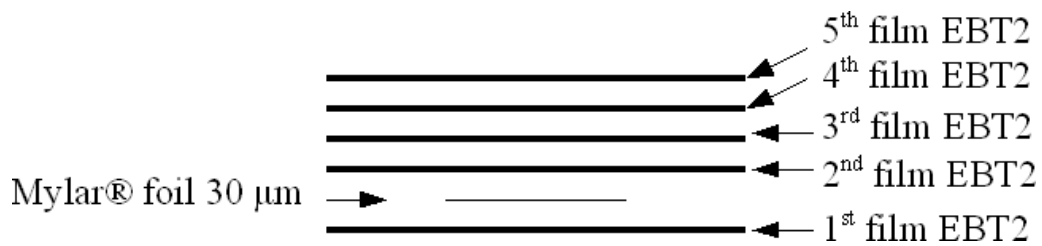
Figure 3.22 First configuration: foil between the first and second film
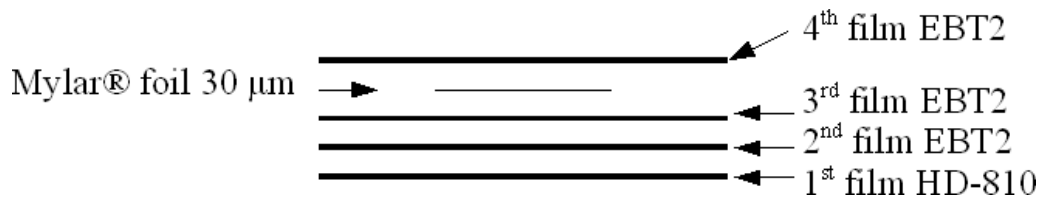
Figure 3.23 Second configuration: foil between the 3rd and the 4th film
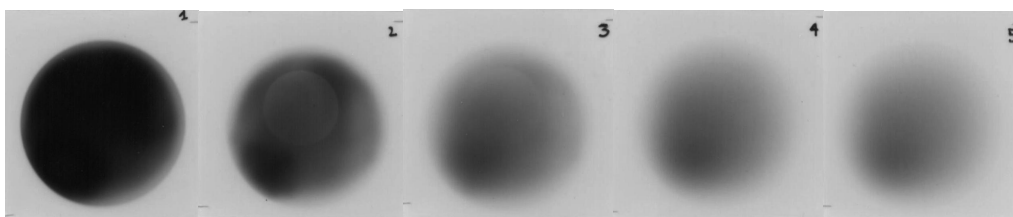
Figure 3.24   Irradiation results of the first configuration: foil between the first and second film
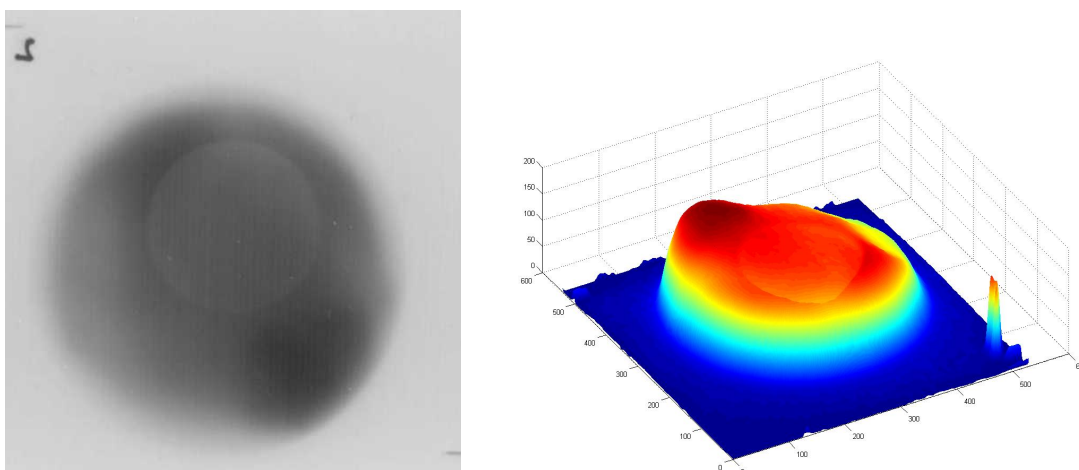
Figure 3.25   Second GAFCHROMIC® film and the analysis in Matlab

the covered area is 148.1; instead outside the covered area 153.4, confirming the difference detected visually.

It may be noted incidentally that since the above values show attenuation in the $30\,\mu m$ Mylar® foil, they confirm the existence of a component below $30\,keV$ in the photon spectrum. This difference can be noticed also in the third film, provoking that this component below $30\,keV$ is still present although weaker.

The irradiation results for the second configuration are shown in figure 3.26.

For the second configuration no variations in grey scale due to the presence of the foil was detected, or in other words, the transmission in Mylar® was essentially 100%.

This also indicates that photons capable of reaching the Mylar® foil have energies above $30\,keV$.
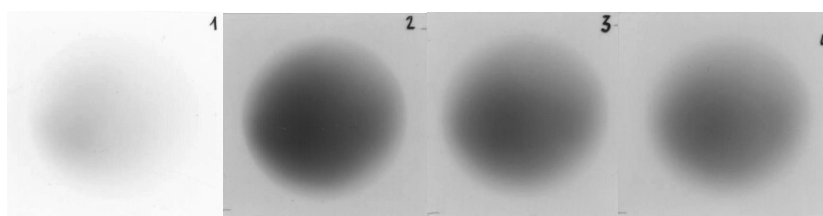
Figure 3.26   Irradiation results of the second configuration: foil between the 3rd and the 4th film

All these considerations will find a good agreement in the Monte Carlo simulations, described in the following chapter (4).

3.6 Experimental measurements of isotropy

Experimental measurements were conducted to investigated the isotropy of the x-ray beam produced by the PFMA-3 device. A sheet of film was positioned as shown in the figure 3.27. Two small rectangular blocks were positioned immediately after the aperture to hold the piece of film in place. The length of the GAFCHROMIC® film is calculated from the 3.5 cm diameter of the aperture.

Two GAFCHROMIC® film were irradiated one with 5 discharges and the other with 10 discharges. PFMA-3 working parameters are the same for both: voltage: 18 kV and nitrogen pressure: 0.45 mbar. The two irradiated samples are shown in figure 3.28: the darker one is the one irradiated with 10 discharges, the level of blackening indicates saturation.

The analysis in Matlab was performed on the second sample (5 discharges): the one less dark, less saturated. The GAFCHROMIC® film was scanned in reflection mode and converted to the 8-bit grey scale, with the same procedure described before for the other film. A line through the middle of the area was chosen and the isotropy of the x-ray beam produced was analyzed with the *polar plot* tool in Matlab and the result is shown in figure 3.29.

The analysis shows a good isotropy of the beam.
It possible to notice edge effects in figure 3.29, due to the geometry of the drift tube: after the brass foil, there is an aperture with a diameter of 3.5 cm and 1 mm thickness responsible of these effects.
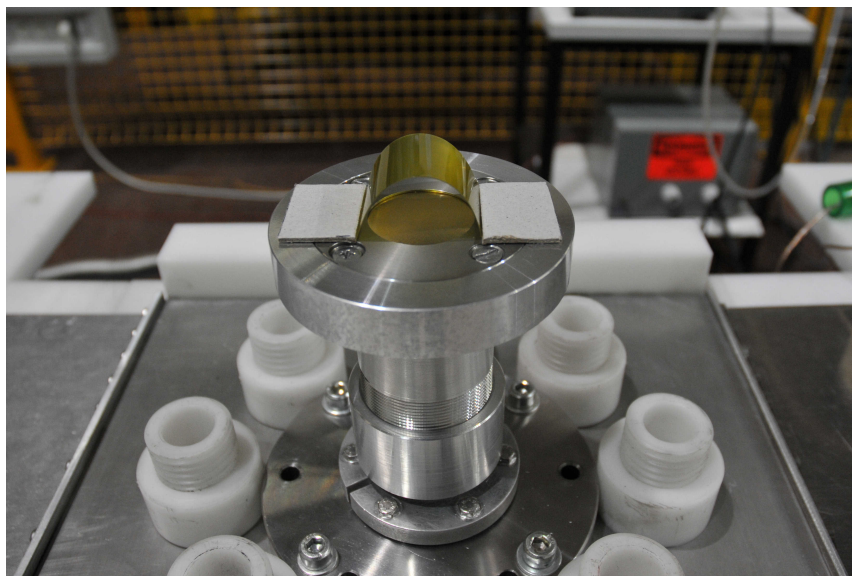
Figure 3.27   Experimental configuration of the isotropy measurements of the x-ray beam produced by the PFMA-3 device
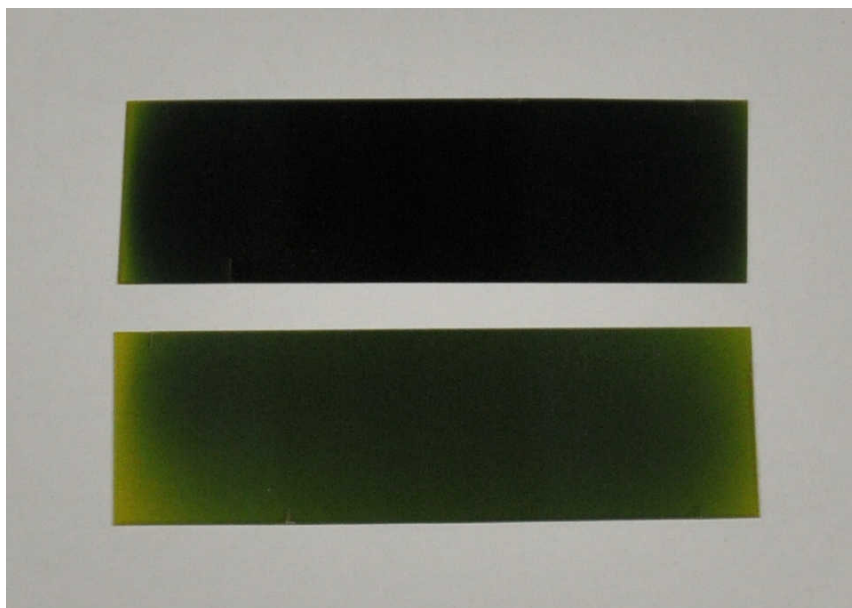
Figure 3.28   Irradiated samples for the isotropy measurements
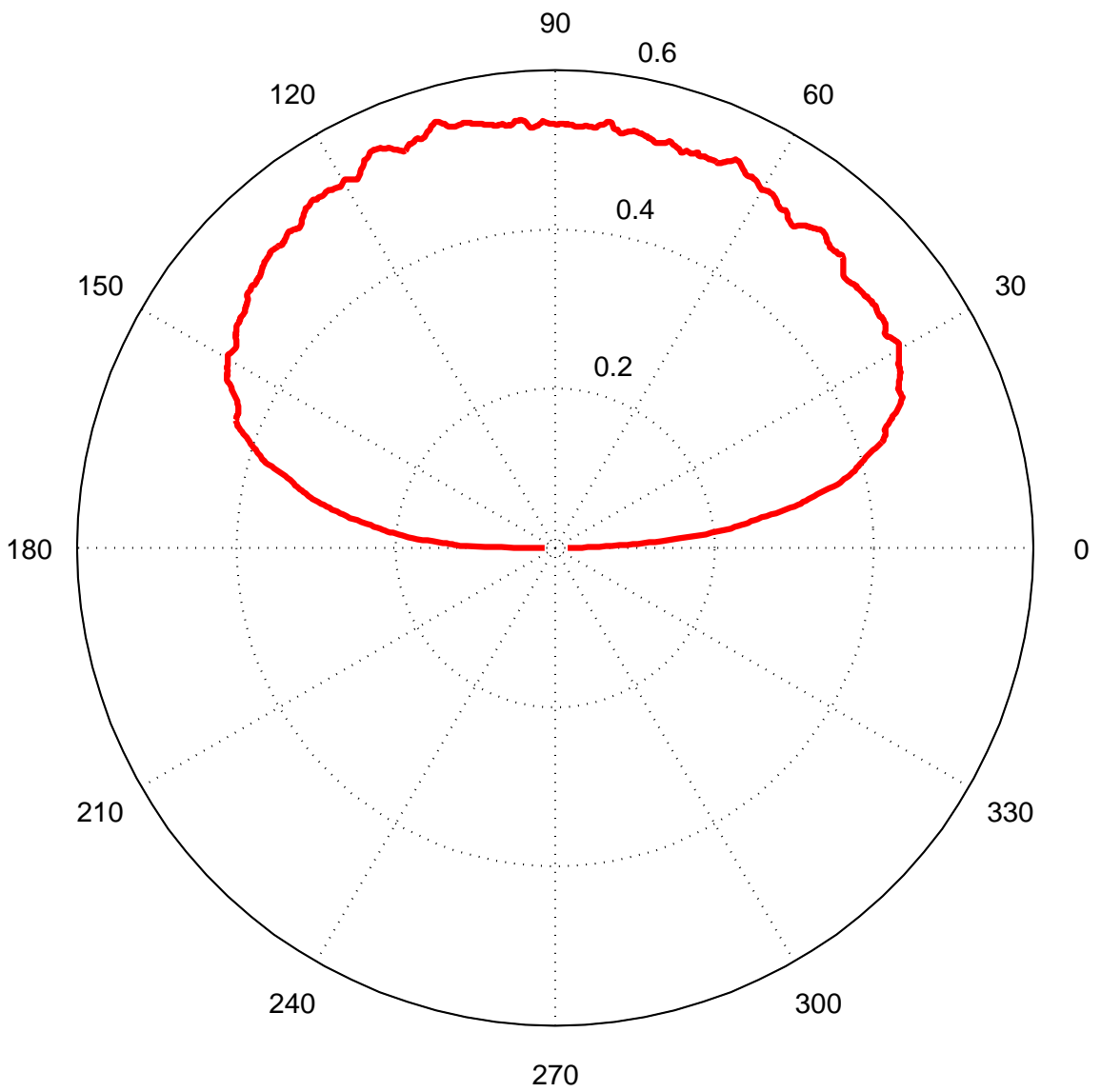
Figure 3.29 Isotropy analysis in Matlab

3.7 Radio-biological results of the cell culture irradiations

The cell culture irradiations were conducted to verify the efficiency of PFMA-3 on the cell culture irradiations on two different human cell systems: a glioblastoma multiforme cell line (T98G) derived from a human tumor and normal human dermal fibroblasts (hDF) derived from adult human skin, measuring the membrane ionic currents, cell growth and stress response [28].

This work is a collaboration with the radio-biological group useful to verify the RBE (relative biological effectiveness) of PFMA-3. The results are preliminary and further experiments have to be conducted.

The cells were irradiated with x-rays, with dose ranging between 0.5 and 4.5 Gy with intermediate points to obtain the kinetic response as a function of the dose, using PFMA-3. Membrane currents were measured in the whole-cell configuration of the patch clamp technique at room temperature. Current traces were acquired at digitizing rates of 20 kHz. Images were acquired every 30 minutes for about 90 hours in bright field to perform growth curves and in bright field and in fluorescence to perform the stress oxidative response analysis. Growth curves data were obtained, counting cells with a semi-automatic procedure, from three or four images acquired every four hours; the average was normalized with respect to the number of cells counted at time t = 0. Fluorescence data were obtained counting the number of fluorescent pixels in three fields for each sample, 24 and 48 hours after irradiation. The fluorescent pixels average was normalized to the number of fluorescent cells.

Cell growth: T98G and hDF were both irradiated by x-rays using the PFMA-3 (0.5 and 2 Gy). Growth curves of T98G cells (figure 3.30) showed a significant dose dependent decrease in the proliferation rate for both doses.

Stress response: the DHE fluorescence data (figure 3.31) suggest a trend in which superoxide intracellular concentration decreases at lower irradiation doses compared to control and higher doses.

(a)   (b)
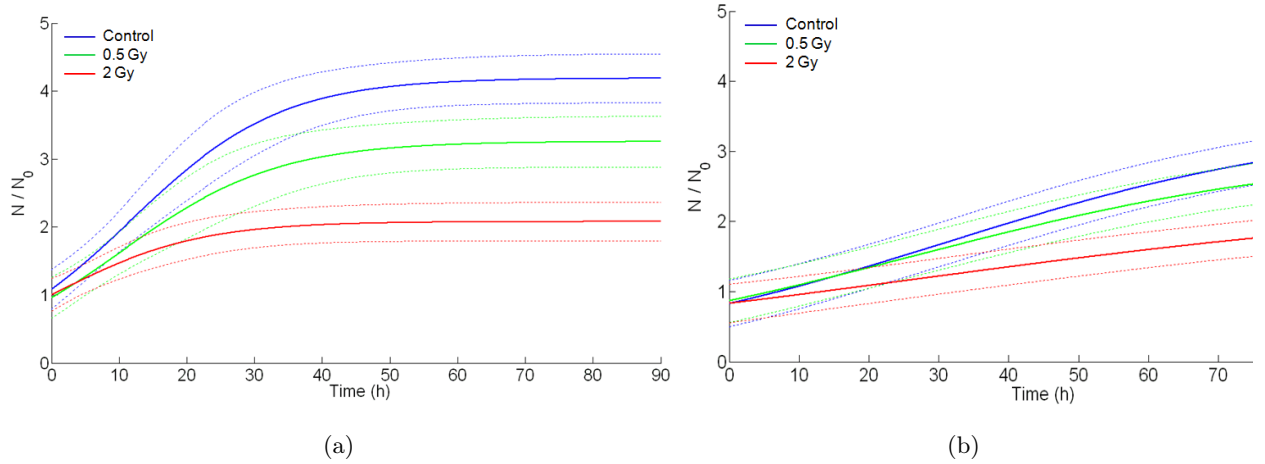
Figure 3.30 PF's x-rays effect on growth curves of T98G (a) and hDF (b) cells. Data were
normalized with the number of cells at time $t = 0$ and fitted with the logistic curve:
$N(t) = (s \cdot f)/[s + (f - s)exp(-g \cdot t)]$

(a)   (b)
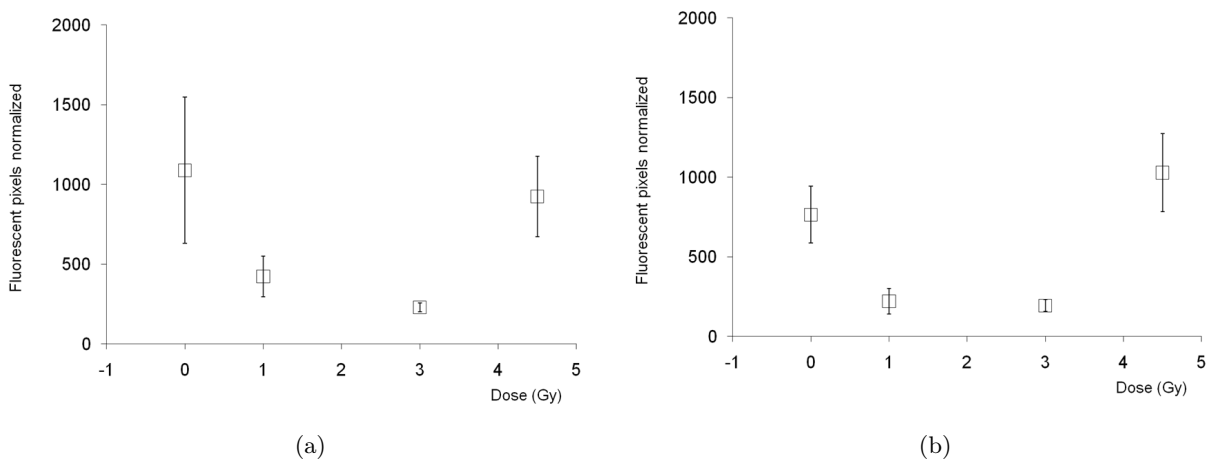
Figure 3.31 PF's x-rays effects on T98G superoxide intracellular production. Cells were marked
with DHE and observed in fluorescence microscopy at 24 (a) and 48 (b) hours after
irradiation. Data represent the mean number of fluorescent pixels normalized to
the number of fluorescent cells. Error bars represent the standard deviation.

Chapter 4

Monte Carlo Simulation of the Conversion X-Rays

For the applications described in the previous chapters, the spectrum of the x-rays thus produced must be investigated, to estimate the penetration in and the dose to Standard Human Tissue.

To this end version 2.60 of the MCNPX Monte Carlo code is used in this project [29]. MCNPX was used instead of MCNP5 because it has more accurate algorithms for electron interactions with the material and more accurate cross sections at low energies.

These simulations were conducted also because it is very difficult to measure directly the x-ray spectra.

The MCNPX simulation presented showed that the x-ray spectrum emitted comprises two components, one at lower energy (of the order of $10\,\mathrm{keV}$) capable of imparting dose only superficially, and one with higher energy (centered around $50\,\mathrm{keV}$), capable of reaching deeper in tissue [30].

4.1 Input of the Monte Carlo Code

In the following paragraphs the Monte Carlo input will be described. The code is presented below.

```
problem: electron and photon in gafchromic film
c geometry card
c stainless steel cylinder
1   1    -7.85          1  -2  3  -4          imp:p=1 imp:e=1
2   2    -0.0000006     1  -5  -3             imp:p=1 imp:e=1
c brass target subdivided in different layers  until 100 um
c to study different thicknesses, reality 50 um the first and
c second layer full of nitrogen
c first layer 25 um
```

```
3    2    -0.0000006    -3  5 -6                imp:p=1  imp:e=1
c second layer 50 um
4    2    -0.0000006    -3  6 -7                imp:p=1  imp:e=1
c in the brass target the divisions are more to study better the physics involved
c third layer 62.5 um
5    3    -8.5          -3  7 -8                imp:p=1  imp:e=1
c firth layer 75 um
6    3    -8.5          -3  8 -9                imp:p=1  imp:e=1
c fifth layer 87.5 um
7    3    -8.5          -3  9 -10               imp:p=1  imp:e=1
c sixth layer 100 um
8    3    -8.5          -3  10 -2               imp:p=1  imp:e=1
c stainless steel collimator
9    1    -7.85          11 -4  2 -12           imp:p=1  imp:e=1
10   4    -0.0012048    -11  2 -12             imp:p=1  imp:e=1
c stack of 5 gafchromic film
c each film is composed by one layer of 75 um polyethylene, 30 um of active layer
c and 175 um of polyethylene
c first film hd-810
11   8    -1.35         -13 14 -15 16  12 -17  imp:p=1  imp:e=1
12   5    -1.2          -13 14 -15 16  17 -18  imp:p=1  imp:e=1
13   6    -1.35         -13 14 -15 16  18 -19  imp:p=1  imp:e=1
c second film ebt2
21   6    -1.35         -13 14 -15 16  19 -20  imp:p=1  imp:e=1
22   7    -1.2          -13 14 -15 16  20 -21  imp:p=1  imp:e=1
23   5    -1.2          -13 14 -15 16  21 -22  imp:p=1  imp:e=1
24   6    -1.35         -13 14 -15 16  22 -23  imp:p=1  imp:e=1
c third film ebt2
31   6    -1.35         -13 14 -15 16  23 -24  imp:p=1  imp:e=1
32   7    -1.2          -13 14 -15 16  24 -25  imp:p=1  imp:e=1
33   5    -1.2          -13 14 -15 16  25 -26  imp:p=1  imp:e=1
34   6    -1.35         -13 14 -15 16  26 -27  imp:p=1  imp:e=1
c fourth film ebt2
41   6    -1.35         -13 14 -15 16  27 -28  imp:p=1  imp:e=1
42   7    -1.2          -13 14 -15 16  28 -29  imp:p=1  imp:e=1
43   5    -1.2          -13 14 -15 16  29 -30  imp:p=1  imp:e=1
44   6    -1.35         -13 14 -15 16  30 -31  imp:p=1  imp:e=1
c fifth film ebt2
51   6    -1.35         -13 14 -15 16  31 -32  imp:p=1  imp:e=1
52   7    -1.2          -13 14 -15 16  32 -33  imp:p=1  imp:e=1
53   5    -1.2          -13 14 -15 16  33 -34  imp:p=1  imp:e=1
```

```
54  6    -1.35        -13 14 -15 16  34 -35  imp:p=1  imp:e=1
c rest of the world
14  0       #1 #2 #3 #4 #5 #6 #7 #8 #9 #10 #11 #12 #13 #21 #22 #23 #24 #31 #32
            #33 #34 #41 #42 #43 #44 #51 #52 #53 #54        imp:p=0  imp:e=0


c Surfaces Card
c stainless steel cylinder
1   pz    0
2   pz    30
3   cz    1.76
4   cz    2.3
c brass target
c subdivided in different layers
5   pz     29.99
6   pz     29.9925
7   pz     29.995
8   pz     29.99625
9   pz     29.9975
10  pz     29.99875
c stainless steel collimator
11  cz    1.75
12  pz    30.1
c area of the gafchromic film
13  px    1.2
14  px    -1.2
15  py    1.2
16  py    -1.2
c thicknesses of the first gafchromic film (hd-810)
17  pz    30.100075
18  pz    30.100725
19  pz    30.110377
c thicknesses of the second gafchromic film (ebt2)
20  pz    30.115377
21  pz    30.118377
22  pz    30.121377
23  pz    30.138877
c thicknesses of the third gafchromic film (ebt2)
24  pz    30.143877
25  pz    30.146877
26  pz    30.149877
27  pz    30.167377
```

```
c thicknesses of the fourth gafchromic film (ebt2)
28  pz      30.172377
29  pz      30.175377
30  pz      30.178377
31  pz      30.195877
c thicknesses of the fifth gafchromic film (ebt2)
32  pz      30.200877
33  pz      30.203877
34  pz      30.206877
35  pz      30.224377


c Material Card
c stainless steel of the extraction tube nad collimator
m1      6000  0.0007   14000  0.01  25000  0.02  15000  0.00045
        16000  0.0003  24000  0.18  7000   0.0011  28000  0.095
        26000  0.69245
c nitrogen at low pressure
m2      7000   1.0
c brass target
m3      29000  0.64    30000  0.36
c air
m4     8016 0.21   7014  0.79
c active layer of the gafchromic film
m5      1000   0.097  3000   0.009  6000   0.587  7000   0.0023
        8000    0.28  17000  0.0175  19000  0.0064
c polyethylene of the gafchromic film (substrate)
m6      1000   0.042  6000   0.625  8000   0.333
c adhesive layer
m7      1000   0.094  6000   0.651  8000   0.255
c surface layer set immediately before the active layer
m8      1000   0.058  3000   0.063  6000   0.310  8000   0.250
        17000  0.320
c
MODE P E
c
c source definition: electron source
c
SDEF PAR=E POS=0 0 0.001 AXS=0 0 1 ERG=d1 VEC=0 0 1 DIR=d2
c
c elctron spectrum discribed like an histogram
si1  H  0. 0.01 0.02 0.03 0.04 0.05 0.06 0.07 0.08 0.09 0.1 0.11 0.12 0.13 0.14
```

```
        0.15 0.16 0.17 0.18 0.19 0.2 0.21 0.22 0.23 0.24 0.25 0.26 0.27 0.28
        0.29 0.3
sp1  D  0. 0.06 0.0924 0.11048 0.10604 0.09783 0.09942 0.10817 0.08827 0.06947
        0.05406 0.03544 0.02628 0.01482 0.01205 0.00784 0.00476 0.00353 0.00172
        0.00159 0.00127 0.00026 0.00014 0.00011 0.00011 0.00009 0.00013 0.00013
        0.00011 0.00005 0.00002
c
c
BBREM 1. 1. 46I 10.  3
c
c director cosine for the sourec with a collimated aperture of 3.3 degrees
si2 A  0.998  1
sp2  1  1
c
c photon fluence in the different thicknesses of the brass target
F14:P 5 6 7 8  T
c electron fluence in the different thicknesses of the brass target
F24:E 5 6 7 8  T
c
c electron spectrum in the brass target and in the gafchrmic film
F114:E 5 6 7 8 10 12 23 33 43 53
E114:E 0. 0.01 0.02 0.03 0.04 0.05 0.06 0.07 0.08 0.09 0.10 0.12 0.14 0.16 0.18
      0.2 0.25 0.3
c
c photon spectrum in the brass target and in the gafchrmic film
F124:P 5 6 7 8 10 12 23 33 43 53
E124:E 0. 0.01 0.02 0.03 0.04 0.05 0.06 0.07 0.08 0.09 0.10 0.12 0.14 0.16 0.18
      0.2 0.25 0.3
c
c electron(3) and photon(4) fluence in the active layer of the gafchromic film
F34:E 12 23 33 43 53
F314:E 11 12 13
F324*:E 12 23 33 43 53
c
F44:P 12 23 33 43 53
F414:P 11 12 13
F424*:P 12 23 33 43 53
c
c dose deposited in the active layer of the gafchromic film
c dose produced by photons
F16:P  12 23 33 43 53
```

```
c dose produced by electrons
F26:E  12 23 33 43 53
c
c dose deposited in the brass target
c dose produced by photons
F116:P  5  6  7  8  T
c
c dose produced by electrons
F126:E  5  6  7  8  T
c
c current on the surface of the brass target
F1:E     7
C1     0  1
c
c number of particles
nps  1E+08
c
PTRAC file=asc write=all max=50000
c
print
```

4.1.1   Geometry

The input geometry focuses on the end part of the device and, more specifically, the end part of the extraction tube with the collimating aperture and the brass foil where the electron beam is driven to impinge, thus generating the conversion x-rays, and the five gafchromic film sheets positioned immediately after the collimated aperture. The extraction tube is a hollow cylinder of conducting material connected to the inner electrode of PFMA-3; the inner volume of the tube contains nitrogen at 0.5 mbar at room temperature,

$$0.5 mbar = 50.7 Pa \tag{4.1}$$

$$kT = 4.1 \cdot 10^{-21} \tag{4.2}$$

$$n = \frac{p}{kT} = 1.2 \cdot 10^{22} \frac{\#}{m^3} \tag{4.3}$$

$$6.02 \cdot 10^{23} \rightarrow 28g \tag{4.4}$$

$$\alpha = 1 \rightarrow \frac{28}{6.02} \cdot 10^{-23} = 4.7 \cdot 10^{-23} g \tag{4.5}$$
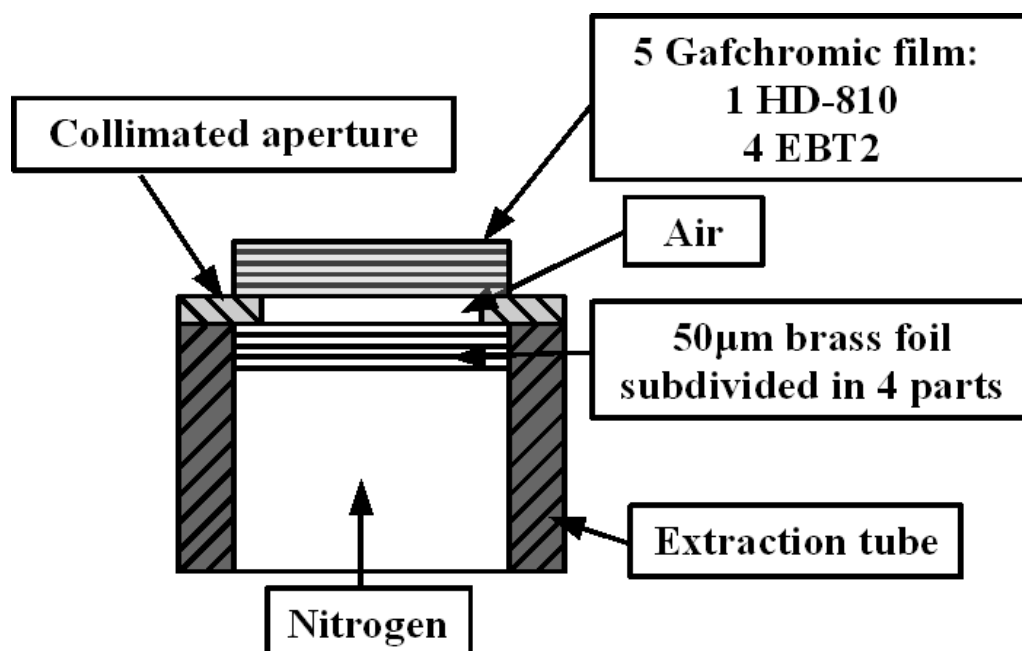
Figure 4.1 Details of the Monte Carlo input geometry

$$\rho = n \cdot \alpha = 5.6 \cdot 10^{-1} \frac{g}{m^3} \cong 0.6 \frac{g}{m^3} = 0.6 \cdot 10^{-6} \frac{g}{cm^3} \tag{4.6}$$

corresponding to a mass density of $0.6 \times 10^{-3}\,\mathrm{kg/m^3}$. The total drifting path of the electron beam is $30\,\mathrm{cm}$.

Details of the geometry are presented in Fig. 4.1, as generated by VISED [31]: the end part of the extraction tube is filled with nitrogen. A $50\,\mu\mathrm{m}$ brass foil is positioned immediately before the aperture, subdivided into 4 layers for greater detail in the description of the electron and photon interactions. Past the target, within the open space of the aperture, there is air at standard atmospheric pressure and temperature, and right out of the aperture the stack of five sheets of GAFCHROMIC® film (1 HD-810 + 4 EBT2).

Further details of the geometry are shown in figure 4.2, generated by the Sabrina code.

4.1.2 Source

The electron spectrum shown in Fig. 4.3 has been measured with a magnetic spectrometer [16]. The electron mean energy is approximately $50\,\mathrm{keV}$. Tails of the electron distribution are present up to about $200\,\mathrm{keV}$.

In the simulation, the electrons start as a point source directed to the collimator aperture, producing a conical beam. The starting electron spectrum in MCNPX must be described in discretized form, subdividing the energy range into discrete "bin", each "bin" being associated with a discrete probability (Fig. 4.4).

To describe the beam, the "direction cosines" MCNPX feature has been used. The aperture of the cone is 3.3°, resulting from the collimated target radius of $17.5\,\mathrm{mm}$ and the
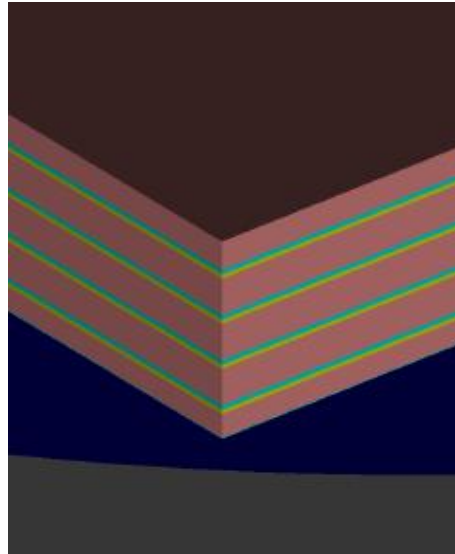
Figure 4.2   Details of the Monte Carlo input geometry extrapolated with the Sabrina Monte Carlo code

Table 4.1   Mass fraction composition of GAFCHROMIC® film

	Density [$\mathrm{g\,cm^{-3}}$]	H	C	O	Li	Cl
Polyester	1.35	0.042	0.628	0.335		
Active layer	1.20	0.097	0.591	0.285	0.009	0.018
Adhesive Layer	1.20	0.094	0.651	0.255		
Surface Layer	1.20	0.058	0.310	0.250	0.063	0.320

distance between the source and the brass foil of 30 cm. Electron current measurements with a Rogowski coil revealed peak current values in the range 100–400 A with a pulse duration (FWHM) of 0.1–0.5 µs. Integration of the electron current signal yields an average charge value of $\sim 0.2\,\mathrm{mC}$ per discharge, corresponding to 1.2×10^{15} electrons per discharge. MCNPX simulations are per unit starting particle, in view of to the linear behavior of the system with respect to the source; multiplication of the results by the number of starting particle of the starting particles yields the quantities consistent with the problem investigated. To describe the EBT2 GAFCHROMIC® film, the composition of Fig. 4.5 is used.

As it can be seen, the composition is asymmetric on the two sides of the active layer. For the HD-810 GAFCHROMIC® film, that it is the first film of the stack, the composition is the one of Fig. 4.6.

Specifics on the atomic composition of the layers, detailed in the *materials* section of the input to MCNPX, are presented in table 4.1: these information were described in chapter 2.

In the attenuation measurements, both HD-810 and EBT2 films are consistently posi-
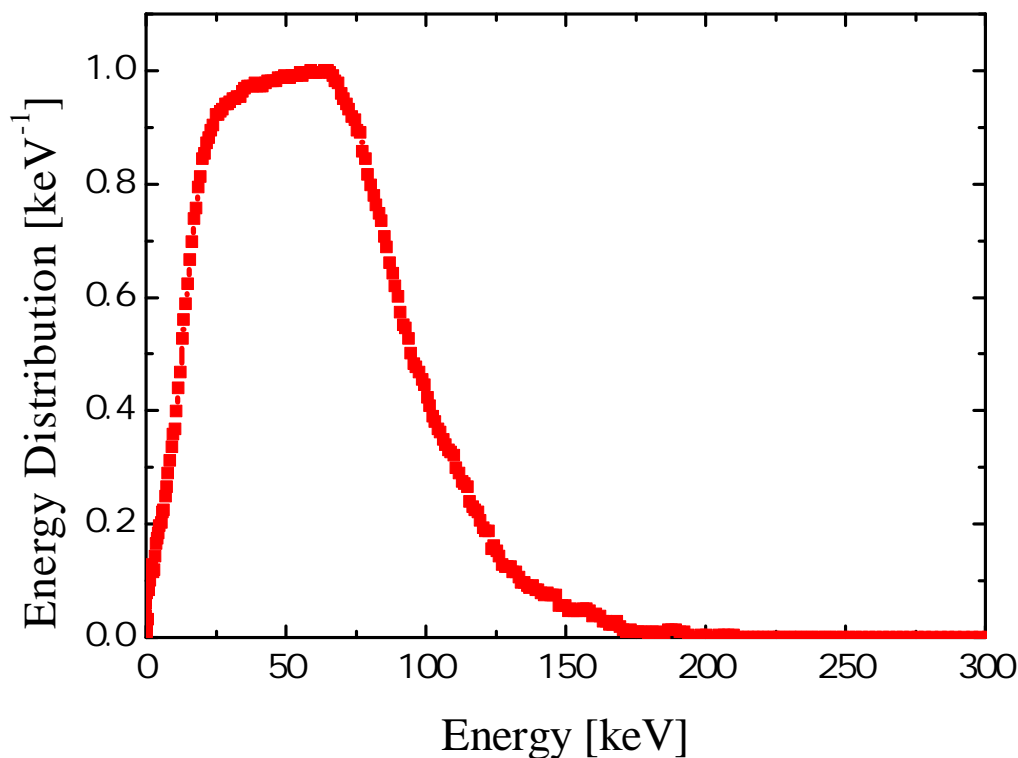
Figure 4.3   Electron spectrum measured by a magnetic spectrometer

tioned with the thinner coating (0.75 µm and 80 µm) facing toward the incoming beam: in the Monte Carlo input they are described consistently with this practice.

4.1.3   Output quantities requested

The output quantities requested from the simulation are electron and photon fluence in the different parts of the geometry, the spectrum of the photon produced by the electrons impinging on the target and in the five film sheets, the electron spectrum in the brass foil, in air and in the five sheets of film, and the dose deposited by electron and photons in the five film sheets. In the present simulation, a variance reduction technique (BBREM Card) had to be used. Bremsstrahlung processes generate many low-energy photons, whereas higher-energy photons are rarer: however the latter are of greater interest in the present application. In view of obtaining a finer description of the higher energy part of the spectrum, a standard variance reduction technique (BBREM Card) [29] was used in the present simulation, although only for the brass foil section.

The number of particles used in the present simulation is 10^8. The simulation takes 10–11 hours on a standard desktop computer, and the relative error in the output variables was never found to be higher than 2%, which is adequate accuracy for the present assessment needs.
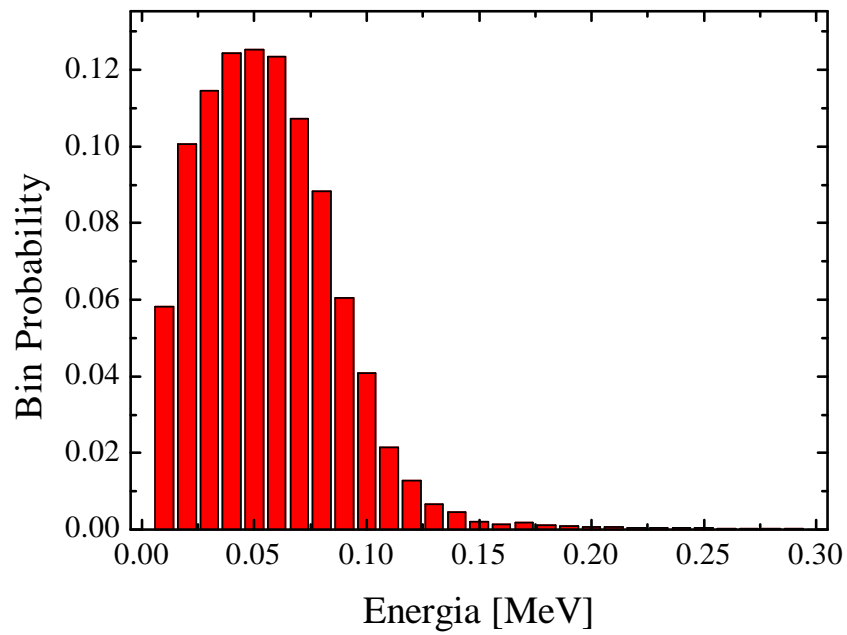
Figure 4.4   Details of the Monte Carlo source input (described as an histogram)
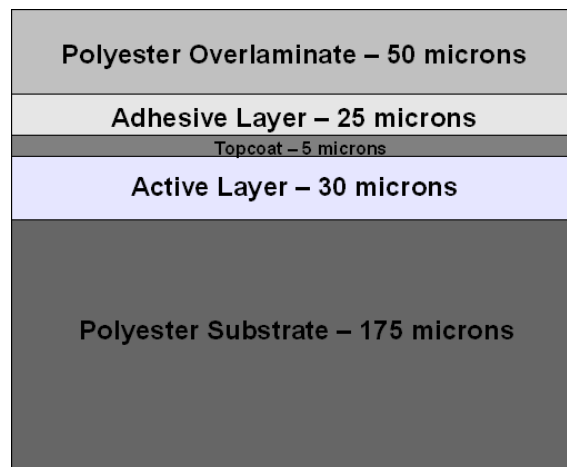
Figure 4.5   GAFCHROMIC® film: EBT2
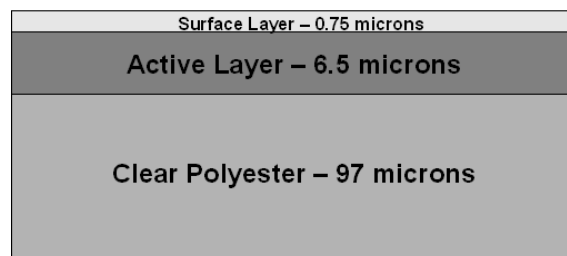
Figure 4.6   GAFCHROMIC® film: HD-810

4.2 Results of the simulation

In the following paragraphs the Monte Carlo output will be described. Wherever it applies, the results presented in the following are obtained taking into account secondary electron production.

4.2.1 Fluence

In figure 4.7, the attenuation of the fluence-per-discharge of photons and electrons can be seen at a number of steps across the 50 μm brass thickness.

In figure 4.8 the photons and electrons attenuation of the fluence-per-discharge in the active layers of the GAFCHROMIC® film.

4.2.2 Photon spectrum produced by the impinging of the electron beam on the brass foil

Fig. 4.9 presents the photon spectrum in the brass foil and Fig. 4.10 the photon spectrum exiting the brass foil and in the active layer of each film sheets. These results are important to understand the energy of the x-rays produced and the penetration in standard human tissue (EBT2 are human tissue equivalent).

In Figure 4.10 a double components is present: one at lower energy around 10 keV and one at higher energies, around 50 keV. The component at lower energy is attenuated much more rapidly than the component at higher energy, as expected. To investigate these two components, a number of simulations were run using the "PHYS" option card, an MCNPX tool permitting selection of different processes of present interest. The command line of this option card interesting for this study concerns the electron physics and has the following form:

```
PHYS:E emax ides iphot ibad istrg bnum xnum rnok enum numb
```

The first number (*emax*) indicates the maximum energy of the electrons considered in the simulation, the default is 100 MeV, the second number (*ides*) the electron production by photons, the third one (*iphot*) the photon production by electrons, the fourth one (*ibad*) the angular distribution of bremsstrahlung emission, the fifth one (*istrg*) the calculation method for the straggling, the sixth one (*bnum*) the bremsstrahlung x-ray production, the seventh one (*xnum*) turns off and on the characteristic x-ray production, the eighth one (*rnok*) turns off and on the knock-on electron production, the ninth one (*enum*) turns off and on the pair production and finally the tenth one (*numb*) controls the bremsstrahlung nominal production.
The default line is the following:

```
PHYS:E 100 0 0 0 0 1 1 1 1 0
```
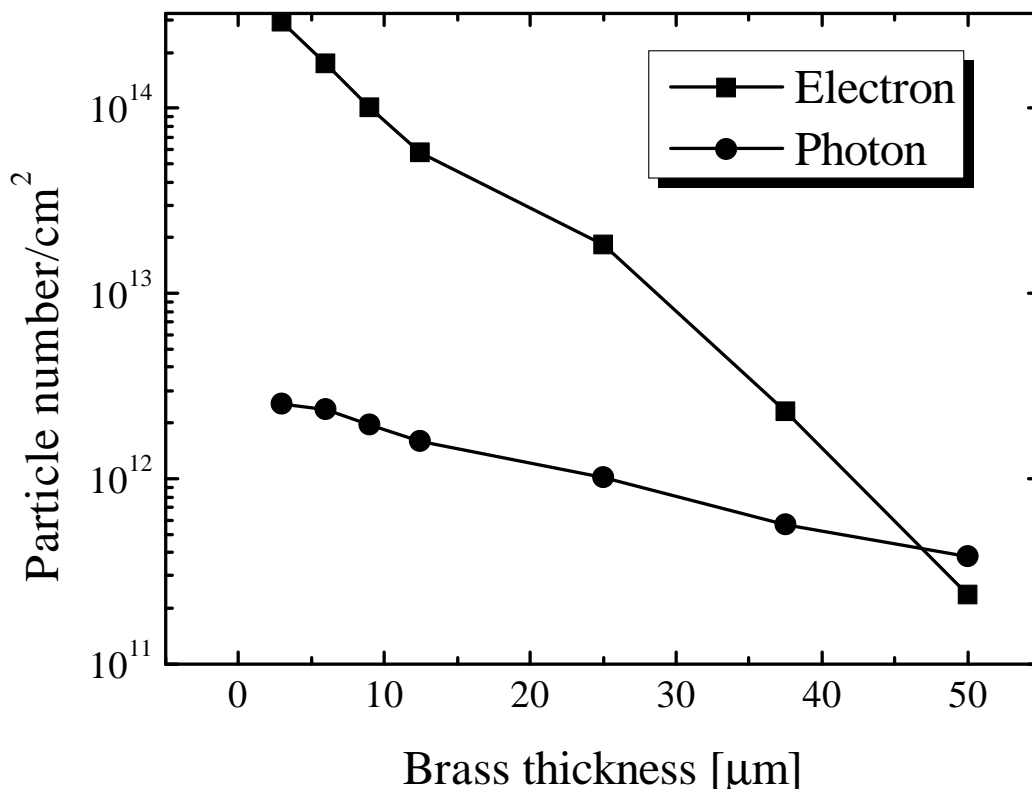
Figure 4.7   Fluence-per-discharge in brass thickness

Changing the number 1 to 0 and the number 0 to 1, it is possible to select the different processes.

The first interest is characteristic x-ray and bremsstrahlung x-ray production. Turning off the production of characteristic x-rays, the component at high energy alone can be seen to survive, Fig. 4.11.

Conversely, by turning off bremsstrahlungemission, the characteristic x-rays are seen to generate the low energy part of the spectrum (Fig. 4.12).

The 10 keV range is consistent with spectroscopic data (see NIST database [23]): K-edge transition x-rays have energies of nearly 9 keV and 9.7 keV, respectively, for copper and zinc, the two components of brass. A comparable x-ray spectrum is obtained from a simulation (made with the EGS code) of a different Plasma Focus device, but in a similar context [8].

4.2.3   Electron spectrum in the brass foil and out of the target

Figure 4.13 shows the electron spectrum in the brass foil each 12.5 μm.

Figure 4.14 represents the electron spectrum exiting the target and in the 1st (HD-810 used like a filter) and 2nd (EBT2) film.

In these film sheets the electrons detected are the ones that had enough energy to pass
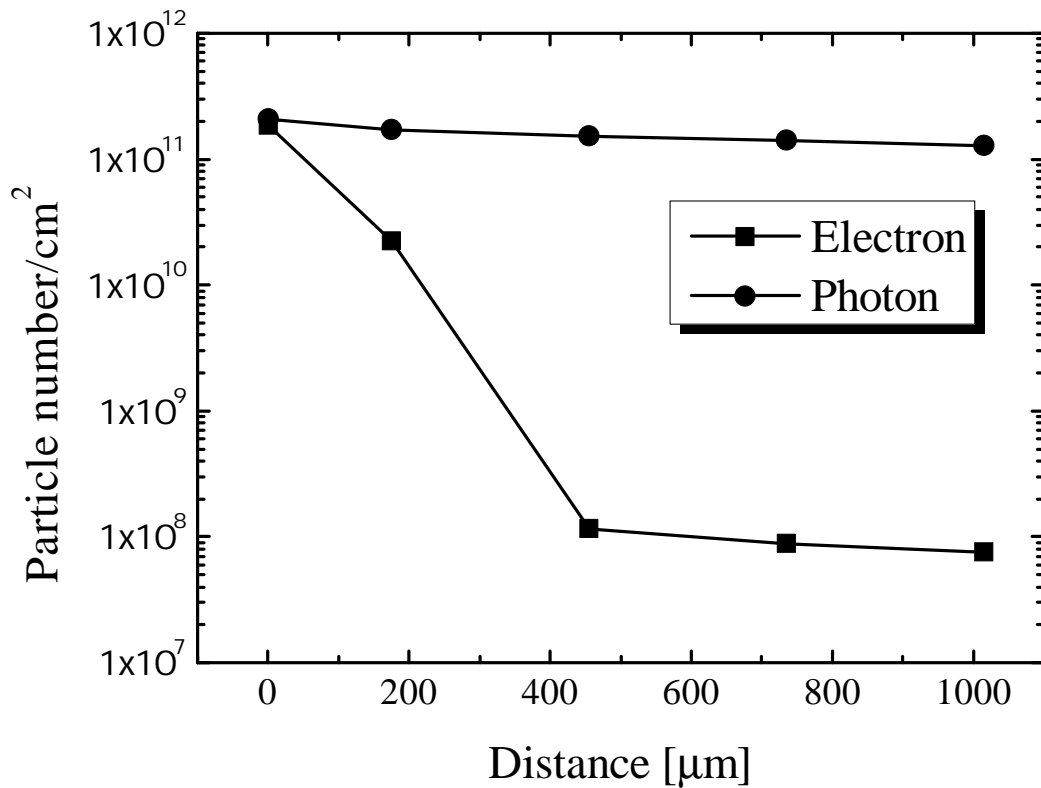
Figure 4.8 Fluence-per-discharge in GAFCHROMIC® film

the 50 µm brass foil (see the electron range) and reach the second film sheet. Figure 4.15 shows the electron spectrum in the 3rd to 5th film sheets.

The mean energy is around 10 keV. The electrons in the spectra of Figure 4.15 are the secondary electrons produced by photon interaction, the electron beam from the device does not reach so far into the film stack. This can be confirmed using the "PHYS" option card to turn off the secondary electron production processes: the spectra of figure 4.15 simply disappear.
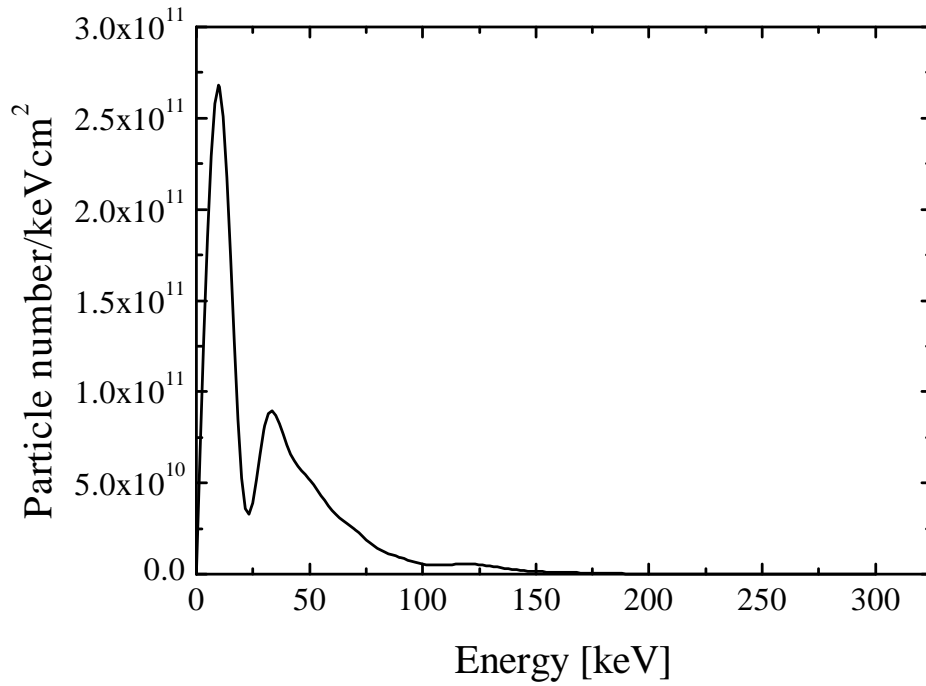
Figure 4.9   Photon spectrum in the brass foil
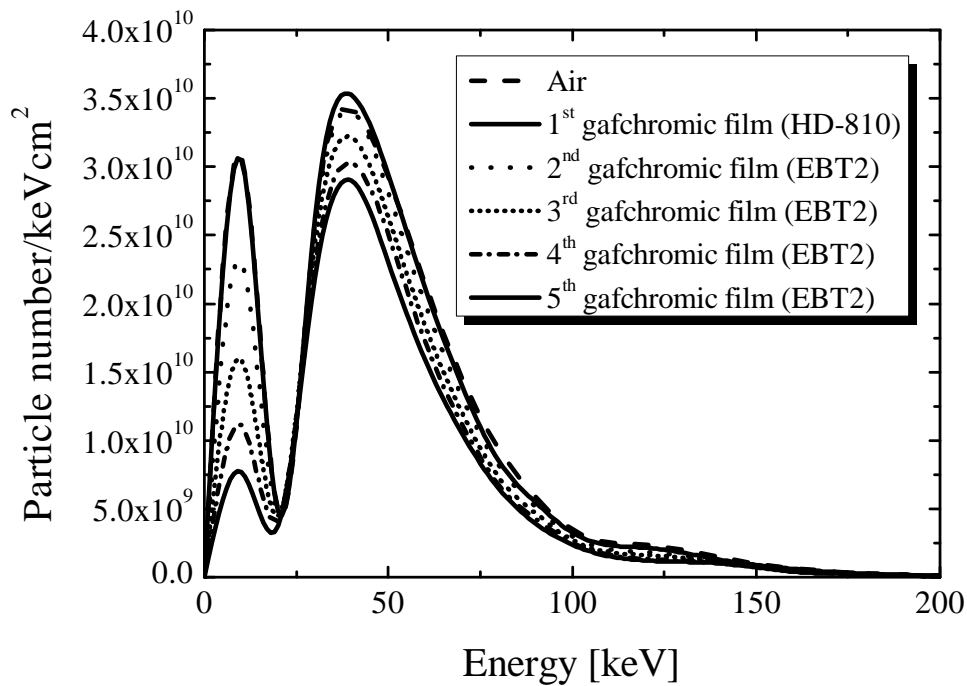
Figure 4.10   Photon spectrum exiting the brass foil (in air at standard atmospheric pressure) and in the active layer of the five GAFCHROMIC® film
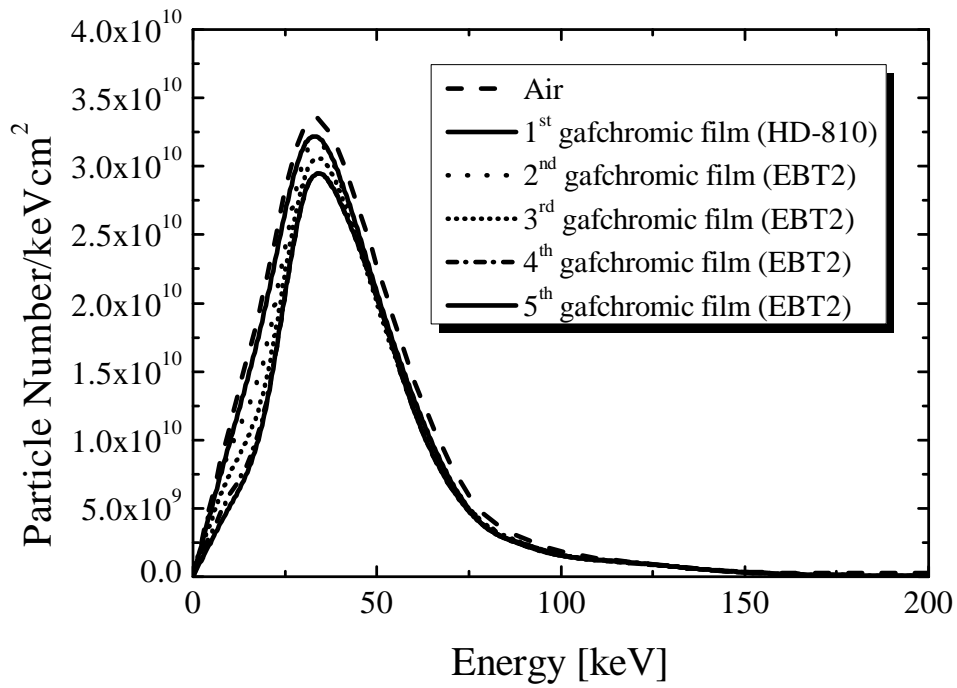
Figure 4.11 Photon produce by bremsstrahlungeffect
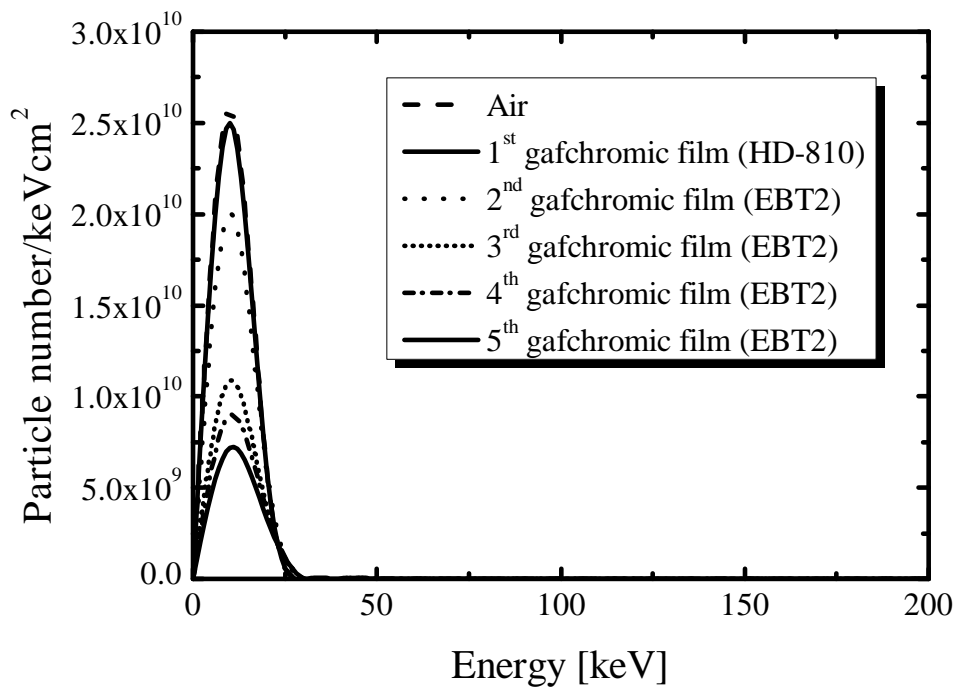
Figure 4.12 Photon produce by x-rays characteristic effect
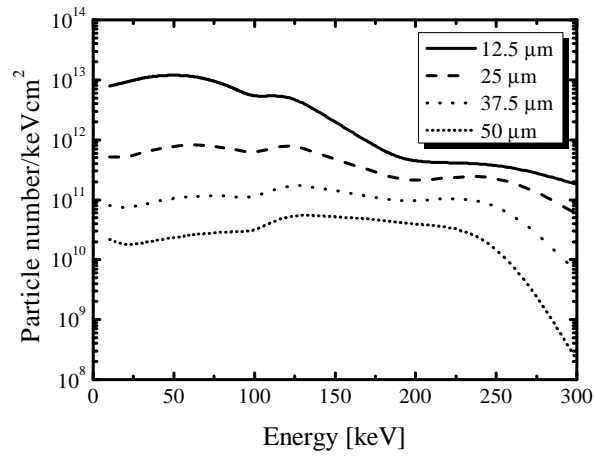
Figure 4.13 Electron spectrum in the brass foil each 12.5 μm
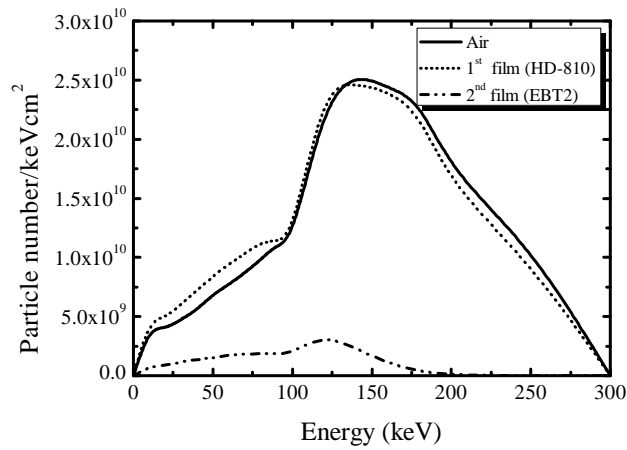
Figure 4.14 Electron spectrum exiting the target and in the first and second GAFCHROMIC®
film
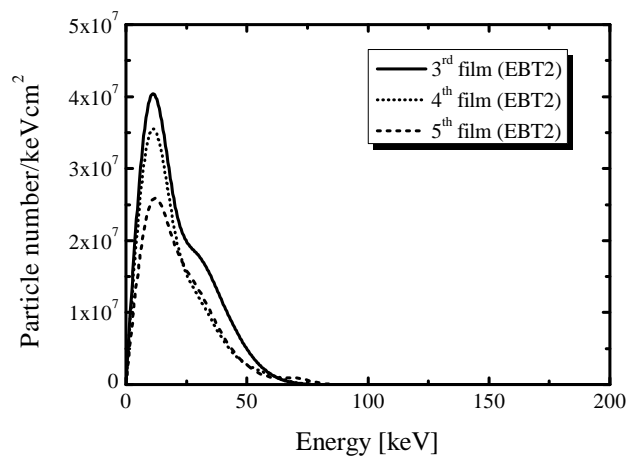
Figure 4.15 Electron spectrum from 3rd to 5th GAFCHROMIC® film

4.3 Dose deposited in the Gafchromic film

To calculate the dose with the MCNPX code the "F6" tally is used, calculating the energy deposited per unit mass and per particle. The simulation calculates the doses from electrons and from photons produced by the electrons, in each active layers of the film sheets. MCNPX, in the simulation, takes into account also the production of secondary electrons and photons.

Since the "F6" tally is expressed in $[\mathrm{MeV\,g^{-1}}]$, to convert it into dose units, the following conversion had to be made (4.7):

$$F6 \left[\frac{MeV}{g}\right] \cdot 1.602 \cdot 10^{-13} \left[\frac{J}{MeV}\right] \cdot \frac{1}{0.001} \left[\frac{g}{Kg}\right] \cdot 1.25 \cdot 10^{15} [number of particles] \quad (4.7)$$

After the above calculation (4.7) this quantity becomes expressed in $\mathrm{J\,kg^{-1}}$, i.e., gray more precisely gray per discharge.

These simulations were compared with the experimental results obtained from attenuation measurements performed with GAFCHROMIC® film, as described in chapter 3. Figure 4.16 presents a comparison between simulated and experimental data.

Figure 4.17 is a detail of the figure 4.16, to see in greater detail the dose deposited in the last film sheet.

The comparison between the experimental data obtained from attenuation measurements and the simulated data calculating the dose deposited in the film shows a very good agreement.

Using the "PHYS" option card it is possible to turn off the secondary electron production in the dose evaluations and then the dose graph changes, as shown in figure 4.18, and in more a detailed scale in figure 4.19.

The results indicate that the secondary electron production play an important role in dose deposition.

The very good agreement of numerical and experimental data strengthens confidence that the results of the simulations yield a reliable picture of the physics involved.

The first question to be investigated was the depth of penetration of the x-rays produced by the device, to assess its capability to deliver dose: particular interest was focused on whether dose would only be superficial or rather reach deeper in tissue. The results show that the lower energy component disappears soon, reaching no farther than 0.4 mm, whereas the higher energy component, centered around 50 keV, reaches significantly deeper. Simulations, as well as the previous experimental campaign, were run with 1 mm of material, and at that depth the dose is still significant (0.5 Gy/discharge), hinting at the possibility of reaching definitely further. Future work may investigate thicker materials to assess the maximum depth of dose penetration.

Also, the simulations provide good guidance in the development of the target, insofar as the choice of material and geometry is concerned. Future choices being considered are higher Z materials Monte Carlo simulation of the dose deposited by the electron beam of
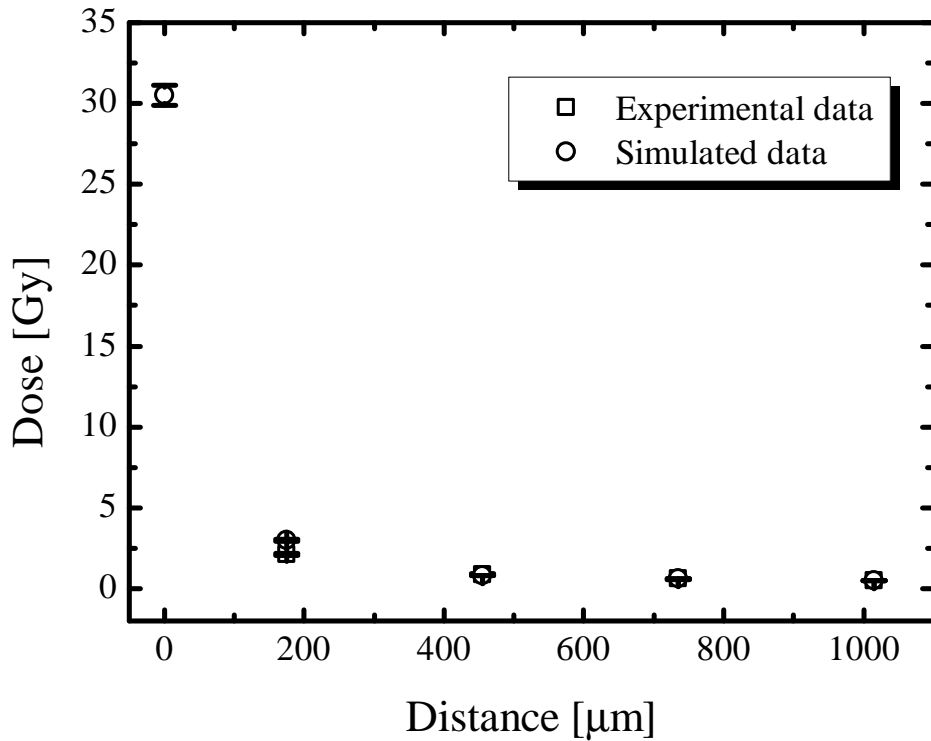
Figure 4.16   Dose comparison between simulated and experimental data

Table 4.2   Dose deposited difference between a 75 μm brass target and 50 μm brass target

	3rd Dose [Gy per discharge]	4th Dose [Gy per discharge]	5th Dose [Gy per discharge]
50 μm	0.83	0.6	0.49
75 μm	0.53	0.42	0.38
% of decreasing dose	36.0	30.0	22.0

PFMA-3 such as, e.g., tungsten, and/or combinations of different thicknesses. The influence of the spectral details of the incoming electrons can be evaluated, and hence the effect of operation conditions in turns, because of the effect they have on the electron spectrum. Again, this will provide guidance in the development of the IORT device.

An example was also the simulation of 75 μm of thickness of the brass target, figure 4.20. 75 μm was chosen because there were problems with the brass target breaking and the next standard size to 50 μm was selected.

The decrease of dose deposited can be summarized in table 4.2. In table 4.2 only the values in the 3rd film to 5th film sheets are reported, the ones of greater interest.

From this graph and from the values in the table, it is possible to understand that the dose deposited decreased and the 75 μm brass target attenuated too much the x-ray production in the brass foil.
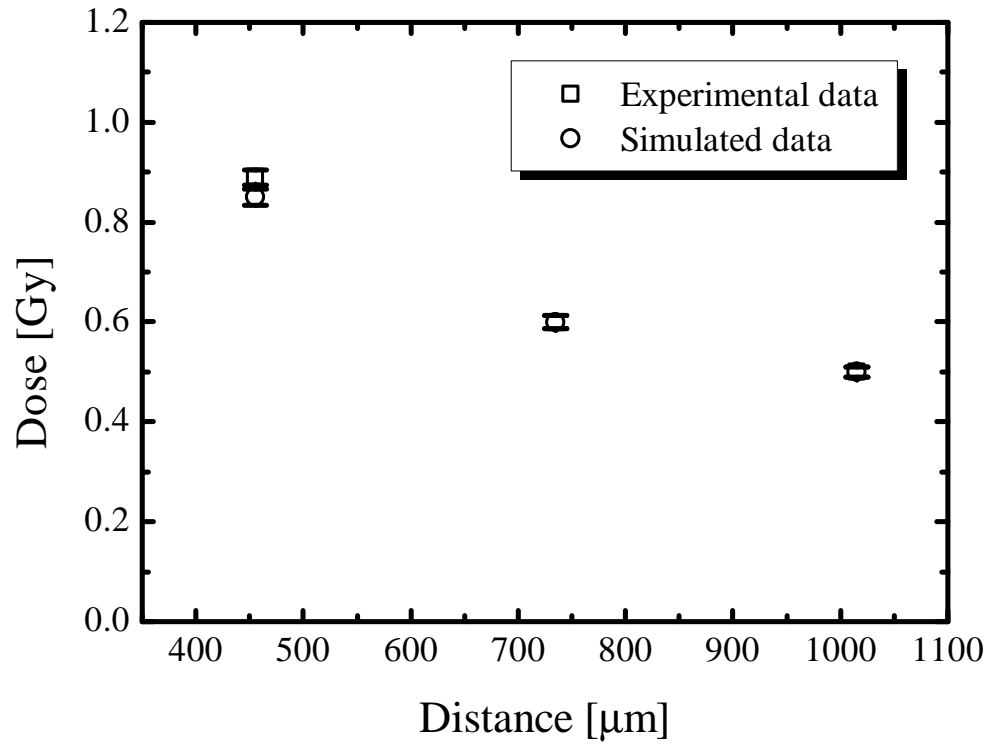
Figure 4.17   Detail of the dose comparison from 3rd film to 5th GAFCHROMIC® film
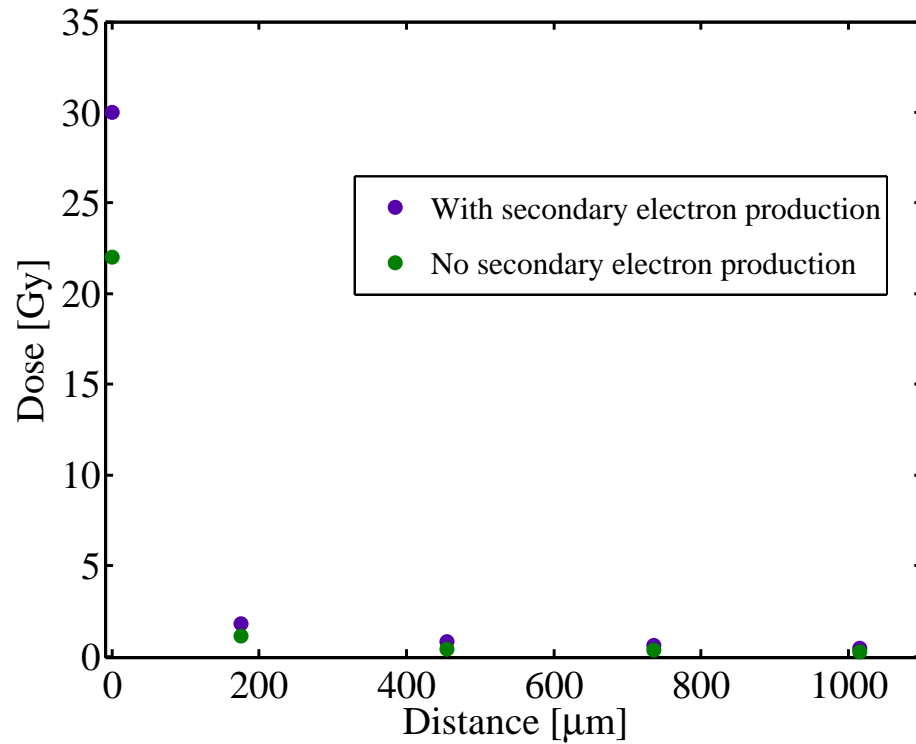
Figure 4.18   Dose comparison between secondary electron production and no secondary electron production
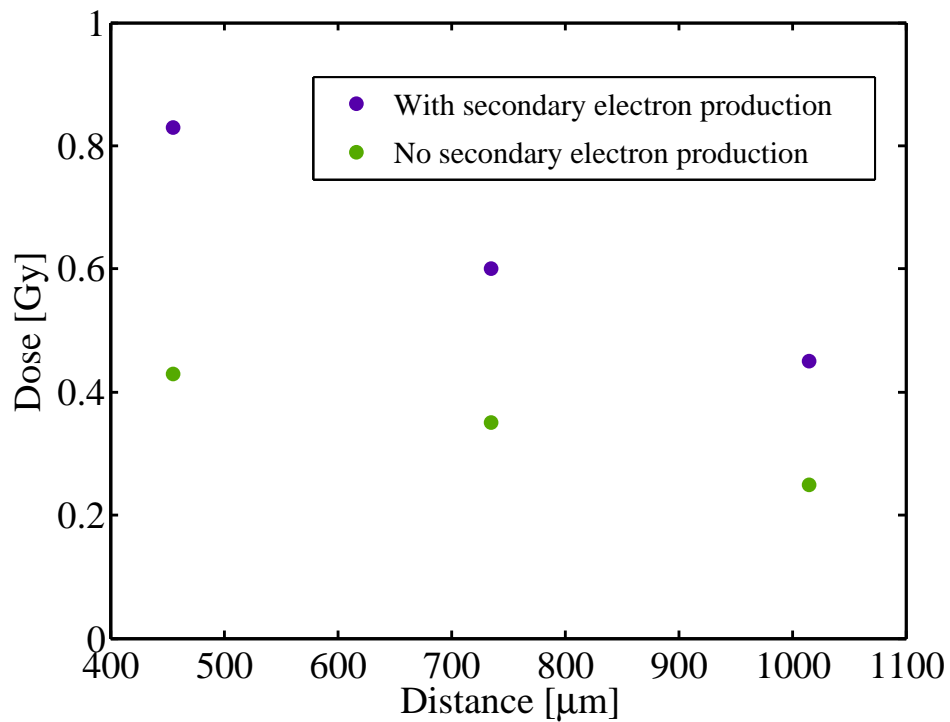
Figure 4.19   Detail of dose comparison between secondary electron production and no secondary electron production
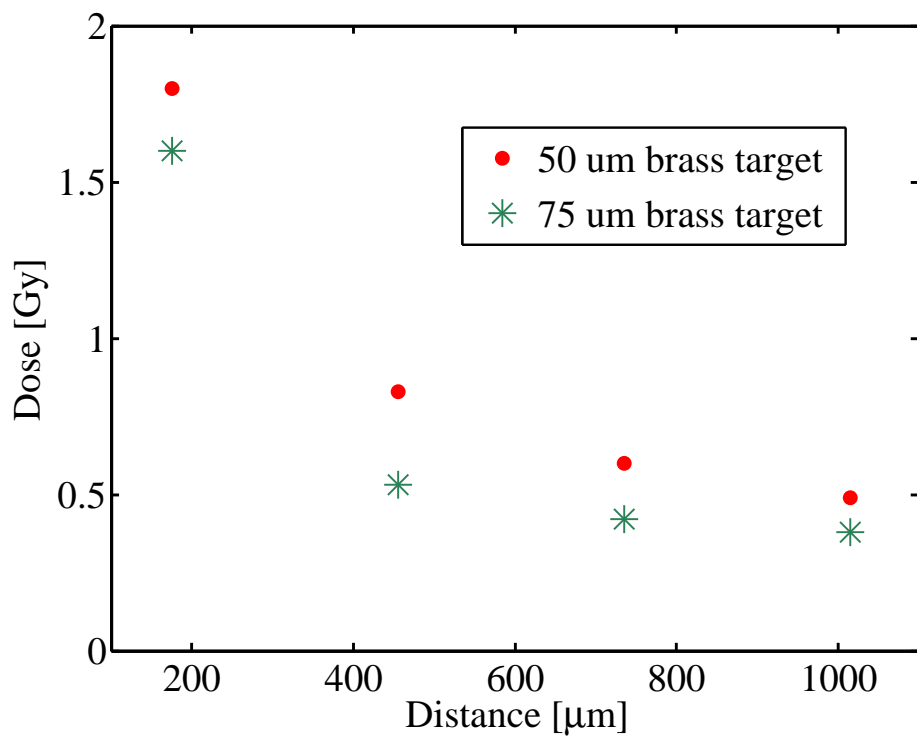
Figure 4.20   Dose deposited comparison between a 75 µm brass target and 50 µm brass target

Chapter 5

Brass converter

It was observed that a fracture of ∼5 mm will appear in the central part of the 50 µm brass foil after 50-60 discharges in normal working condition: 18 kV and 0.45 mbar pressure of nitrogen. Figure 5.1 shows the effect.

Figure 5.1   Break of the brass foil after 50-60 discharges of the Plasma Focus device

5.1   Sem Eds analysis

SEM EDS analysis was performed on the brass foil to characterize the three visible areas:

- brass area: external part
- dark area: intermediate part
- white area: central part

A SEM (Scanning Electron Microscope) can be utilized for high magnification imaging of almost all material With SEM in combination with EDS (Energy-dispersive x-ray spectroscopy) is it also possible to find out which elements different parts of a sample contain. The Energy-dispersive x-ray spectroscopy (EDS) is an analytical technique used for the elemental analysis or chemical characterization of a sample. It relies on the investigation of an interaction of a source of x-ray excitation and a sample.
To stimulate the emission of characteristic x-rays from a specimen, a high-energy beam of charged particles such as electrons or protons, or a beam of x-rays, is focused onto the sample being studied. The number and energy of the x-rays emitted from a specimen can be measured by an energy-dispersive spectrometer. As the energy of the x-rays are characteristic of the atomic structure of the element from which they were emitted, this allows the elemental composition of the specimen to be measured.
Figure 5.2, 5.3 and 5.4 show SEM images, respectively of the brass area, of the dark area and of the central white area.

The differences are more morphological than compositional in the three different areas. Micro-analysis were performed on discrete area for these specific zones. The mean semi-quantitative compositions determined are reported in table 5.1; the corresponding spectra are shown in figure 5.5, 5.6 and 5.7.
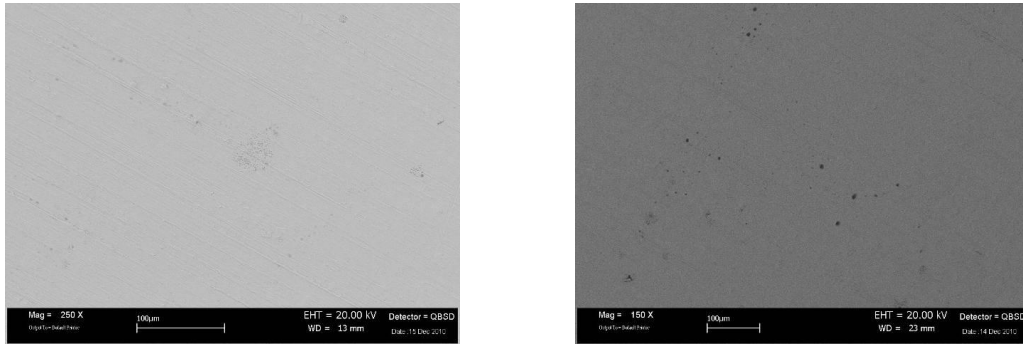
Figure 5.2 SEM images of two point of the brass external area
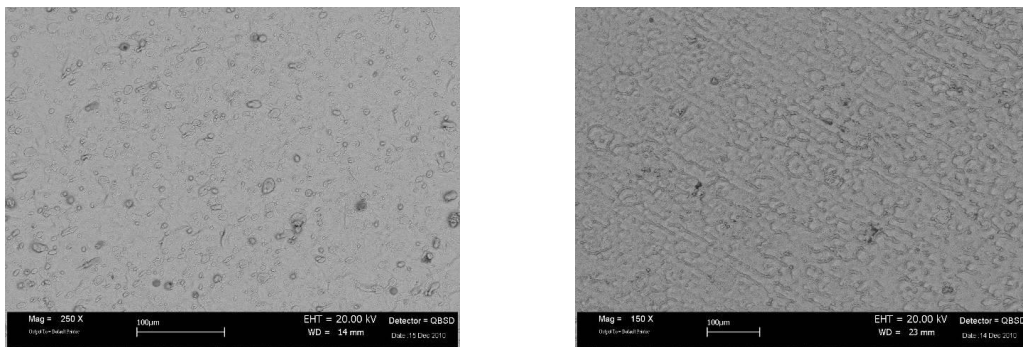
Figure 5.3 SEM images of two point of the darker intermediate area
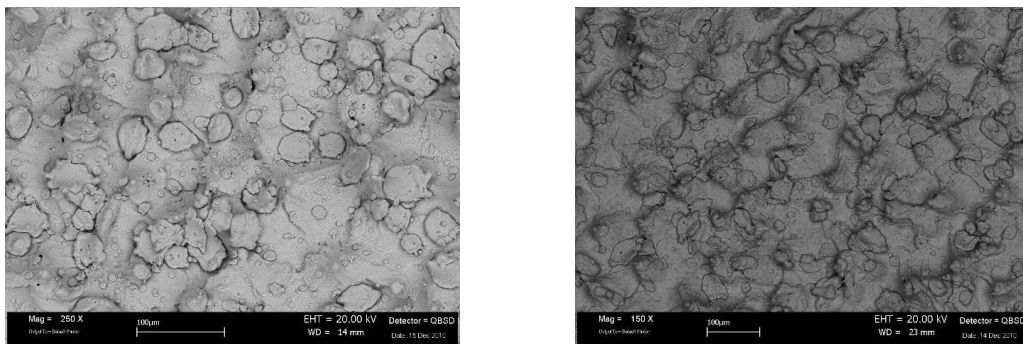
Figure 5.4 SEM images of two points of the central white area

Table 5.1 Mean weight semi-quantitative compositions determined in two different areas for each zone

Weight %	Brass Area		Dark Area		White Area	
	Area 1	Area 2	Area 1	Area 2	Area1	Area 2
O	1.6	2.0	6.4	5.0	1.2	1.2
Al	0.6	5.4	-	0.4	-	-
Cu	61.3	58.0	61.3	65.5	62.0	62.0
Zn	36.5	34.6	32.3	29.1	36.8	36.8
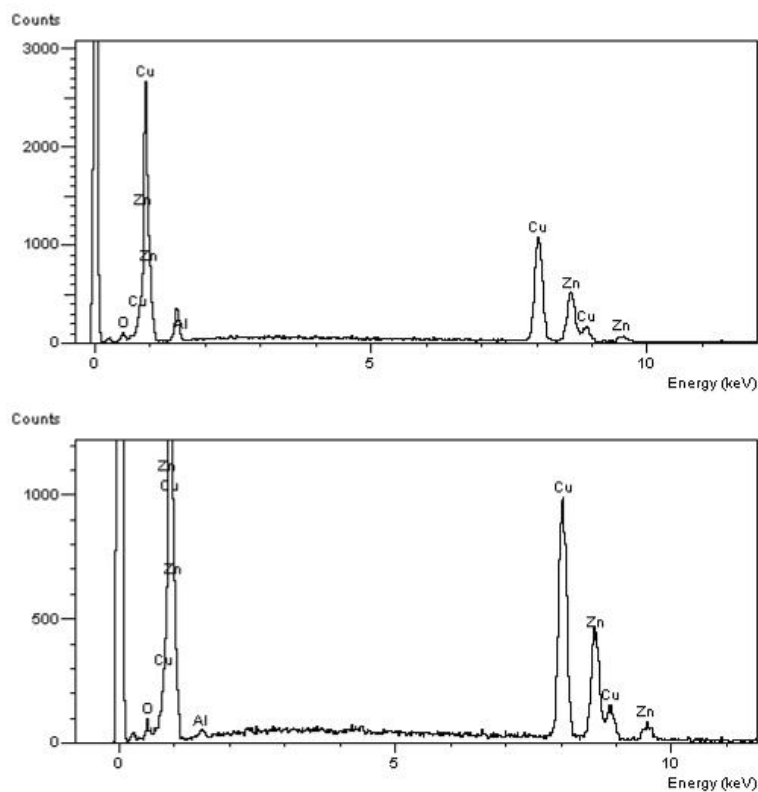
Figure 5.5   EDS Spectra obtained respectively from Area 1 and Area 2 of the external brass zone
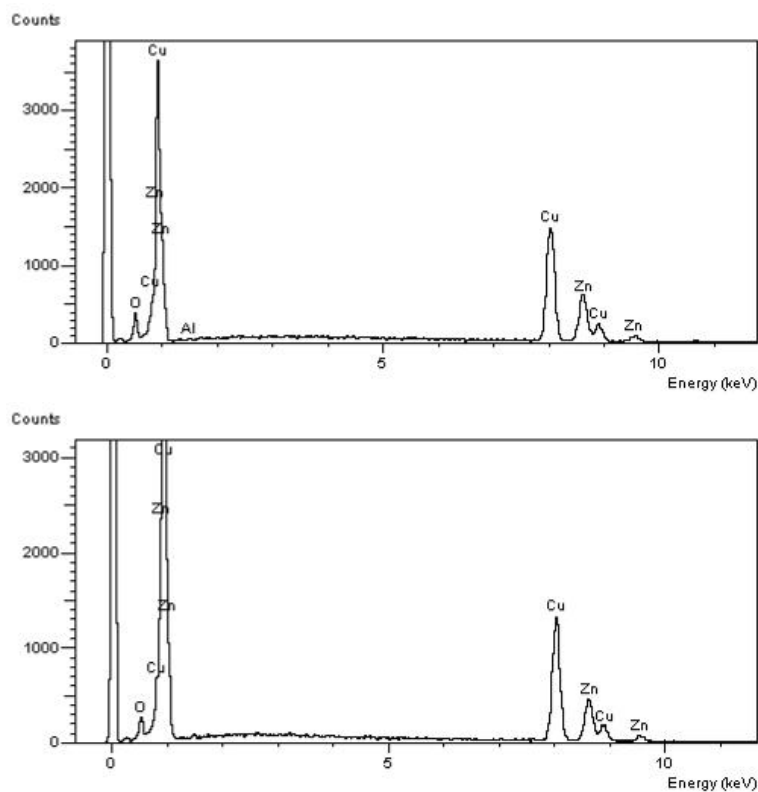
Figure 5.6   EDS Spectra obtained respectively from Area 1 and Area 2 of the intermediate dark zone
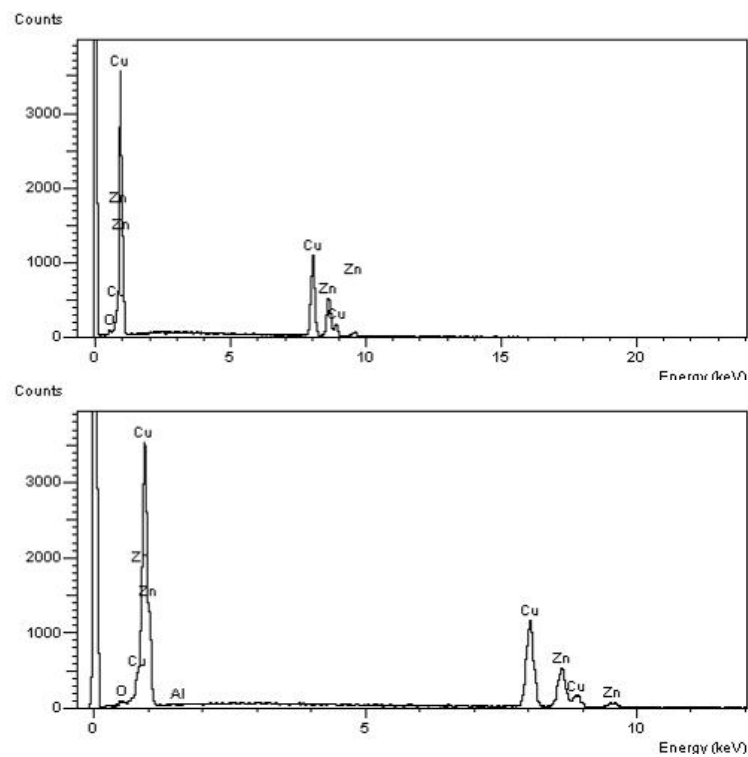
Figure 5.7 EDS Spectra obtained respectively from Area 1 and Area 2 of the central white zone

The dark area is the most oxidized. With respect to the external part, the white and the dark area are characterized by a lesser quantity of aluminum. Looking to the morphology of these zones, punctual analysis were performed to determine compositional differences. The technique of back diffusion electrons is not the more apt to seeing compositional differences because Cu and Zn, which are the elements composing brass, differ only by one atomic number, so possible increase or decrease of zinc and copper quantities are not evident, still the analyses were performed. For the dark and white area two punctual analyses were performed, as shown in figure 5.8 and 5.9. Table 5.2 shows the compositions determined from the punctual analyses, the spectra are shown in figure 5.10 and 5.11.

A map of the border between the dark and white area was constructed, see figure 5.12.

Table 5.2 Mean weight semi-quantitative compositions determined in two different points for each zone

Weight %	Dark Area		White Area	
	Point 1	Point 2	Point 1	Point 2
O	3.3	2.6	0.9	1.2
Al	0.3	-	-	-
Cu	87.0	60.4	75.1	63.0
Zn	9.4	37.0	24.0	35.8
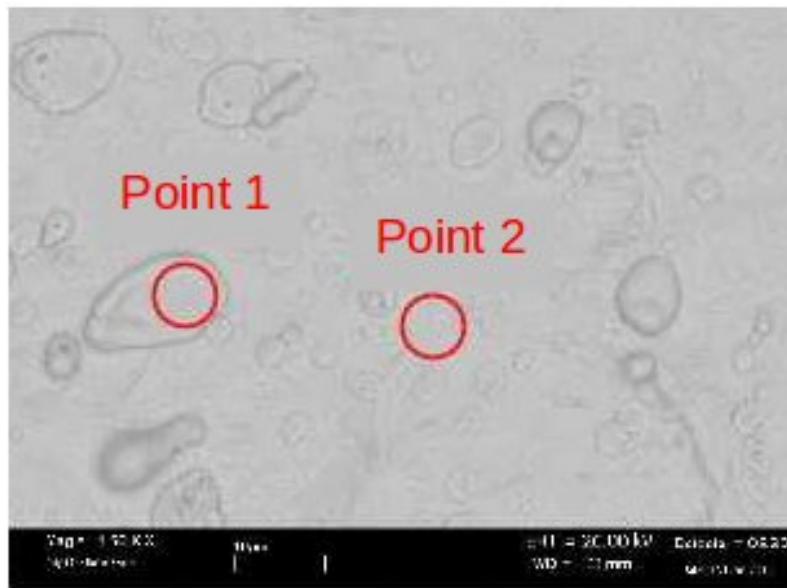
Figure 5.8   SEM image of the dark area for the punctual analysis

After analyzing all the spectra and the data of the table no significant compositional variations were found between the two areas of interest: the white and dark one; the fracture appears to be due to a mechanical or thermal effect.
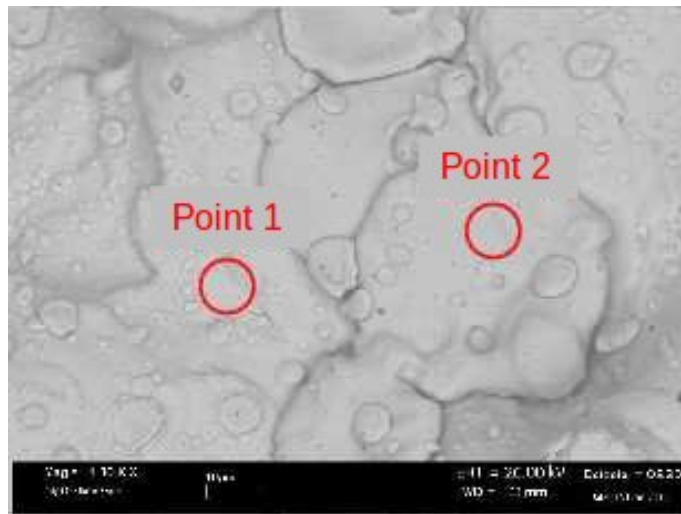
Figure 5.9 SEM image of the white area for the punctual analysis
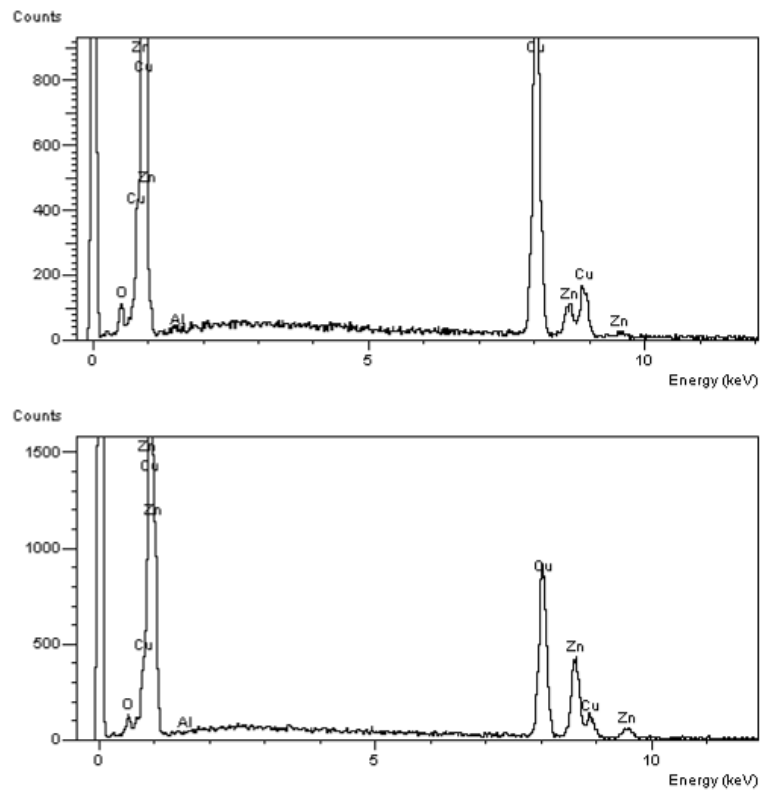
Figure 5.10 EDS Spectra obtained respectively from Point 1 and Point 2 of the dark zone
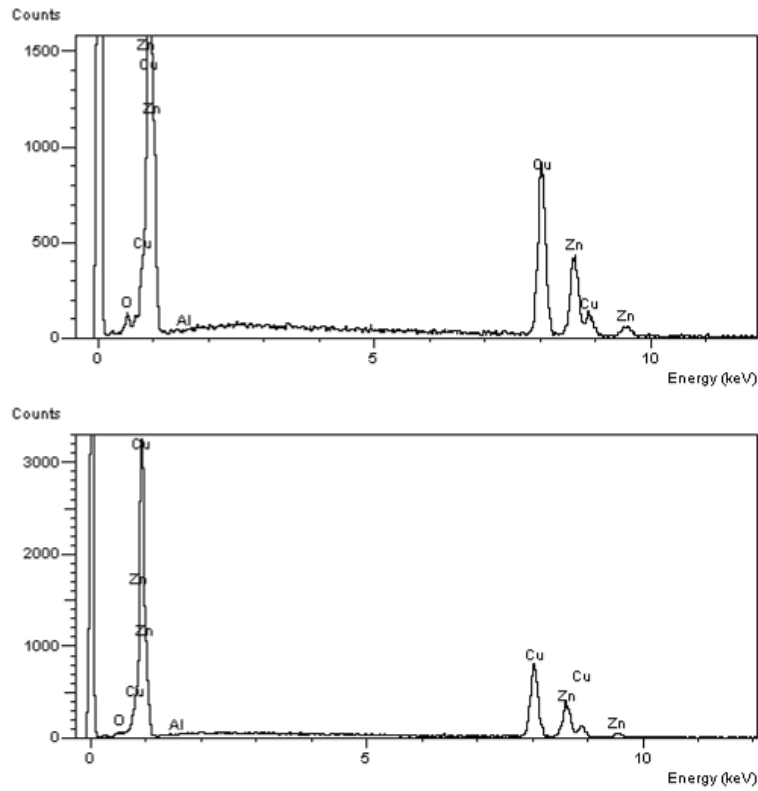
Figure 5.11   EDS Spectra obtained respectively from Point 1 and Point 2 of the white zone
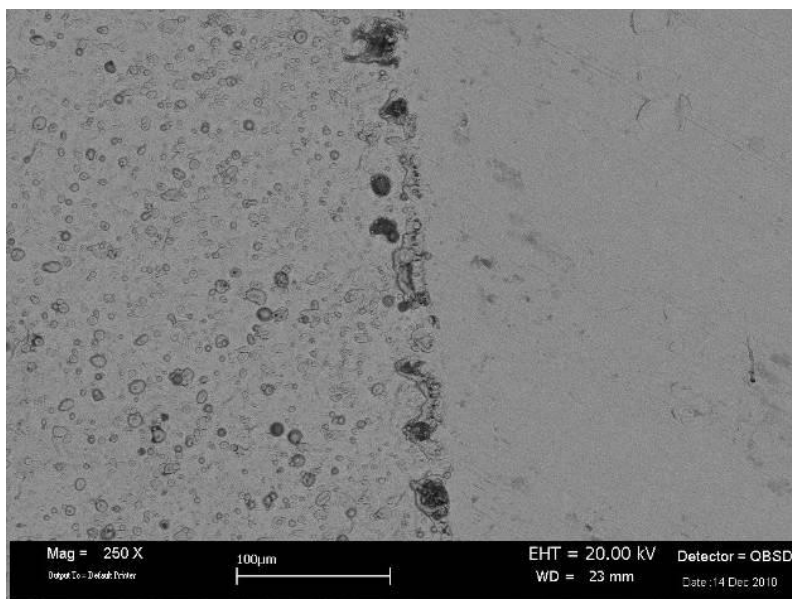
Figure 5.12   Interface between the white area and dark area

5.2 Experimental measurements of the loss of mass

Another hypothesis was that the impact of the electron beam was responsible for damaging the material target by removing mass.

To measure the erosion due to the electron beam on the brass converter, weight measurements were taken.

The experimental set up was as follow. The brass foil target is cut by hand, so the target foils are not perfectly identical. Different samples of brass foil were taken and weighed. Then these samples were exposed to varying numbers of discharges:

- the first sample: 15 discharges
- the second one: 30 discharges
- the third one: 45 discharges
- and the last one until it broke, which happened after 51 discharges

Figure 5.13 shows the different samples for the different discharges performed.

After the discharge cycle each sample was again weighed.

Having measured with a caliper the diameter of each sample and given the 50 μm thickness of the foil, the density of the brass, $8.4 \, \text{g/cm}^3$, and the weight measured experimentally, it is possible to calculate the weight loss. Table 5.3 shows the results.

Graph 5.14 is shows these results; in the x-axis is found the weight loss expressed in gram, in the y-axis the discharge number.

Figure 5.15 is the trend of the percentage variation in weight without the data on the last sample, since it is the representation of the break.

The experimental data are fitted with a 3rd order polynomial.

Looking at the fifth column of the table 5.3, the weight loss variation seems to be minimal; it can be said that the breaking of the brass foil is not due to the erosion by the electron beam, impinging on the brass foil.

Table 5.3 Weight Loss of the brass foil target after the discharges

Sample	Number discharge	Weight before P [g]	Weight after p [g]	Weight difference dP [g]	$(dP/P) \cdot 100$	$(dP/P) \cdot 100$ per discharge
1st	15	0.71591	0.71520	0.00071	0.09917	0.00661
2nd	30	0.71300	0.71086	0.00214	0.30014	0.01001
3rd	45	0.73056	0.72675	0.00381	0.52152	0.01159
4th	51	0.71148	0.70096	0.01052	1.47861	0.02899
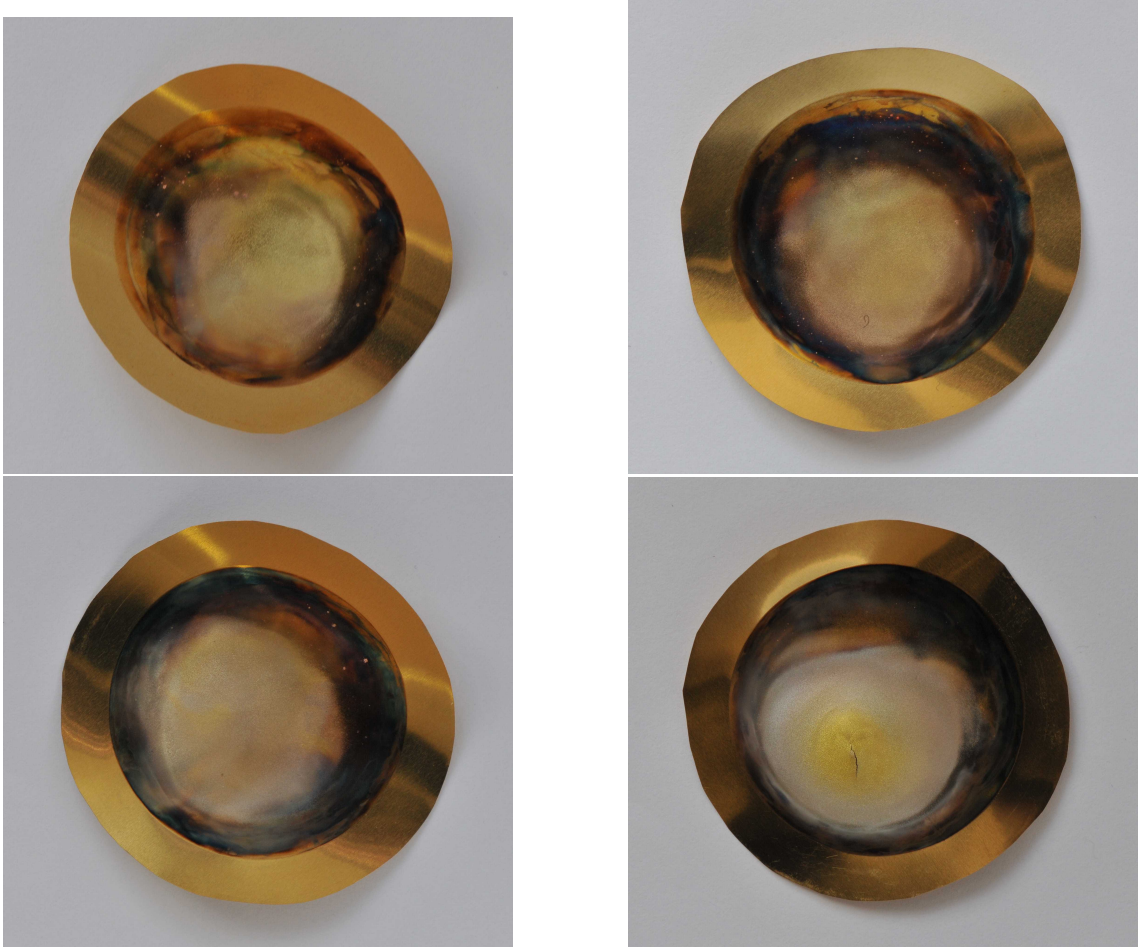
Figure 5.13   Experimental results on the brass foil from 15 discharges performed until the break
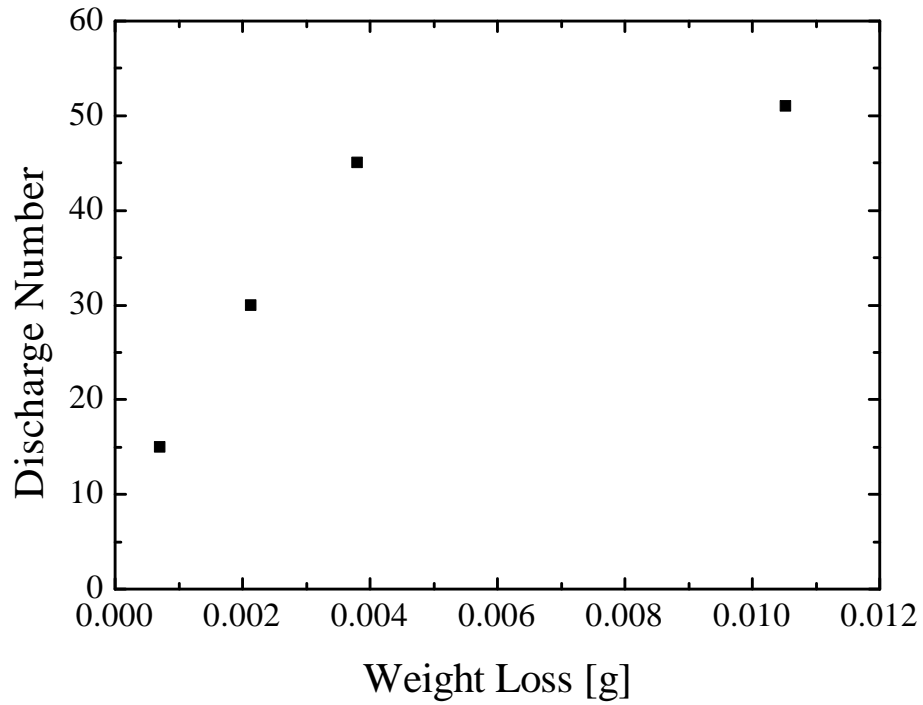
Figure 5.14 Weight loss of the brass foil for different experimental measurements
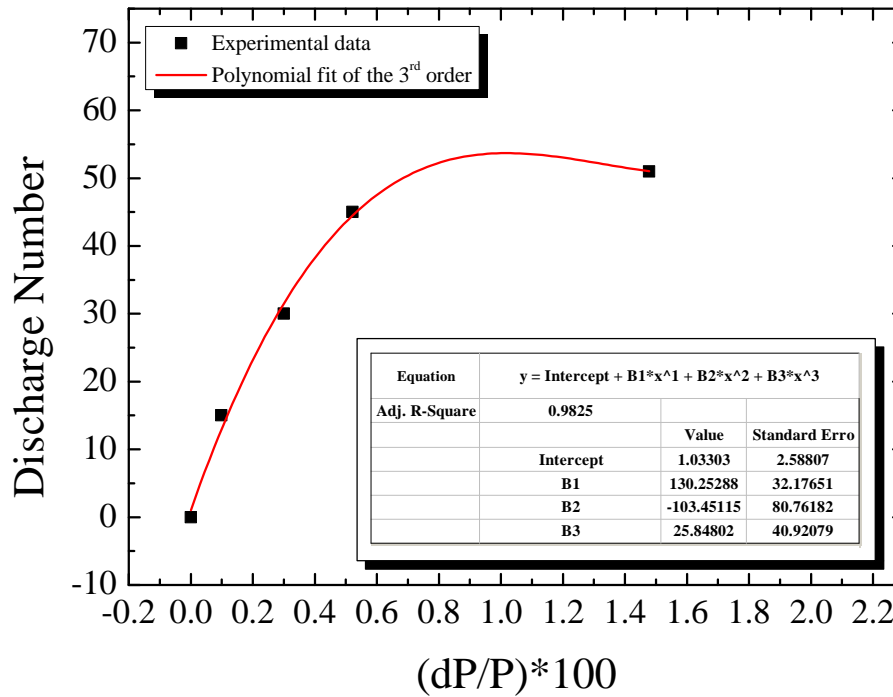
Figure 5.15 Percentage weight variation of the brass foil for the experimental measurements

5.3   Thermacam Analysis

The other point that has to be investigated is the heating of the electron beam on the brass foil target. To measure the heating, a thermal flux analysis of the PFMA-3 was performed, with a Flir Systems Thermacam PM 675.
With this study it is possible also to validate the simulation made with the MCNPX code, version 2.60, see chapter 4.

5.3.1   Experimental set-up

Temperature measurements were obtained with a thermographic camera, a Flir Systems Thermacam PM 675, having a time resolution of $0.8\,\text{Hz}$, yielding the mean temperature of the area of the brass foil impinged on by the electrons. It is possible also to obtain temperature maps of the exposed surface on which the electron beam impinges.
To performed the analysis several parameters of the Flir System Thermacam need to be set, to wit:

- reference emissivity (the black color that correspond to the value 0.99)
- ambient temperature
- humidity and
- distance at which the Thermacam is positioned,

The experimental set-up refers covering all the metallic surfaces of the drift tube, figure 5.16, around the target, which can provoke reading mistakes making reflections.

First, a plastic black structure was created around the extraction tube, figure 5.17.

A second option, more effective on reflections, was to create a matt paperboard cover, see figure 5.18.

A third option adopted to measure the temperature without reflections was to paint the brass target with a very thin layer of a matt black paint.

5.3.2   Experimental measurements: results

Two kinds of experimental measurements were performed: one analyzing only one discharge and the second one analyzing 5 discharges carried out consecutively.
One discharge of the device was analyzed storing infrared images in the shortest acquisition time: beginning $10\,\text{sec}$ before the discharge, ending 15–20 sec after the discharge, that is several times the temperature relaxation time in the thickness of the brass target (estimated as a first approximation as $s^2 \varrho c_\text{p} \backslash \pi^2 k$, $s = 50\ \mu m$ being the thickness, "ϱ" the mass density, "k" the thermal conductivity and "c_p" the specific heat, yielding few microseconds); with this relation the temperature gradient along the thickness of the target becomes so small that the temperature measured on the external surface temperature can be practically considered coincident with the average temperature of the whole disc [32].
The radius of the exposed area is $35\,\text{mm}$. The images were stored with a temporal resolution of $0.8\,\text{Hz}$, the shortest available on the camera. Once the data acquired, they were analyzed
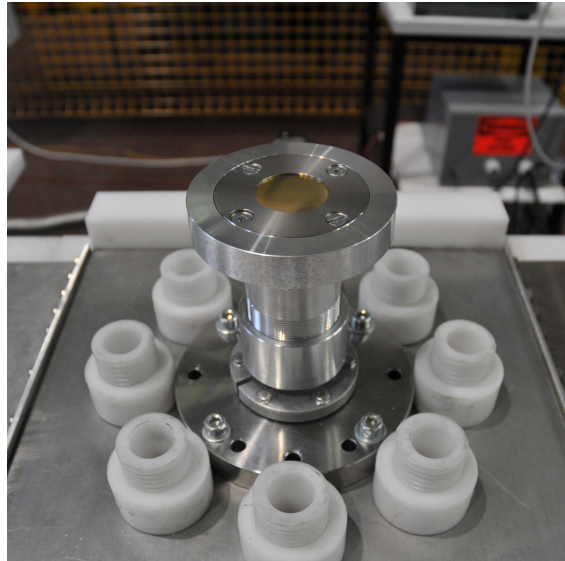
Figure 5.16   Drift tube for the electrons produced by the Plasma Focus

in Matlab.

Figure 5.19 represents the analysis of one discharge, the image on the left is taken by the Thermacam program and the image on the right is the elaboration in Matlab of the temperature iso-level.

The graduate scale has degrees Celsius as unit temperature. The one discharge analysis has the maximum temperature area above 90 °C.

The same procedure of acquisition for the image was followed to analyze five discharges in sequence, figure 5.20; it was made also a video of the increasing and decreasing temperature during the discharges.

The image on the left (of figure 5.20) is also taken by the Thermacam program and the image on the right is the elaboration in Matlab of the temperature iso-levels. The image elaborated in Matlab was the one closer to the moment of "pinch". The image in the graduate scale has again the temperature expressed in degrees Celsius.

The temperature iso-levels show that the maximum temperature reaches 160 °C, that means that this acquisition image is nearer than the previous one to the *pinch* time.

It was elaborated also a profile sequence of the temperature of a section target area passing through the maximum temperature, figure 5.21.

The x-axis is expressed in cm, the y-axis in degrees Celsius and the legend represents the profile acquisition time. The shortest acquisition time for the thermographic camera is 1.3 s. It can be seen, figure 5.21, that after 10 s the temperature comes back to ambient temperature value. The time for charging the bank capacitor before each discharge is approximately 15 s, so the heating of the electron beam impinging on the brass foil is not the cause of the target breaking. The breaking may be due to the shock wave that forms during the *pinch phase*.
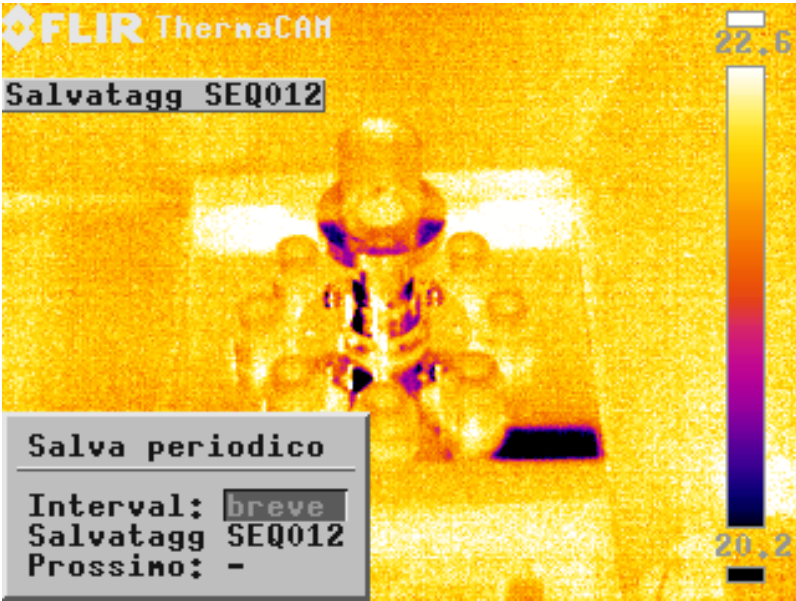
Figure 5.17   Plastic support covers all the metallic surfaces that can create reflections
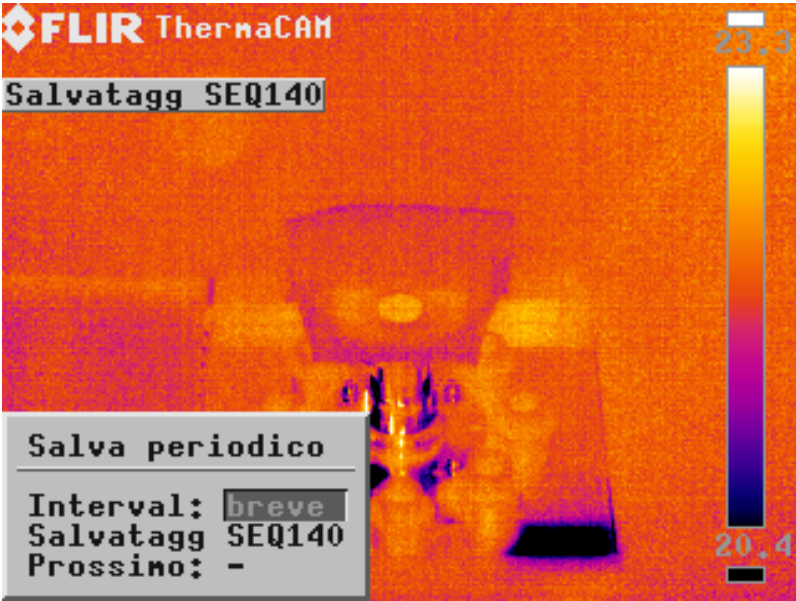
Figure 5.18   Paper support covers all the metallic surfaces that can create reflections
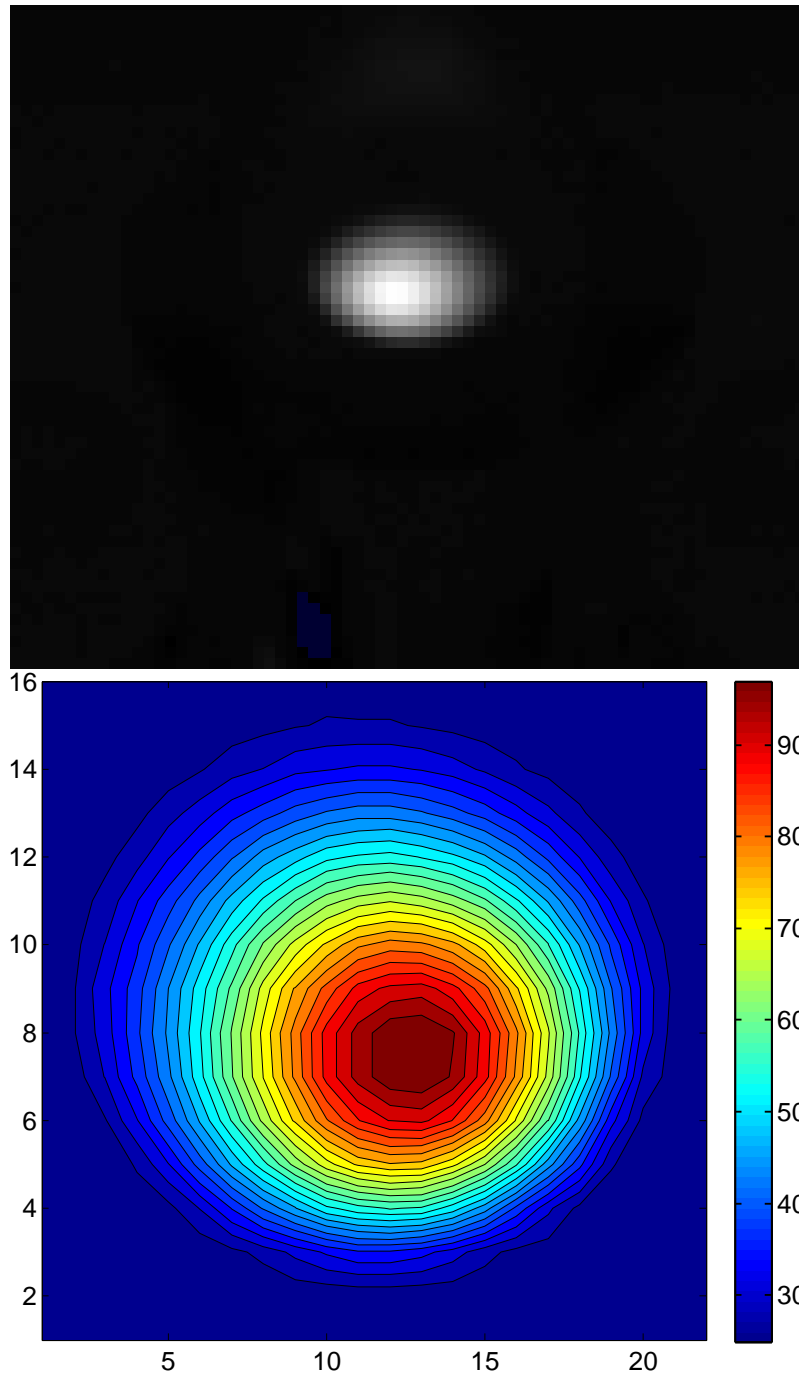
Figure 5.19   Matlab analysis: iso-level of the temperature [°C] of one discharge
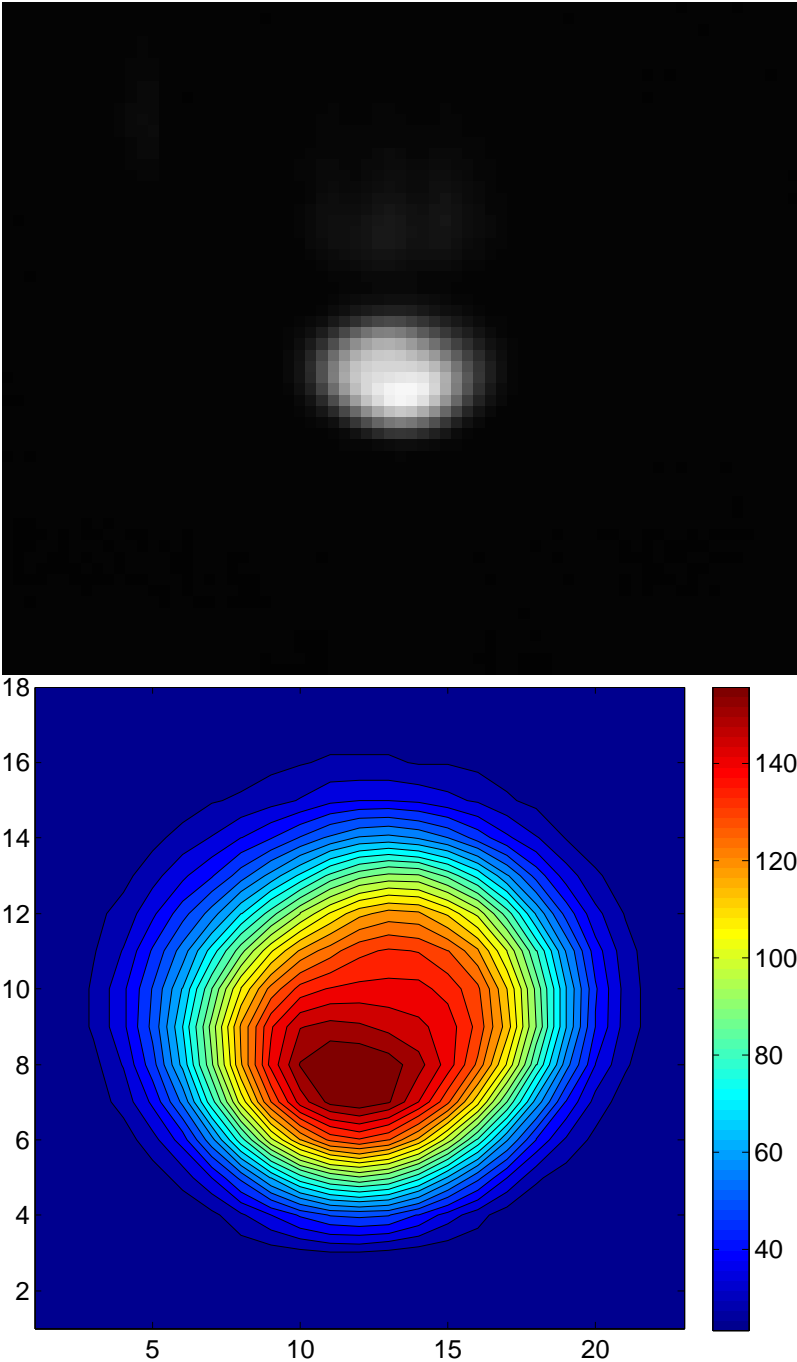
Figure 5.20   Matlab analysis: iso-level of the temperature [°C] of one discharge of the 5 sequence discharges
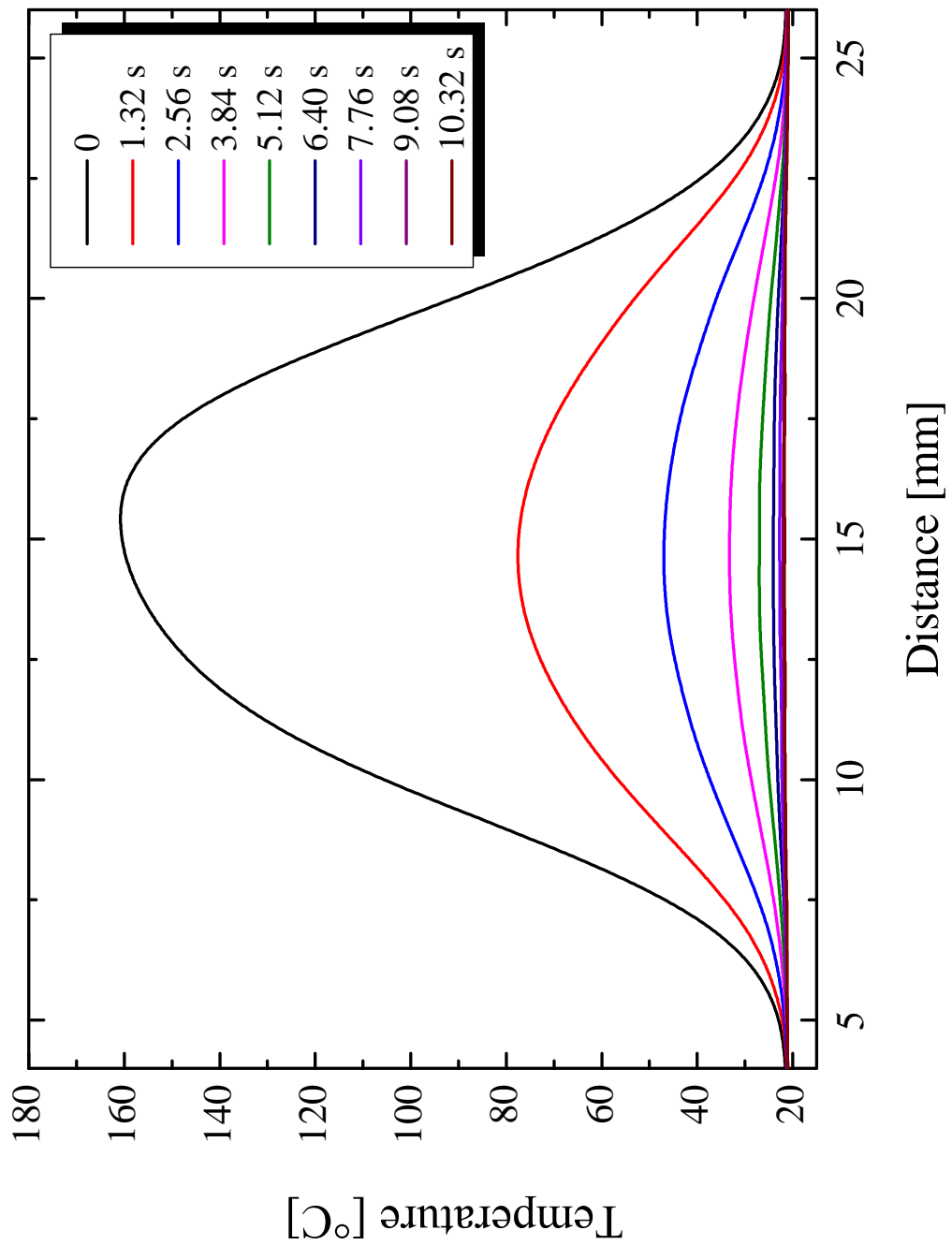
Figure 5.21   Temperature profiles for a target section

5.4   Comparison between the calorimetric measurements and the simulation results

Energy deposition in the brass foil produces heating of this latter, and the temperature thus produced can be measured. Given the small thickness of the brass foil, the average surface temperature has been assumed as representative of the whole depth of the foil. From the temperature rise ΔT the dose deposited can be estimated. It is worth clarifying that a possible systematic error in the absolute calibration of the Thermo-camera would be of no concern, since the temperature difference ΔT is used for these evaluations.

Knowing the mass "m" and the specific heat "c_p" of the brass, the energy ΔE deposited can be calculated as:

$$\Delta E = m \cdot c_{\mathrm{p}} \cdot \Delta T \tag{5.1}$$

and hence the average dose D:

$$D = \frac{\Delta E}{m} = c_{\mathrm{p}} \cdot \Delta T \tag{5.2}$$

This value in turn can be compared to the dose calculated in the MCNPX simulation, offering a benchmark to evaluate the simulation, [30].

Experimental measurements yielded a mean temperature of $73\,°\mathrm{C}$ in the area stricken by the electron beam, with an ambient temperature of $25\,°\mathrm{C}$, i.e., $\Delta T = 48K$. Considering a specific heat of $378\,\mathrm{J\,kg^{-1}\,K^{-1}}$ a mean dose of $18.1\,\mathrm{kGy}$ is calculated. To calculate the dose with MCNPX code the "F6" tally is used, calculating the energy deposited per unit of mass and per particle. The simulation calculates the doses from electrons and photons produced by the electrons, in spatial steps of $12.5\,\mathrm{\mu m}$ across the foil thickness.

In the simulations MCNPX takes into account also of the production of secondary electrons and photons. Figure 5.22 and Figure 5.23 present, respectively, the doses deposited by electrons, and by photons produced by electrons in the foil, all after appropriate unit conversion.

As can be seen, the contribution from electrons is greater than that due to photons by over one order of magnitude. This is consistent with what one would expect. The simulation gave a mean dose of $17.9\,\mathrm{kGy}$, which compares very satisfactorily with the experimental measurement, adding to the reliability of the simulation.
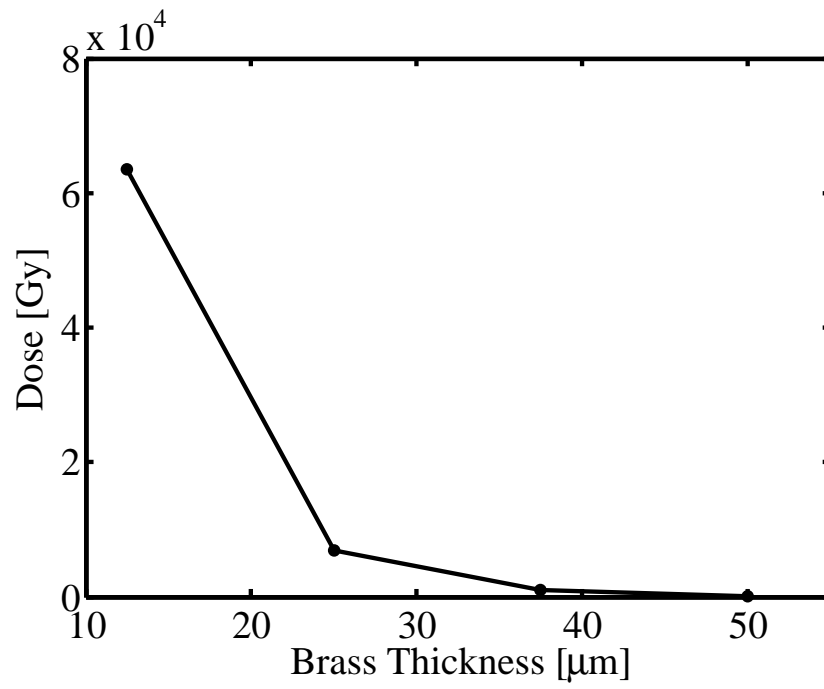
Figure 5.22   Dose deposited by electrons in the target foil
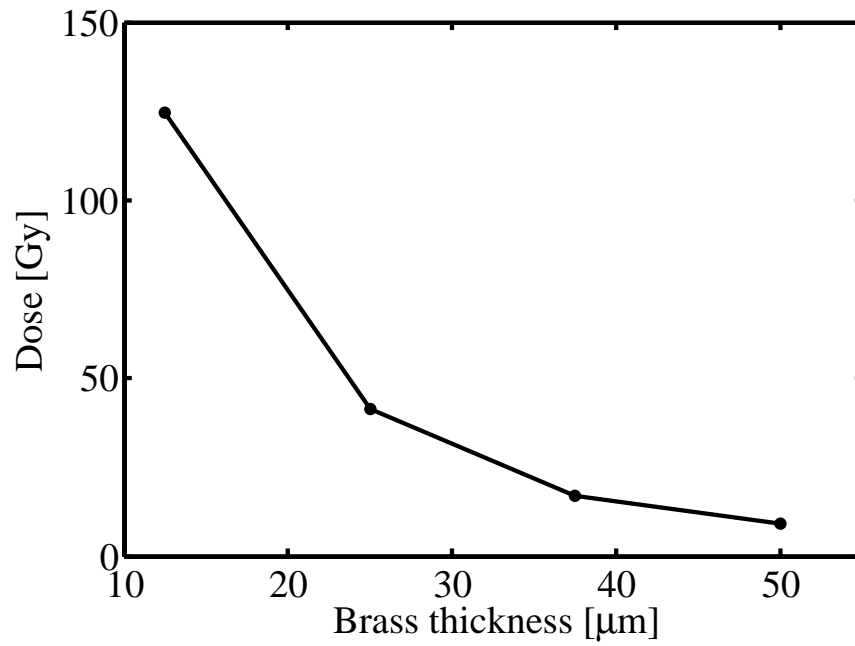
Figure 5.23   Dose deposited by photons in the target foil

Chapter 6

Design development of the cell culture holder

This chapter is dedicated to the design development of the cell holder used for the cell culture irradiations. This project was a collaboration with the radio-biologists group, as was explained in the introduction, and they have put forth requests to improve the cell holder for their analysis.

6.1 First configuration of the cell holder

The first configuration of the cell holder, figure 6.1, is a hollow, cylindrical central piece 3 cm long and with a 3.9 cm inner diameter, threaded at both ends to accommodate sealing end pieces. The Mylar foil is 30 µm thickness and the cell culture is seated on it in a aqueous solution, offering an exposed area with a diameter of 35 mm. The closure with the end pieces is mechanical. The sealing secured by a Teflon o-ring with a rectangular section. The thread must be very fine to prevent leakage, it must be recalled that the work of the radio-biologist group is conducted under a hood. (The AutoCad drawing of this cell holder was shown in Chapter 3, figure 3.12)

This first configuration has the problem that the 30 µm Mylar foil has a diameter of 4 cm and the *petri* dish, used for the radio-biological analyses, has a diameter of 3 cm. To conduct the analysis, the cell culture has to be removed from the Mylar foil and re-positioned on the *petri* dish, provoking a high mortality in the cell culture.

Another problem is that sometimes this cell holder is not water tight enough, so the following solutions for both problems were sought.

Stainless steel rather than plastic was selected, because the holder needs to be sterilized at very high temperature. The Mylar foil is sterilized with an ethanol solution.

Figure 6.1   Cell holder: first configuration

6.2   Second configuration of the cell holder

Second configuration, figure 6.2, is still a hollow, cylindrical central piece 3 cm long, threaded at both ends to accommodate sealing end pieces. The closure is again mechanical, the external surfaces of the three principal pieces are milled.

The material and the dimensions of the piece are the same; for this configuration, the exposed area has a diameter of 26 mm and the thread is improved, decreasing leakage. The diameter of the 30 μm Mylar foil is of 2.8 cm and it can be positioned directly on the *petri* dish to be analyzed. The sealing is obtained with two Teflon o-rings for each end piece, having rectangular section with the same dimensions of the previous one, and the Mylar foil, with the cell culture in aqueous solution, is located between the two o-rings.

Figure 6.2 Cell holder: second configuration

6.3 Third configuration of the cell holder

The third configuration, figure 6.3, has again a hollow, cylindrical central piece 3 cm long, threaded at both ends for the sealing end pieces, but has the better mechanical closure and better water sealing with respect to the precedent configurations. The materials and the dimensions are not changed.

As for the second configuration, the three parts of the cell holder have the external surfaces milled to afford a good grip closing by hand. The sealing is made with a silicon o-ring, having a circular section, positioned inside the central hollow body. There is a groove in the end part of the central hollow piece (can be seen in figure 6.3) where the o-ring can be seated.

The exposed area has a diameter of 20 mm and the Mylar foil diameter is always 2.8 cm to position it directly in the *petri* dish for the radio-biological analysis.

In the first configuration the aperture of the exposed area has a thickness of less than

Figure 6.3   Cell holder: third configuration

1 mm, in the second case the Mylar foil is positioned between the two teflon o-ring and the thickness became 2 mm, for the last configuration it is of 1.5 mm.

After the attenuation studies of the x-ray production and the radio-biological analyses, the final configuration adopted was the 3rd, for the reasons just mentioned: the diameter of the Mylar foil and the best mechanical closure and sealing.

Studies are in progress on the effect of x-ray scattering produced by the walls of the holder during the cell culture irradiations, to understand if this produces a variation in the dose deposited.

Chapter 7

Efficiency of the PFMA-3 with different working conditions

Several experimental measurements were performed to analyze the efficiency of the Plasma Focus device in different working conditions, changing:

- pressure and
- voltage

parameters. Testing the efficiency of PFMA-3 means evaluating the electron spectrum and x-ray production changes, while varying the working conditions, using the the magnetic spectrometer described in chapter 2, to measure the electron spectrum and the dosimetric stack of GAFCHROMIC® film to evaluate the x-ray production.

7.1 Electron spectrum with different working conditions

7.1.1 Electron spectrum with different pressure conditions

Nitrogen pressure was varied first, keeping the working voltage at 18 kV. Three different pressures were chosen:

- 0.40 mbar
- 0.45 mbar
- 0.50 mbar

To analyze the electron spectrum each HD-810 GAFCHROMIC® film was irradiated with several discharges. In the beginning, the number chosen was 6 discharges (see figure 7.1).

As cab be seen in figure 7.1, there is a "plateau" in the top of the elaborated electron spectrum. This means that the GAFCHROMIC® film is saturated (we recall that the HD-810 GAFCHROMIC® film has a dose range between 10 to 250 Gy). To understand the real trend of the electron spectrum, it is important not to saturate the GAFCHROMIC® film hence series of fewer discharges were performed, focusing only on the two most promising
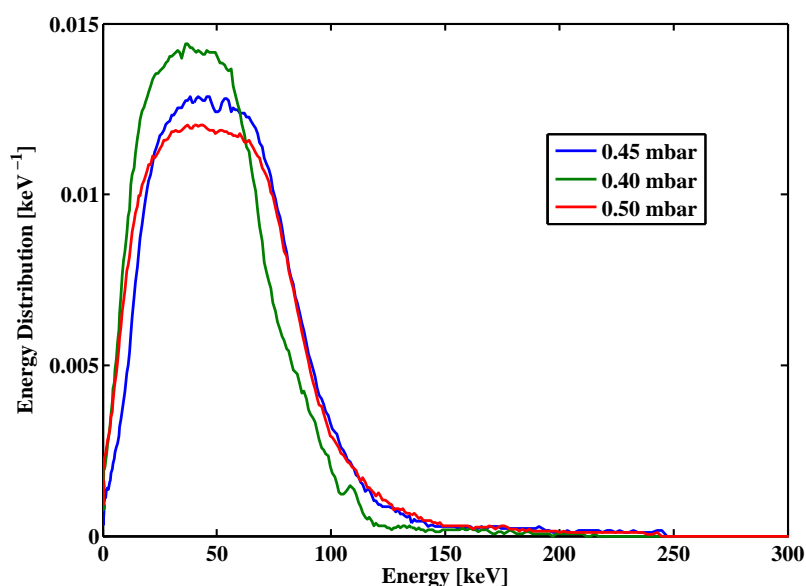
Figure 7.1   Comparison between spectrum performed at different nitrogen pressures: 6 discharges, 18 kV

pressures.

Series of 4 discharges were tried, figure 7.2, but saturation of the film was still present; hence series were sealed down to 3 discharges, and the saturation was not reached, see figure 7.3. Figure 7.1 is still useful to analyze the tails of the electrons at higher energies. As was mentioned before, GAFCHROMIC® film has a dose range, with a minimum threshold for blackening (10 Gy), and the tails at higher energies are less intense compared to the mean energy and need more discharges to be detectable in the film.

The three different pressures were compared again at the working voltage of 20 kV. Figure 7.4 is the electron spectrum of 6 accumulated discharges, used to analyze the tails of the electrons at higher energies, figure 7.5 is obtained with 4 and figure 7.6 with 3 accumulated discharges. This last figure is used to analyze the real trend of the electron spectrum at 20 kV.

From the graphs it can be inferred that the best working pressure is 0.45 mbar for both 18 kV and 20 kV, even though the difference is not so remarkable. Of more consequence the comparison between the two different working voltage conditions illustrated in the following paragraph.

7.1.2   Electron spectrum with different voltage conditions

This paragraph is dedicated to the comparison of the electron spectrum for two different working voltages:

- 18 kV
- 20 kV
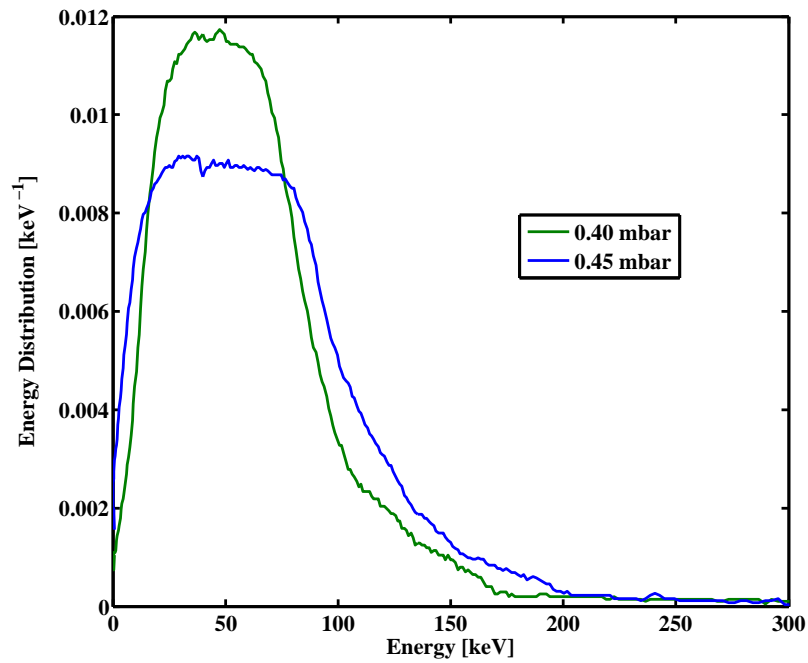
Figure 7.2 Comparison between spectrum performed at different nitrogen pressures: 4 discharges, 18 kV
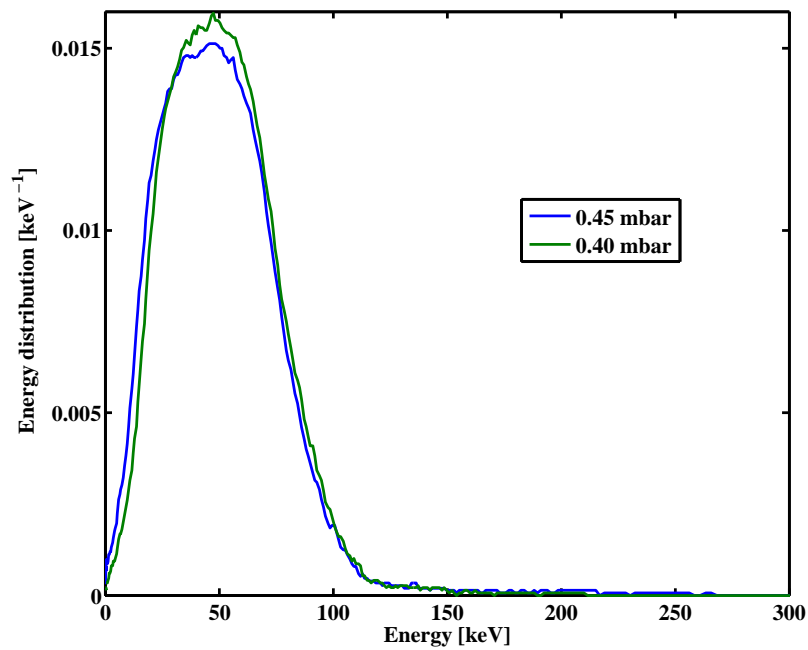
Figure 7.3 Comparison between spectrum performed at different nitrogen pressures: 3 discharges, 18 kV
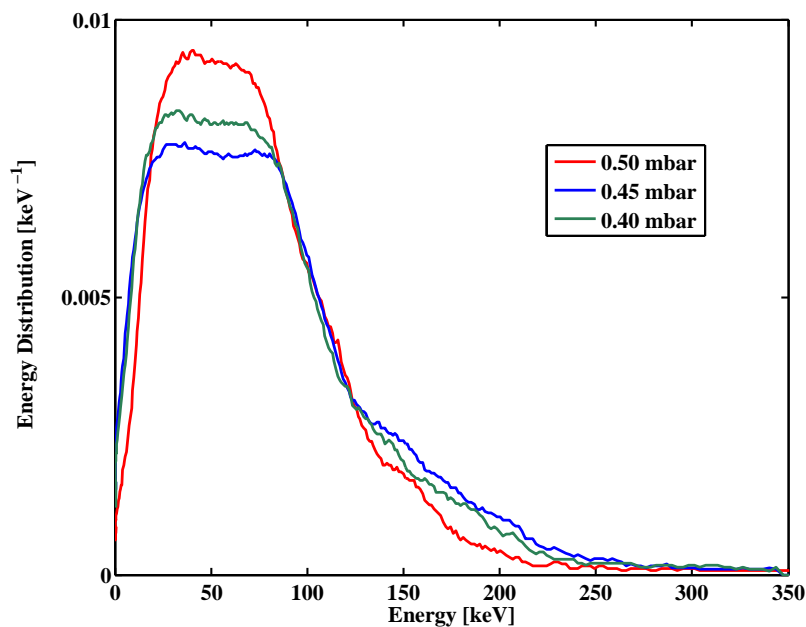
Figure 7.4 Comparison between spectrum performed at different nitrogen pressures: 6 discharges, 20 kV

The procedure is the same as in the previous analysis: to identify the best electron spectrum, 3 accumulated discharges were used, as reported in figure 7.7; to analyze the higher energy tail of the electrons, 6 accumulated discharges were used, saturating a part of the HD-810 GAFCHROMIC® film, see figure 7.8.

The pressure chosen for this analysis was the one determined as the best in the previous comparison: 0.45 mbar.

From figures 7.7 and 7.8 one can see how the 20 kV working voltage brings about an increase in the energy tail of approximately 50 keV.

To understand if this positive behavior is repetitive, several experiments were performed with different number of accumulated discharges, figure 7.9.

Figure 7.9 is obtained comparing only higher energy tails, as discussed in chapter 2.

The tails are repetitive, so it is of interest to investigate the intensity of the electron beam and the x-ray production.
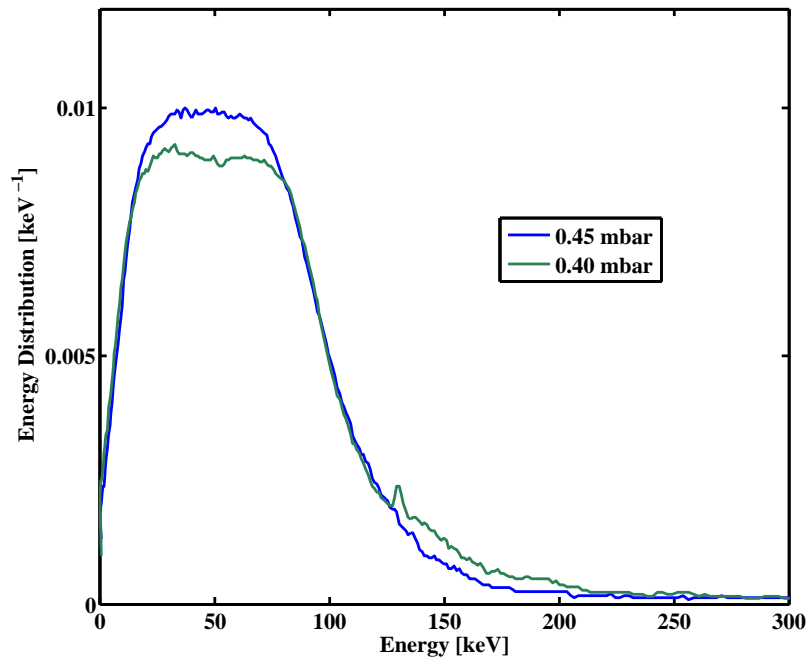
Figure 7.5 Comparison between spectrum performed at different nitrogen pressures: 4 discharges, 20 kV
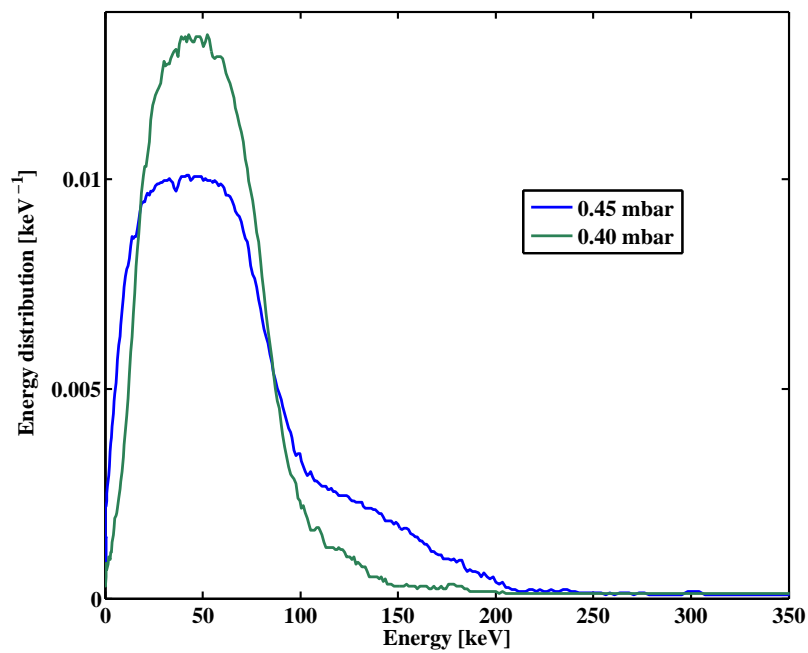
Figure 7.6 Comparison between spectrum performed at different nitrogen pressures: 3 discharges, 20 kV
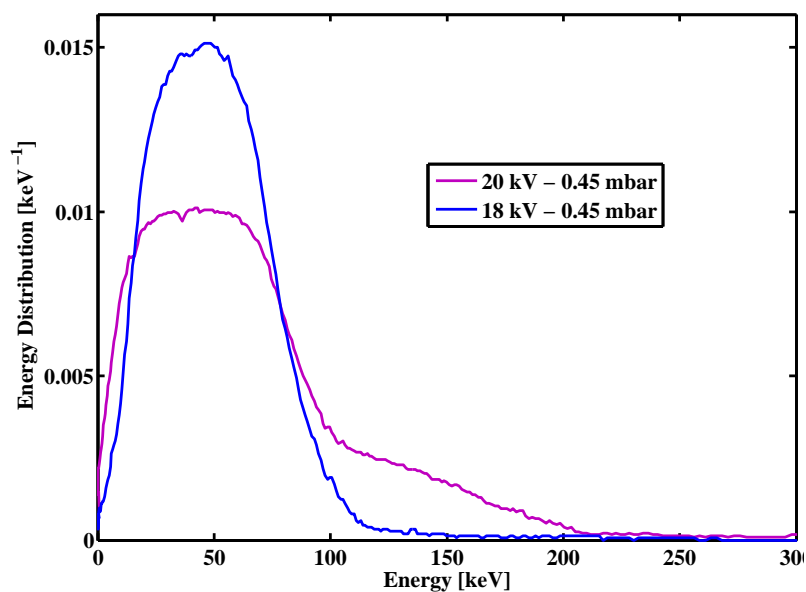
Figure 7.7 Comparison between spectrum performed at different working voltage: 3 discharges, 0.45 mbar
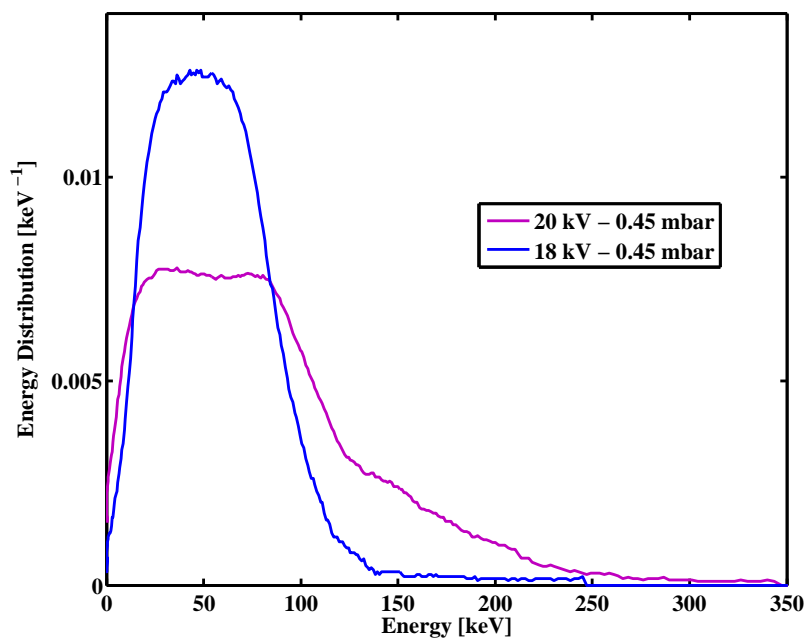
Figure 7.8 Comparison between spectrum performed at different working voltage: 6 discharges, 0.45 mbar
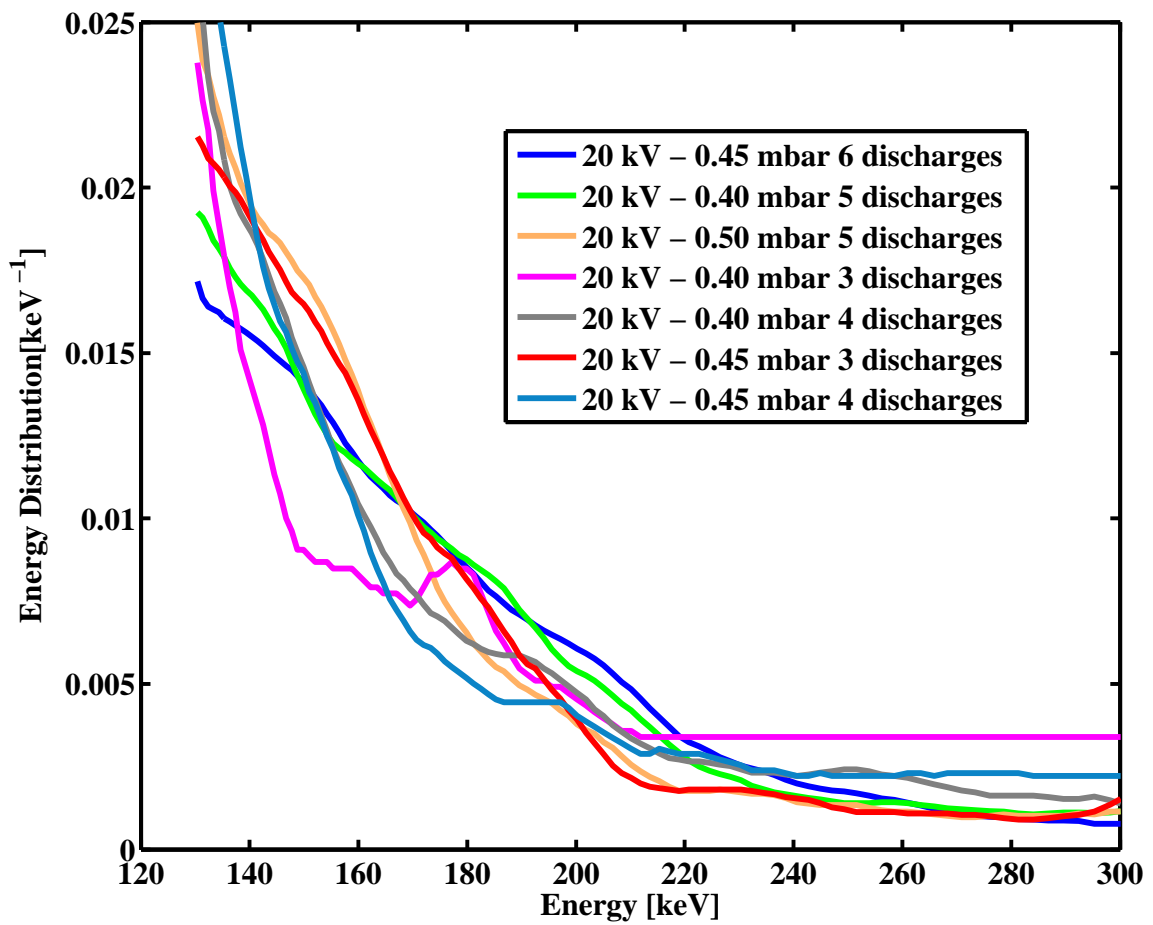
Figure 7.9 Tail of the electron at high energies, $20\,\text{kV}$ and $0.45\,\text{mbar}$

7.2   Electron beam measurements

To understand if this positive behavior of the increasing of the energies in the electron spectrum has also a positive reflection on the intensity of the electron beam, current measurements were performed, with the Rogowski coil described in the chapter 1, positioned at the end of the extraction tube, see figure 7.10. The Rogowski coil is connected to the oscilloscope through a shielded BNC cable. The cable is connected in such a way as not to touch other BNC cables and the oscilloscope to which the cable is connected and is positioned 3 m away from the Plasma Focus device, these measures are taken to avoid possible electromagnetic disturbances to signal.

The electron beam measurements were taken at 18 kV for two pressures: 0.45 mbar and 0.4 mbar. The results are shown in table 7.1.

The same measurements were then taken at 20 kV, the results are shown in table 7.2.

In the first column of the tables the working pressure is reported, in the second column the number of the experiment, in the third the number of the *pinches*, in the fourth the charge measured, in the fifth the mean charge measured for all the experiments, and in the last one the standard deviation on the value of the mean charge.

From the current measurements, can be noticed that there is no significant difference in the intensity of the electron beam measured at 18 kV or at 20 kV. The more efficient pressure is 0.45 mbar for both working voltages, because at 0.4 mbar, often two *pinches* develop, indicating that the plasma sheet is not compressed in a good way.

It is important to say that in the experiments performed at 20 kV, most of the time the oscilloscope switches off due to the large electromagnetic disturbances, maybe due to the very intense current flowing in the Plasma Focus device.

Table 7.1 Current measurement of the electron beam for $18\,\mathrm{kV}$

Pressure [mbar]	Experiment	*Pinch* number	Q [mC]	Mean Q [mC]	Std
	1	1	0.12		
	2	1	0.25		
0.45	3	1	0.37	0.22	0.10
	4	1	0.17		
	5	1	0.18		
	1	1	0.18		
	2	2	0.10		
0.40	3	2	0.30	0.26	0.14
	4	2	0.22		
	5	2	0.48		

Table 7.2 Current measurement of the electron beam for $20\,\mathrm{kV}$

Pressure [mbar]	Experiment	*Pinch* number	Q [mC]	Mean Q [mC]	Std
	1	1	0.22		
	2	2	0.20		
0.45	3	1	0.41	0.23	0.11
	4	2	0.16		
	5	1	0.16		
	1	2	0.28		
	2	2	0.18		
0.40	3	2	0.40	0.22	0.12
	4	2	0.12		
	5	2	0.13		

Figure 7.10   Setting of the Rogowski coil used for the current measurements

7.3   Attenuation measurements with different working conditions

To understand the efficiency of PFMA-3, the x-ray production needs to be investigated together with the dose deposited.

The x-ray production is connected to the electron spectrum, because the component at high energies of the x-ray spectrum calculated in the Monte Carlo simulations (see chapter 4) is due to bremsstrahlung.

7.4   Attenuation measurement configuration

The attenuation measurements of the x-rays produced by the Plasma Focus device were compared for different working voltages. Working pressure changes were not considered since they did not show significant variations in the electron spectrum, as was discussed in the previous paragraphs.

The configuration of the irradiation measurements was changed, see figure 7.11.

Figure 7.11 is a schematic representation: after the aperture of the drift tube outside the brass foil, there is a stainless steel collimator 9 mm long. Summing the thickness of the aperture to the height of the collimator, the first GAFCHROMIC® film is positioned 1 cm from the brass foil.

The collimator has an exposed area of 20 mm. This aperture for the collimator was chosen, for the cell culture irradiations. In what follows, the cell holder used in the irradiations will be the one of the 3$^{\text{rd}}$ configuration, see chapter 6; it was also positioned at sufficient distance to have a more uniform irradiated area.

A stack of GAFCHROMIC® film was used for the attenuation measurements: the first film sheets, as usual, is a HD-810 GAFCHROMIC® film used as a filter for the electrons passing through the brass foil that would not attenuate significantly the x-ray emission.
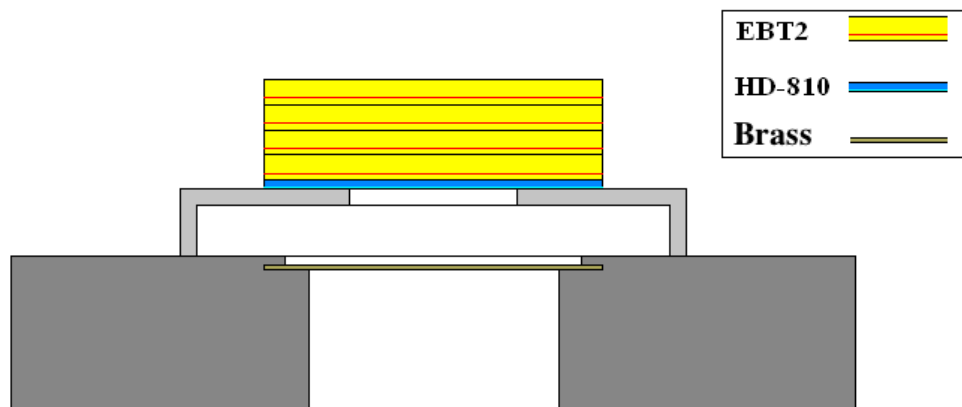
Figure 7.11 Configuration of the X-rays attenuation measurements

The last four film sheets are of EBT2 GAFCHROMIC® film.

Figure 7.12 reported an example of irradiation of a film stack performed at 18 kV.

Figure 7.13 is an example of irradiation of a film stack performed at 20 kV.

The irradiation measurements follow 5 accumulated discharges for each stack.

The samples are scanned, as described in the chapter 3, by an HP Laser Jet M1522n in reflection mode, with 300 dpi resolution, converted to an 8-bit gray scale.

To evaluate the dose deposited the film sheets are analyzed in Matlab, as usual. The input file of the analysis was modified, following explanation by radio-biologist colleagues that the cell culture is moved during the analysis and it is impossible to recognize the position of the cell culture in the Mylar foil. The first input calculated the dose deposited of the 80% of the exposed area, with the final Matlab input it is possible to calculate the mean dose of all the area, using a geometrical method. This result is more useful for the radio-biological analyses.

The modified part, in the Matlab input, is illustrated below:

```
1  %Geometrical Method
2  x=(0:0.085:450*0.085);
3  y=(0:0.085:450*0.085);
4  centro=[xcentro*0.085  ycentro*0.085]
5  dim=size(data3);
6  Mdose=zeros(dim(1),dim(2));
7  for i = x_min:x_max
8      for j = y_min:y_max
9          if (x(j)-centro(1))^2+(y(i)-centro(2))^2<17^2
10             Mdose(i,j)=data3(i,j);
11         end
12     end
13 end
```
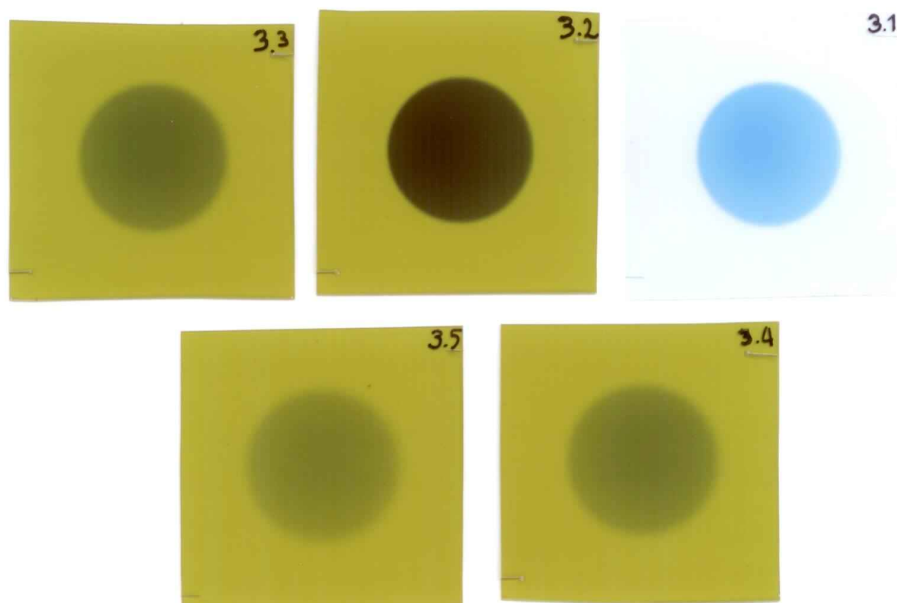
Figure 7.12   Example of irradiation with new configuration
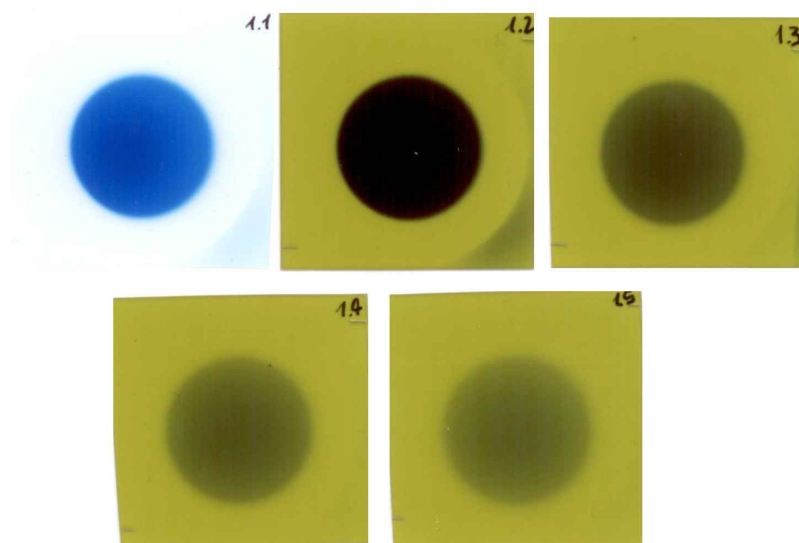
Figure 7.13   Example of irradiation with new configuration

```
14   clear i
15   clear j
16   figure
17   contourf(Mdose,0:0.5:8.0), colorbar
18   z=0;
19   clear dose
20   for h = 1 : dim(1)
21       for k = 1 : dim(2)
22           if Mdose(h,k) > 0
23               z=z+1;
24               dose(z)=Mdose(h,k);
25           end
26       end
27   end
28   dose_media= mean(dose)
29   sigma_dose= std(dose)
30
31   dose_max = max(max(Mdose))
32   dose_media_m=data3(190:355,160:330);
```

To calculate the mean dose it is necessary to locate the center of the irradiated area, with the coordinate of the beginning and the end of the circle, and the mean dose is calculated on all the effective area. Figure 7.14 is an example of the Matlab analysis, representing the isodose levels of the last three film sheets of the irradiation measurements performed at 20 kV. The last three film are the ones important to obtain the attenuation correlations, since they are not stricken by electrons and they can simulate the cell culture. Figure 7.15 is the representation of the isodose level in 3D.

To convert the gray levels to dose values the calibration curve described in the chapter 3 is used.

7.4.1   Result of the attenuation measurements

These attenuation measurements were performed to study the effect of the voltage conditions on the dose deposited and to decide where the cell culture had to be positioned.

After measuring the mean dose deposited in each film sheets, the ratio between doses to the 4th and then 3rd film and between these the 5th and 4th film was calculated.

Figure 7.16 shows the attenuation correlation for several tests performed at 18 kV; figure 7.17 at 20 kV. In the x-axis is reported, first, the ratio between the 4th and 3rd film and likewise second, between the 5th and 4th; in the y-axis the corresponding values.

From both graphs, it is possible to notice that the first relation between 4th and 3rd has less fluctuation, so the cell culture can be simulate by the fourth film, reading directly the dose deposited from the third film. The correlation between 4th and 3rd for the mea-
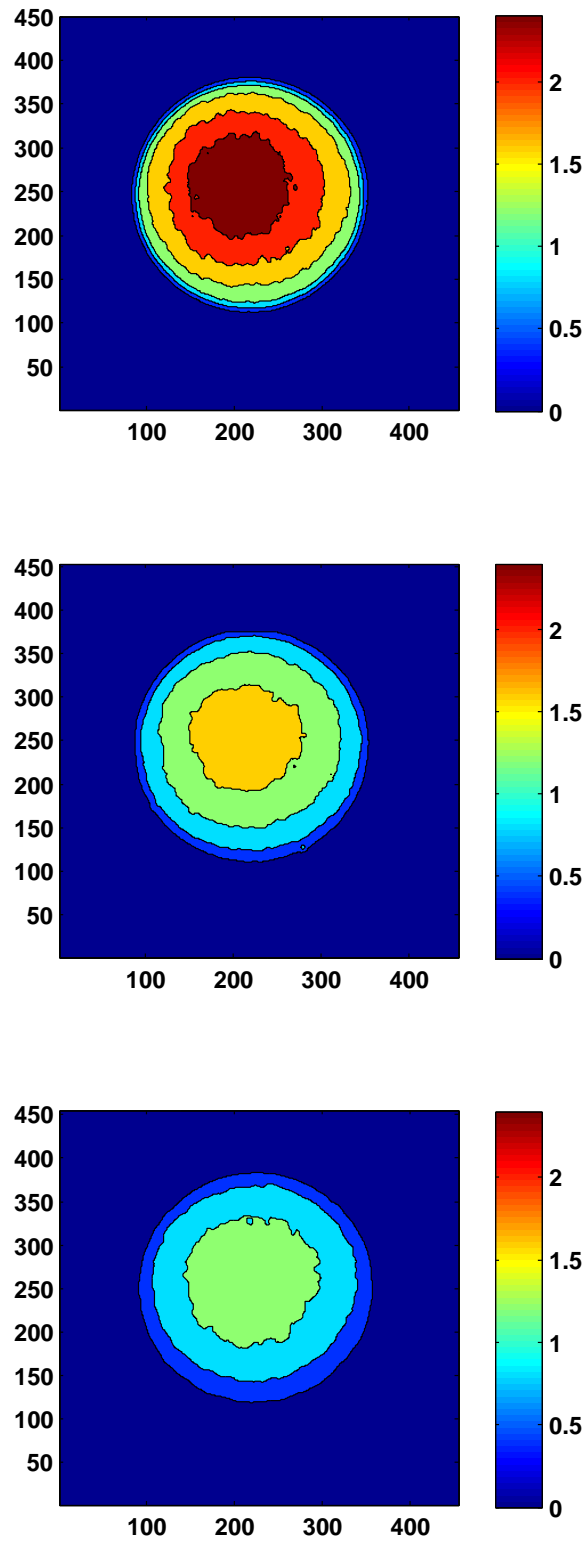
Figure 7.14 Isodose level obtained from Matlab elaboration (Dose expressed in gray)
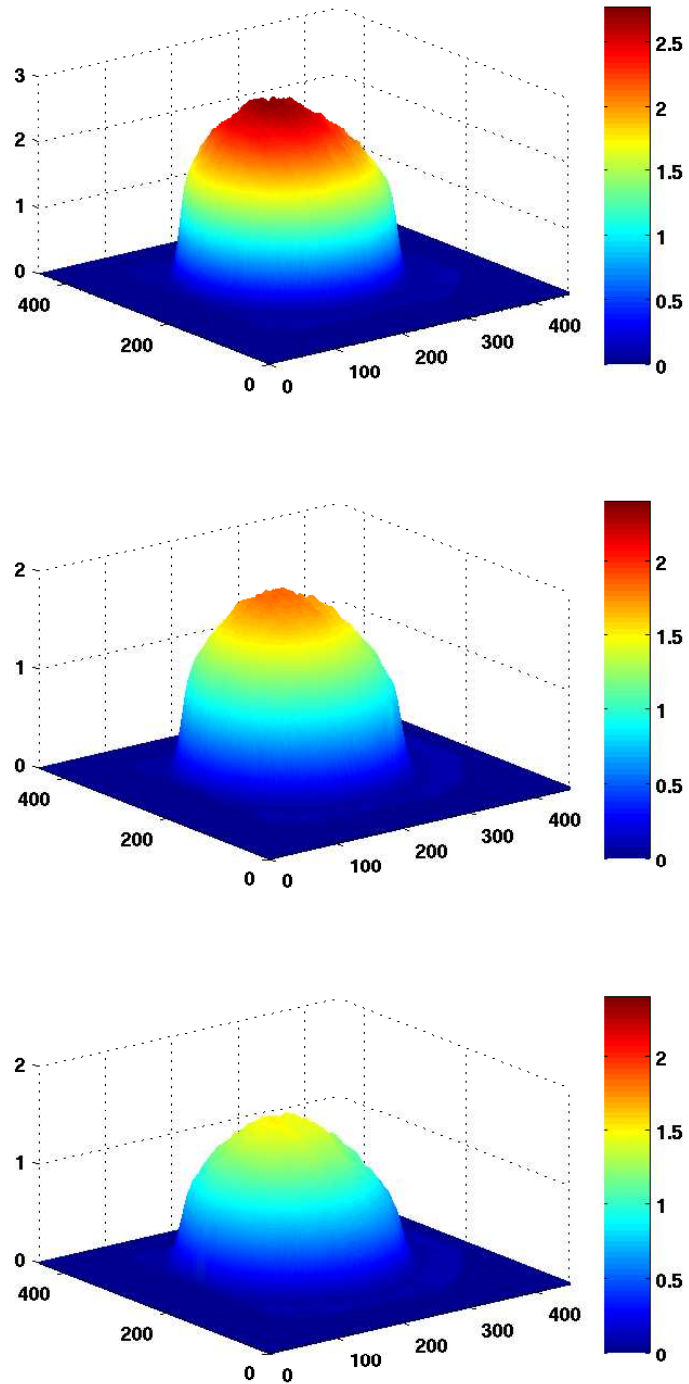
Figure 7.15 Isodose 3D level obtained from Matlab elaboration (Dose expressed in gray)
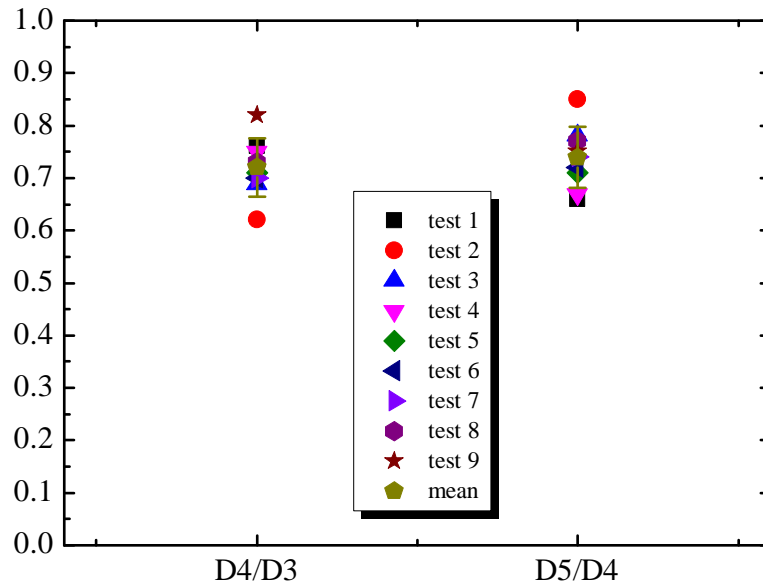
Figure 7.16   Attenuation measurements performed at 18 kV
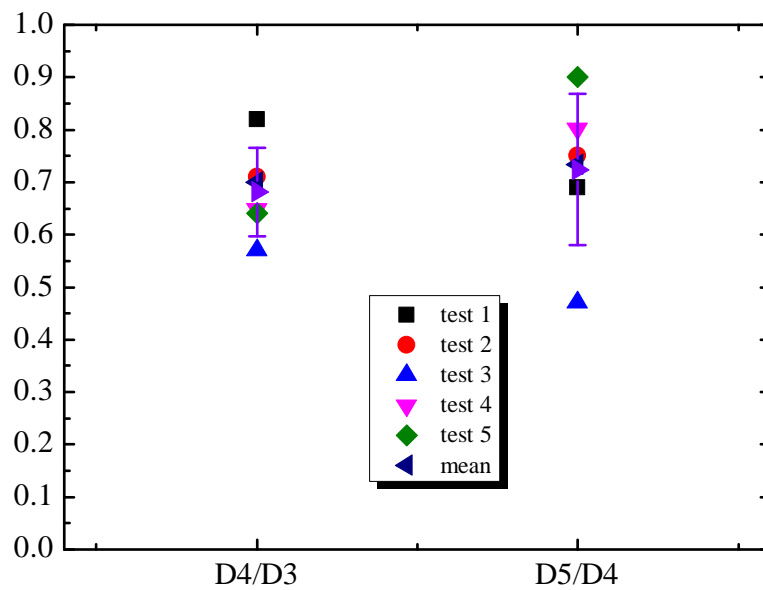
Figure 7.17   Attenuation measurements performed at 20 kV

Table 7.3   Dose attenuation measurement performed at 18 kV

	2nd	3rd	4th	5th
Mean dose per discharges [Gy]	0.42	0.18	0.11	0.08
Std [Gy]	0.11	0.06	0.016	0.013

Table 7.4   Dose attenuation measurement performed at 20 kV

	2nd	3rd	4th	5th
Mean dose per discharges [Gy]	0.40	0.22	0.15	0.10
Std [Gy]	0.09	0.045	0.03	0.03

surements performed at 18 kV is 0.74 ± 0.04, instead for the measurements performed at 20 kV is 0.7 ± 0.06.

The significant data are reported in the following tables 7.3 and 7.4.

From this tables it is possible to notice an increment of 25% of dose deposited, when the Plasma Focus device works at 20 kV.

From these experimental measurements of the efficiency of the Plasma Focus device, it can be said that voltage variations are more significant than pressure variations, that at 20 kV the Plasma Focus device is more efficient: the electron energy spectrum tails is increased by 50 keV and the dose deposited by 25%; this even though the electron beam intensity does not show significant changes (may be due to high electromagnetic noises during the current measurements performed at 20 kV). Possible future experiments will have to be conducted on the cell cultures at 20 kV, to see differences with those conducted at 18 kV, see appendix.

Appendix A

Dosimetric map of the PFMA-3 laboratory

The Plasma Focus device is a radiation source and a dosimetric map of the area around it is required, to verify the safety of the area in terms of dose to the workers and to the public.

Two experimental campaigns were performed to investigate and characterize the area around the Plasma Focus device from the dosimetric point of view.

A.1 TLD GR200

Thermoluminescencent dosimeters (TLD) GR200 were utilized [33], shown in figure A.1. These dosimeters are specific for x and gamma rays and they are provided by the ENEA Bologna Laboratory (that has the characteristic of a Secondary Standard Dosimetric Laboratory).

TLD exposure to ionizing radiation is assessed by measuring the amount of visible light emitted from a crystal in the detector when the crystal is heated. The amount of light emitted is dependent on the dose received.

Inside the dosimeters, there is a card, where two $LiF(Mg,Cu,P)$ detectors are positioned. In correspondence of the two detectors, there are the metallic filters, one is $270\,mg/cm^2$ of aluminum and the second one $520\,mg/cm^2$ of aluminum and copper. Each detectors is also filtered by $20\,mg/cm^2$ of plastic. One of the two detectors allows to measure the personal equivalent dose at $10\,mm$, $H_p(10)$, and the other one at $0.07\,mm$, $H_p(0.07)$. The filtration is symmetric, so it is indifferent the side positioning of the dosimeter. The main characteristics of the GR200 dosimeters are:

- energy range: from $10.7\,keV$ to $1.25\,MeV$
- output variation dependence in terms of $H_p(10)$ of $\pm16\%$ in the energy range
- output variation dependence in terms of $H_p(0.07)$ of $\pm4\%$ in the energy range
- output variation dependence in terms of $H_p(10)$, function of the incidence angle, of $\pm10\%$ in the energy range

Figure A.1   Thermoluminescence dosimeter for whole body for photon: GR200

- output variation dependence in terms of $H_{\mathrm{p}}(0.07)$, function of the incidence angle, of $\pm 5\%$ in the energy range
- minimum dose detectable: $0.05\,\mathrm{mSv}$
- loss of information (fading) absent, during the exposure time
- sensitiveness to other kind of radiations: blind to *alpha* radiations
- the background is calculated multiplying the Italian average value ($0.1\,\mathrm{mSv}/45\mathrm{d}$) by the exposure time.

A.2   First campaign of measurements

For the first campaign of measurements an area of $6\,\mathrm{m}$ around the Plasma Focus device was chosen. Twelve GR200 dosimeter were positioned in points of interest of this area, as shown in figure A.2.

All the dosimeters, except the ones around the vacuum chamber, are positioned at a height corresponding to the chest of an adult man (i.e., the height used for the actual dose measurements).
The dosimeters around the vacuum chamber are positioned as shown in figure A.3, at height corresponding to the location of the *pinch*.

750 discharges were accumulated for the first campaign. The working conditions are: voltage $18\,\mathrm{kV}$ and nitrogen pressure $0.45\,\mathrm{mbar}$.
The dosimeter positioned on the power supply registered the minimum dose detectable, because the x-rays produced in the *pinch* phase (see chapter 1) are attenuated by the capacitor bank, whereas the ones produced from the conversion of the electron beam impinging on the brass target are attenuated only by air.
The highest values registered were around the vacuum chamber: $100\,\mathrm{mSv}$; the vacuum chamber is made of quartz that is transparent to x-rays. This means that most of the dose

Figure A.2 First campaign of measurements: positions of the dosimeters

contribution is due to the x-rays produced during the *pinch* phase and not to those coming from the conversion of the electron beam.

The dosimeter number 39 positioned beyond the glass of the control room did not pass the minimum dose detectable: 50 μSv, so the control room is safe from the dosimetric point of view if less than 15000 discharges per year were conducted.

Other interesting values are those at locations number 36 and 47. The first is positioned at 4 m of distance from the Plasma Focus device and detected 0.10 mSv, the other one is positioned at 2 m of distance from the device and detected 0.15 mSv. They passed the limit of the minimum dose detectable for the shape of the iron shield, which covers only one side of the Plasma Focus device and has an aperture on the top. Figure A.4 shows the shield. The iron shield, 5 mm thick, is a rectangular box opened on the top, on the bottom and on the side in front of the Plasma Focus device; it is possible moving it, using two handles positioned on one side.
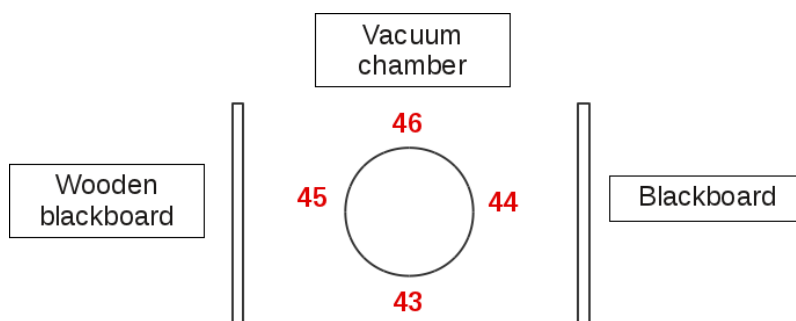
Figure A.3 First campaign of measurements: positions of the dosimeters around the vacuum chamber
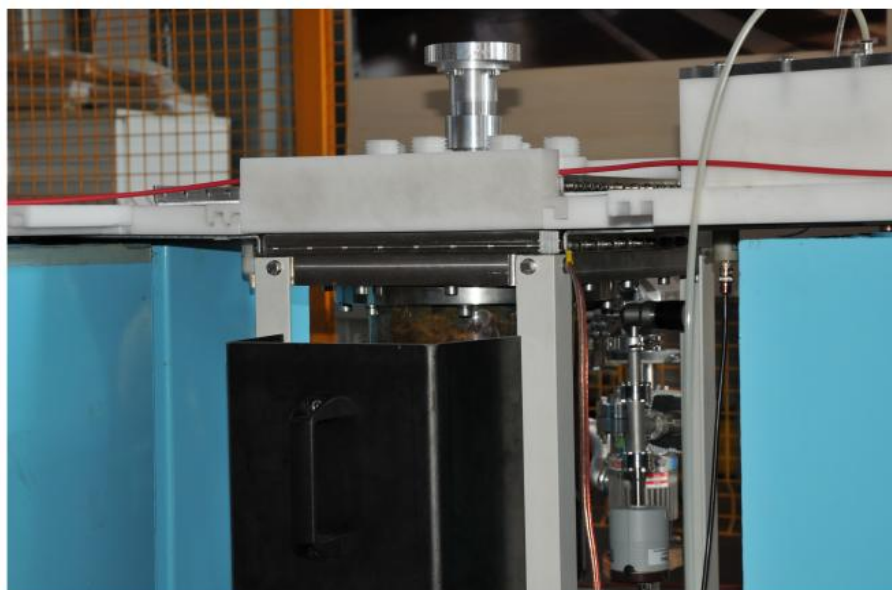
Figure A.4 Opening of the iron shield for the Plasma Focus device

A.3   Second campaign of measurements

A second campaign was conducted with ten GR200 dosimeters comparing the results with, to have further statistics. Figure A.5 presents the position of the dosimeters in the interested area.

Figure A.6 is a larger scale detail of the former.

The dosimeters are positioned again on the gate, on the wooden blackboard and on the vacuum chamber. Since in the first campaign of measurements that the 4 values measured around the vacuum chamber were the same (azimuthal symmetry), only one dosimeter, the number 36, was positioned around the vacuum chamber and a second one, the number 39, was positioned on the bottom of the vacuum chamber.

The dosimeters 40 and 41 are both at $1\,\mathrm{m}$ of distance from the Plasma Focus device: the first one is in front of the iron shield the second one in correspondence of the aperture of
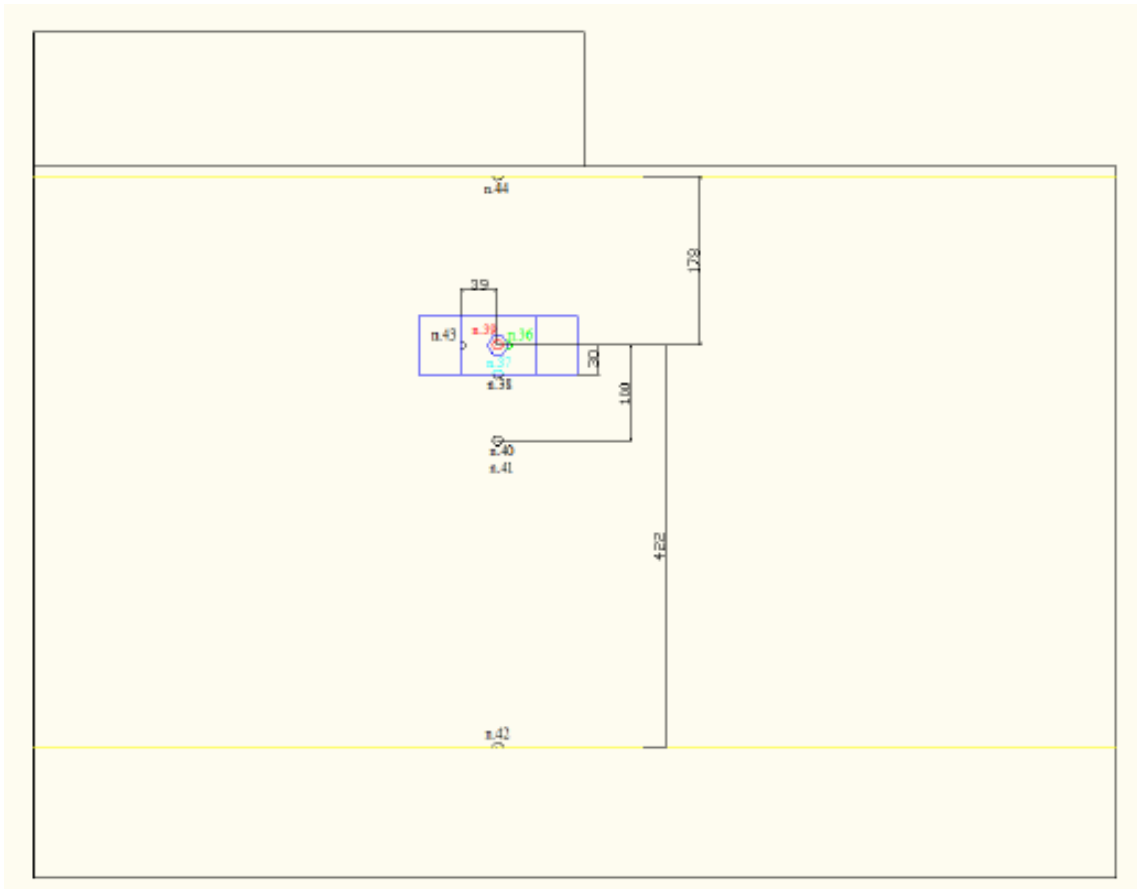
Figure A.5 Second campaign of measurements: position of the dosimeters

the shield, to verify if radiation leaks pass through the aperture.

The number 44 was positioned on the wooden blackboard at the height correspondent to the vacuum chamber to verify if the vacuum system attenuates the radiation. The number 45 is also positioned on the wooden blackboard, but at the height of the chest of an adult man.

Also for the second campaign, 750 discharges were accumulated with the same working conditions as the first campaign. Table A.1 summarizes the doses measured.

The area of the Plasma Focus device is a controlled area (it is delimited and the access is controlled). The area around the Plasma Focus enclosure is a public area, where the limit for the public is 1 mSv of effective dose. Knowing from the measurements that the highest value registered on the enclosure (at the gate) is 0.15 mSv, the maximum number of discharges allowed is 5000 per year.
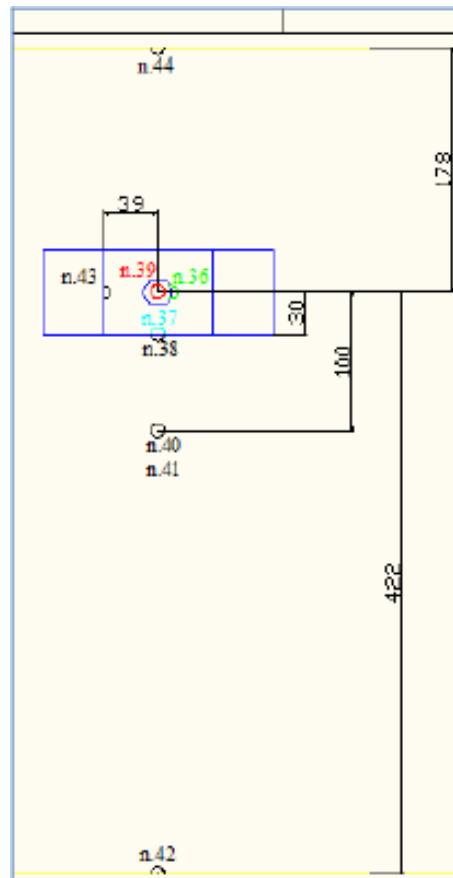
Figure A.6   Detail of the second campaign of measurements: position of the dosimeters

Table A.1   Dose detected in the second campaign of measurements

Number Dosimeter	Distance from the vacuum chamber [cm]	Dose for 750 discharges [mSv]
36	0	89.95
37	19	13.43
38	19	0.650
39	0	71.40
40	90	0.050
41	100	0.450
42	410	0.050
43	29	5.100
44	165	0.050
45	182	0.100

A.4 Dosimetric maps

To calculate the isodose levels, only the dosimeters not screened by metallic parts are considered. Doses decrease with the inverse square of the distance. Figure A.7 shows the dosimetric map for 750 discharges, without the presence of the iron shield. The isodose levels presented in steps of 20 cm until 0.2 mSv, after are at 3 and 4 m of distance.

The attenuation of the unshielded dose for 750 discharges is shown in figure A.8.

The dosimeters number 37 and number 38 are at the same distance, but the second one is positioned after the iron shield of 5 mm thickness. These two values yield an estimation of the fraction of the radiation passing through the shield

$$\frac{D_{(38)}}{D_{(37)}} = \frac{0.650}{13.43} = 0.048 \tag{A.1}$$

the efficiency of the shield is therefore 95%.
The dosimeter number 41 positioned in front of the opening of the shield received a dose of 0.45 mSv, the number 40 (shielded) only the minimum dose detectable: 0.05 mSv.
It is necessary to replace the shield with a taller one. The dosimetric map with an apt shield becomes as in figure A.9.

Figure A.10 shows the attenuation of the dose for 750 discharges, with the shield.
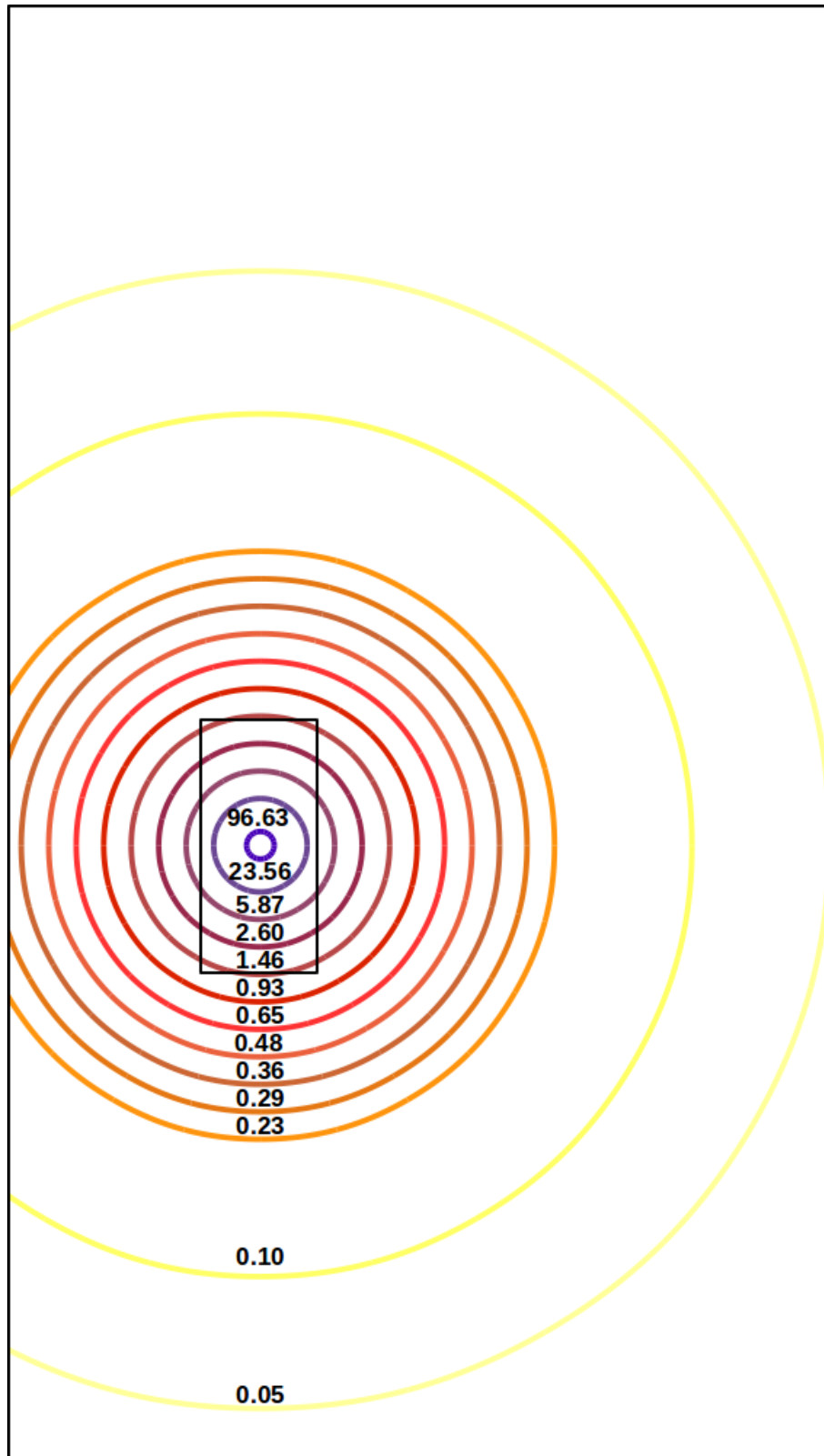
Figure A.7   Dosimetric map without the shield for 750 discharges, isodose expressed in mSv
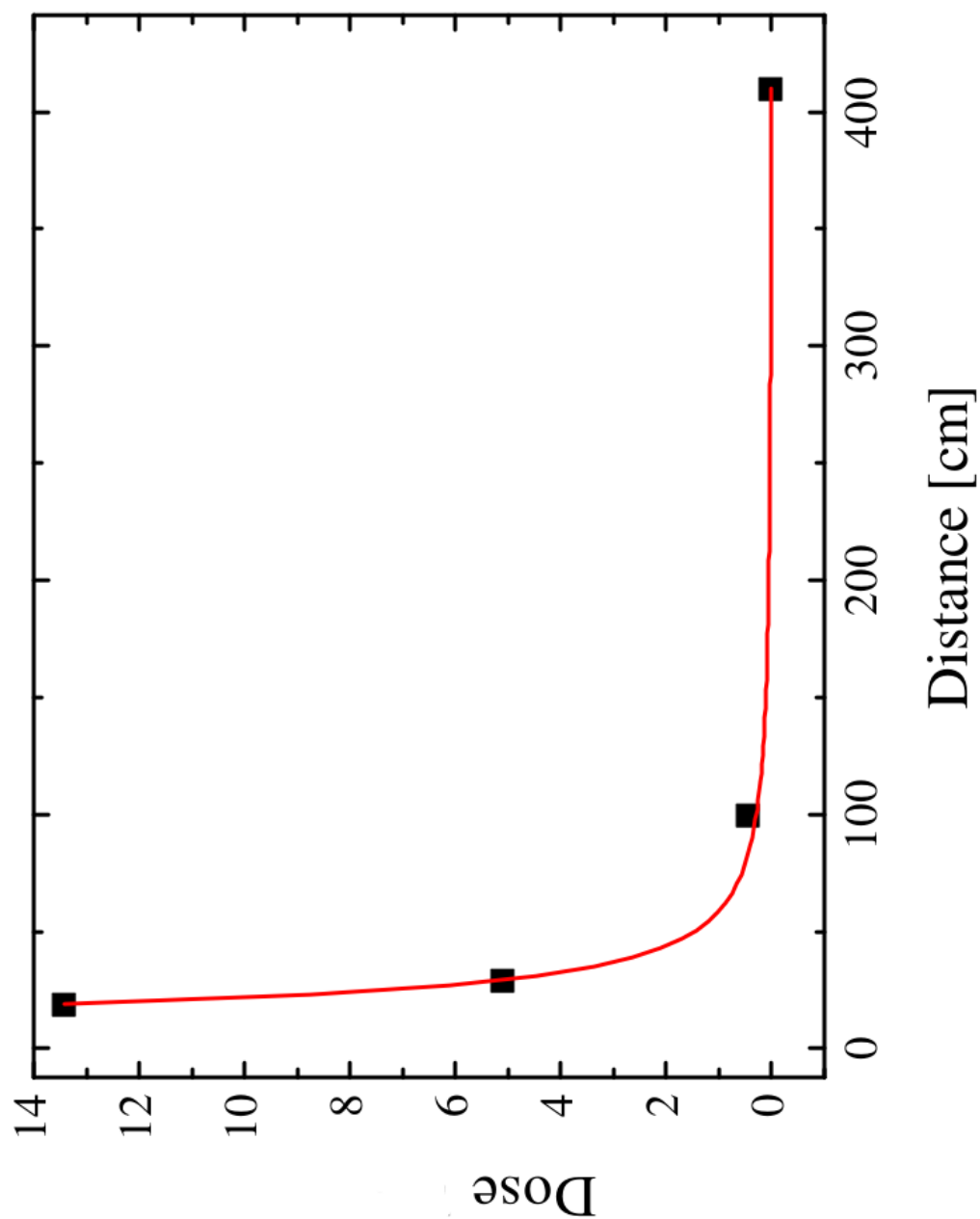
Figure A.8 Dose attenuation for 750 discharges without the presence of the shield, dose expressed in mSv
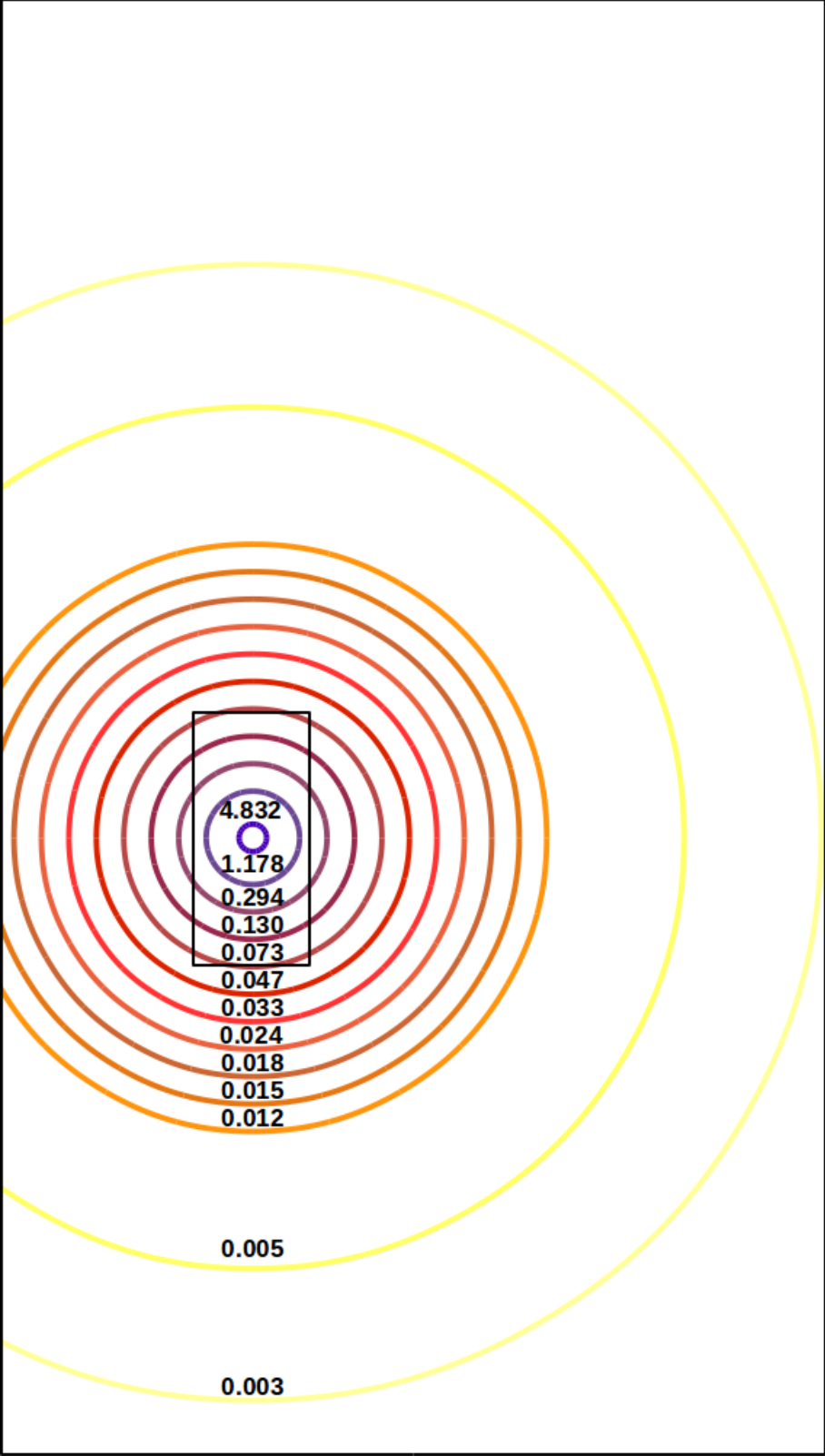
Figure A.9   Dosimetric map with the shield for 750 discharges, isodose expressed in mSv
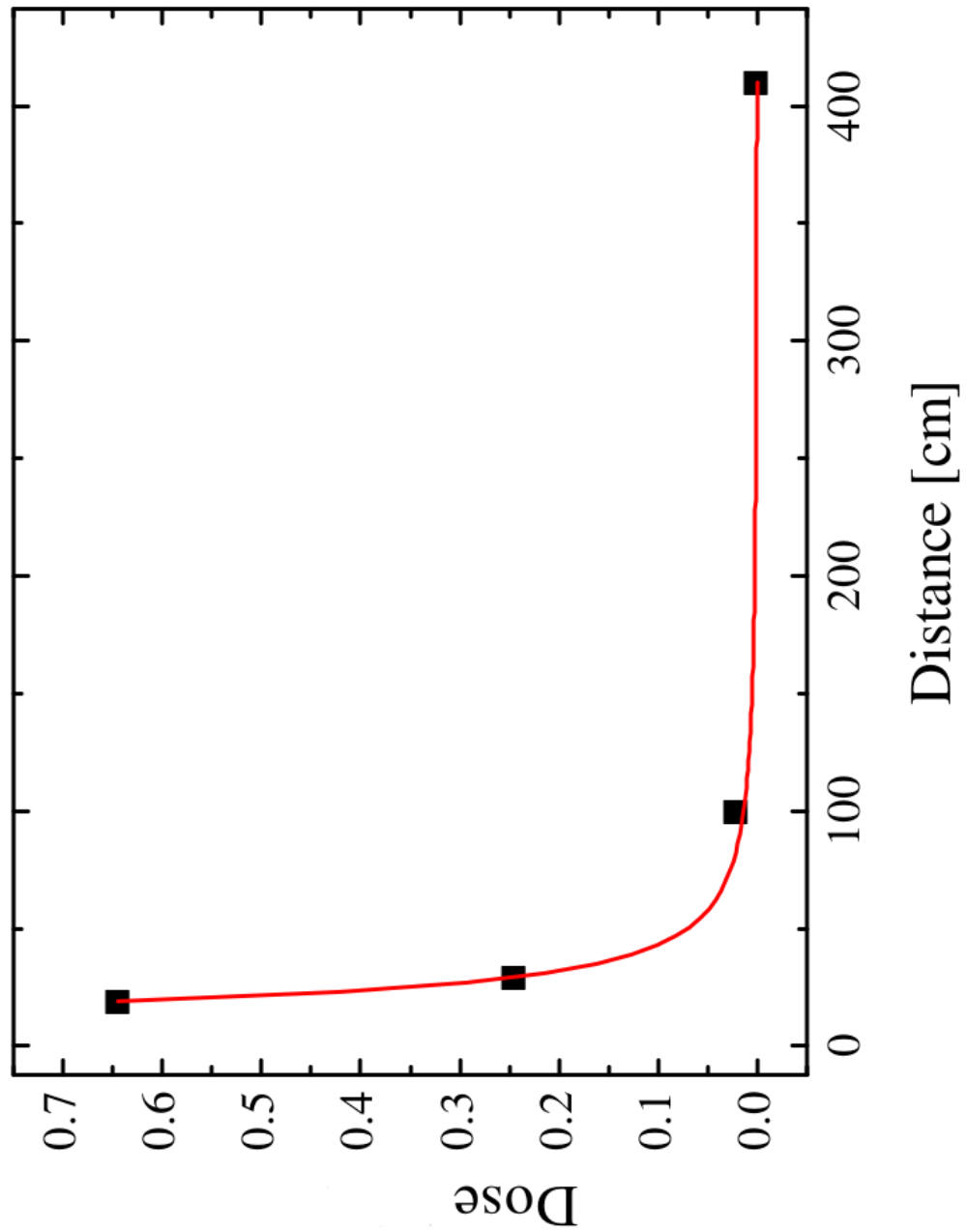
Figure A.10 Dose attenuation for 750 discharges with the presence of the shield, dose expressed in mSv

Conclusion

With the present asymmetric Plasma Focus configuration an electron beam with tails reading 300 keV was extracted by means of a drift tube 15 cm long and converted into characteristic and bremsstrahlung radiation in the interval 10-50 keV from impact with a brass target.

Measurements with the magnetic spectrometer were conducted to analyze the electron energy spectrum. A method was found to calibrate the magnetic spectrometer, based on the energy range determination.

Measurements with GAFCHROMIC® film were conducted to analyze the attenuation of the x-ray beam. GAFCHROMIC® film was identified as a convenient detector.

To analyze the radio-biological effectiveness of the PFMA-3 device, cell cultures were irradiated. In view of applying the device to cell irradiation, which is the object of the radio-biological investigation, a method for fast and reliable determination of the dose delivered was sought: to assess the dose delivered to the cells a stack of film was inserted between the brass foil (the target) and the cell holder, to measure the dose to the last GAFCHROMIC® film layer and from that infer the dose to the cell layer.

Repeating the experiment a sufficient number of times, the relationship between the dose to the extra layer and the dose to the layer immediately preceding was determined. The best configuration found was one sheet of HD-810 film, used as a filter for the electrons passing the brass target, followed by two sheets of EBT2 films, then the cell holder.

Simulations with MCNPX were conducted to study the physic involved. The very good agreement of numerical and experimental data strengthens confidence that the results of the simulations yield a reliable picture of the physics involved. The results show that the lower energy component disappears soon, reaching no farther than 0.4 mm, whereas the higher energy component, centered around 50 keV, reaches significantly deeper. Simulations, as well as the previous experimental campaign, were run with 1 mm of material, and at that depth the dose is still significant (0.5 Gy/discharge), hinting at the possibility of reaching further. Future work may investigate thicker materials to assess the maximum depth of dose penetration. Also, the simulations provide good guidance in the development of the target, insofar as the choice of material and geometry is concerned. Future choices being considered are Monte Carlo simulation of the dose deposited by the electron beam of PFMA-3 using higher Z materials such as, e.g., tungsten, and/or combinations of different thicknesses. The influence of the spectral details of the incoming electrons can be

evaluated, and hence in turns the effect of operation conditions, because of the effect they have on the electron spectrum.

Another validation of the MCNPX simulations was the experiment conducted with the Thermo-camera, that also gave good agreement. With this experiment the energy deposited on the brass target can be calculated and compared to the dose obtained from simulations with the MCNPX code. Analyses on the brass target were conducted to understand why after about 50 discharges the target breaks. After heating and loss of mass measurements, it was thought that the breaking is possibly due to the shock wave that forms during the *pinch phase.*

Several experiments were conducted also to analyze the efficiency of the PFMA-3 device under various working conditions. From these experimental measurements of the efficiency of the device, it can be said that voltage variations are more significant than pressure variations, that at 20 kV the Plasma Focus device is more efficient: tails of the electron energy spectrum is increased by 50 keV and the dose deposited by 25%; this even though the electron beam intensity does not show significant changes. Possible future experiments will have to be conducted on the cell cultures at 20 kV, to see differences with those conducted at 18 kV.

As last thing, better results are expected with an appropriate symmetric assembly.

Acknowledgments

Bibliography

[1] A. Bernard, H. Bruzzone, P. Choi, H. Chuaqui, V. Gribkov, J. Herrera, K. Hirano, A. Kreci, C. Luo, F. Mezzetti, M. Sadowski, H. Schmidt, K. Ware, C. S. Wong, and V. Zoita. Scientific status of plasma focus research. *J Moscow Phys. Soc.*, 8:93–170, 1998.

[2] V. Benzi, V. Molinari, D. Mostacci, F. Rocchi, M. Sumini, E. Angeli, F. Mezzetti, and A. Tartari. Plasma focus laboratory: Experimental setup and application. *Proc. Workshop, University of Bologna - DIENCA Laboratory of Montecuccolino, Editors: A. Barletta and M. Sumini*, pages 1–18, 2003.

[3] V. Benzi, M. Frignani, D. Mostacci, F. Rocchi, M. Sumini, and A. Tartari. Plasma focus per la produzione di energia. *Conferenza Nazionale sulla politica energetica in Italia*, 2005.

[4] M.J. Sadowski and M. Scholz. The main issues of research on dense magnetized plasmas in pf discharges. *Plasma Sources Sci. Technol.*, 17:024001–14, 2008.

[5] M. Frignani. *Simulation of Gas Breakdown and Plasma Dynamics in Plasma Focus Devices*. PhD thesis, Università degli Studi di Bologna - Dottorato in Ingegneria Nucleare - XIX ciclo, 2007.

[6] D. A. Ward and J. La T. Exon. Using rogowski coils for transient current measurements. Technical report, Engineering science and education journal, 1993.

[7] M. Sumini, A. Tartari, M. Mostacci, E. Ceccolini, F. Rocchi, G. Cucchi, M. Roson, M. Martignon, M. Ciocca, A. Facoetti, and R. Orecchia. Physical and radiobiological characterization of extremely high dose per pulse x-ray beams produced by a plasma focus device for iort. *Proc. 6th International Conference of the International Society of Intraoperative Radiation Therapy*, 53, 2010.

[8] A. Tartari, A. Da Re, F. Mezzetti, E. Angeli, and P. De Chiara. Feasibility of x-ray interstitial radiosurgery based on plasma focus device. *Nucl. Instrum. Meth. B*, 213:607–610, 2004.

[9] J. S. Vaidya, M. Baum, J. S. Tobias, S. Morgan, and D. D'Souza. The novel technique of delivering targeted intraoperative radiotherapy (targit) for early breast cancer us-

ing rogowski coils for transient current measurements. Technical report, Educational Section, European Journal of Surgical Oncology, 2002.

[10] Comsol Multiphysics. Version 4.2.

[11] E.A. Lopez, G.A. Bennett, R.R. Bartsch, J.C. Cochrane, J. R. Griego, R. D. Hicks, W. B.Hinckley, K. W. Hosack, R.J. Kasik, A. Marqueza, W.M. Parsons, W.A. Reass, and M.C. Thompson. Rail-gap switch modification and test data for the atlas capacitor bank. *Los Alamos National Laboratory*, Proc. Conference: 11th IEEE International Pulsed Power Conference Baltimore, 1997.

[12] International Specialty Products. Advanced materials group (b) GAFCHROMIC hd-810, 2005, http://www.gafchromic.com/.

[13] International Specialty Products. Advanced materials group (a) GAFCHROMIC ebt2, 2005, http://www.gafchromic.com/.

[14] R. F. Schneider, C. M. Luo, and M. J. Rhee. Compact magnetic electron energy analyzer. *Rev. Sci. Instrum.*, 56:1534, 1985.

[15] A. Patran, D. Stoenescu, R. S. Rawat, S. V. Springham, T. L. Tan, L. C. Tan, M. S. Rafique, P. Lee, and S. Lee. A magnetic electron analyzer for plasma focus electron energy distribution studies. *J. Fusion Energ.*, 25:57, 2006.

[16] E. Ceccolini, F. Rocchi, D. Mostacci, M. Sumini, and A. Tartari. A range-based method to calibrate a magnetic spectrometer measuring the energy spectrum of the backward electron beam of a plasma focus. *Rev. Sci. Instrum*, 85:0851031–7, 2011.

[17] I.Y. Dodidn and N.J. Fisch. Correction to the alfvèn-lawson criterion for relativistic electron beams. *Phys. Plasmas*, 13:103104–7, 2006.

[18] J.R. Davies. Magnetic-field-limited currents. *Phys. Rev. E*, 68:037501–4, 2003.

[19] M. J. Berger, J. S. Coursey, M. A. Zucker, and J. Chang. Estar, pstar, and astar: Computer programs for calculating stopping-power and range tables for electrons, protons, and helium ions (national institute of standards and technology), 2005, http://physics.nist.gov/PhysRefData/Star/Text/appendix.html.

[20] A. Cole. Adsorption of 20-eV to 50000-eV electron beams in air and plastic. *Radiat. Res.*, 38:7–33, 1969.

[21] J.C. Ashley. Inelastic interactions of low-energy electrons with organic solids: Simple formulae for mean free paths and stopping powers. *IEEE Trans. Nucl. Sci.*, NS-27:1453–8, 1980.

[22] T. Zhenyu, X. Yueyuan, Z. Mingwen, L. Xiangdong, L. Feng, H. Boda, and J. Yanju. Electron stopping power and mean free path in organic compounds over the energy range of $20 - 10000$ eV. *Nucl. Instrum. Methods Phys. B*, 222:27–43, 2004.

[23] National Institute of Standard Technology NIST Database. United states, http://www.nist.gov/index.html.

[24] S. Devic, J. Seuntjens, G. Hegyi, E.B. Podgorsak, C.G. Soares, A.S. Kirov, I. Ali, J.F. Williamson, and A. Elizondo. Dosimetric properties of improved gafchromic films for seven different digitizers. *Med. Phys.*, 31:2392–401, 2004.

[25] B. Arjomandy, R. Tailor, A. Anand, N. Sahoo, M. Gillin, K. Prado, and MT. Vicic. Energy dependence and dose response of gafchromic ebt2 film over a wide range of photon, electron, and proton beam energies. *Med. Phys.*, 37:1942–7, 2010.

[26] E. Ceccolini, F. Rocchi, D. Mostacci, M. Sumini, and A. Tartari. EBT2 dosimetry of X-rays produced by the electron beam from PFMA-3, a plasma focus for medical applications. *arXiv:1112.2198v1*, 1112.2198v1:1112.2198v1, 2011.

[27] CRXO Center for X-Ray Optics. X-ray interaction with matter, 2010, Filter Transmission Website.

[28] A. Virelli, E. Gavoci, I. Zironi, E. Cecccolini, F. Rocchi, M. Sumini, E. Belligotti, and G. Castellani. A system biology approach to ionizing radiation response by mammalian cell lines. *Sysbiohealth Symposium*, Proc. Conference: System Medicine Interfacing Physics, Mathematics and Medicine, edited by G. Castellani, C. Franceschi, L. Milanesi and D. Remondini:99–104, 2011.

[29] D. B. Pelowitz and ed. Mcnpx user's manual. *Version 2.60*, LA-CP-07-1473, April 2008.

[30] E. Ceccolini, F. Rocchi, D. Mostacci, M. Sumini, and A. Tartari. Monte Carlo Simulation of the Conversion X-Rays from the Electron Beam of PFMA-3. *AIP Proc. Conference: Conference on Applications of Nuclear Techniques Crete, Greece June 12-18*, 79:1412, 2011.

[31] A. L. Schwarz, R.A. Schwarz, and L.L. Carter. Mcnp/mcnpx visual editor computer code manual for vised. *Version 22S*, February 2008.

[32] S.Mannucci, D. Mostacci, F. Rocchi, M. Sumini, E. Angeli, and A. Tartari. Thermal flux analysis of the pfma-1 device, brussels, belgium. *European Nuclear Conference*, 16-20, September 2007.

[33] E. Fantuzzi, F. Mariotti, B. Morelli, and G. Uleri. The implementation in routine of enea new personal photon dosemeter. *Radiat. Prot. Dosimet.*, 120:278–282, 2006.

[34] International Specialty Products. Advanced materials group (a) gafchromic ebt2. Technical report, 1361 Alps Road Wayne New Jersey US, 1999.

Curriculum Vitae

Education

- 09/2005 - 03/2008: Master Degree Energy Engineering (105/100), University of Bologna, Italy
  Thesis title: "Use of radiochromic (EBT) and radiographic (EDR2) films for quality assurance in brachytherapy and external radiotherapy", Associate to Institute Supèrieur Industriel de Bruxelles (ISIB)
  Advisor: Prof. Domiziano Mostacci, Co-Advisors: Prof. Isabelle Gerardy

- 09/2002 - 03/2006: Bachelor Degree Energy Engineering (95/100), University of Bologna, Italy
  Thesis title: "Variabilità temporale di radiotraccianti naturali atmosferici",
  Advisor: Prof. Domiziano Mostacci

- 09/1997 - 07/2002: Italian secondary school in classical studies (89/100), "Liceo Classico Giulio Cesare", Rimini, Italy

Titles

- July 2008: Professional qualification to the Engineering Profession

- 2011: Qualified Expert in Radiation Protection, with the second (i.e. intermediate) level

Schools

- August 20th-31th, 2007: Nuclear Chemistry Summer School "Aachen University of Applied Sciences Julich Division", Germany

- March 01st-14th, 2009: Erasmus Intensive Program Project (IP), ICARO, Intensive Course on Accelerator and Reactor Operation, Lisbon, Portugal

- July 08th-10th, 2009: International Summer School: Criteria and Approaches for Radioactive waste Management and Nuclear Decommissioning, Milano and Ispra, Italy

Courses and workshops

- May 26th-28th, 2008: CHERNE 4th Workshop on European Collaboration for Higher Education and Research in Nuclear Engineering and Radiological Protection, Favignana, Italy, article presented: E. Ceccolini, I. Gerardy, J. Ròdenas, M. Van Dycke, S. Gallardo, D. Mostacci, MCNP modelling of vaginal and uterine applicators used in intracavitary brachytherapy and comparison with radiochromic film measurements
- April, 2009: Intensive Course: Comsol Multiphysics, Brescia, Italy
- June 01st-02nd, 2009: International VELLA Thematic Workshop "Introduction to the Design Issues of LFR", Nuclear Laboratory of Montecuccolino, University of Bologna, Italy
- February, 2010: Course "Protection against natural radiation", Valencia, Spain
- March, 2010: Experimental Plasma Focus (PF-1000) campaigns, Institute of Plasma Physics and Laser Microfusion (IFPILM), Warsaw, Poland
- June 12th-18th, 2011: 11th International Conference on Applications of Nuclear Techniques, article presented: E. Ceccolini, F. Rocchi, D. Mostacci, M. Sumini, A. Tartari, Monte Carlo Simulation of the Conversion XÂŋ-Rays from the Electron Beam of PFMA-3, Crete, Greece
- November 04th-05th, 2011: Conference "Optical acceleration of ions and perspective for biomedicine", Bologna, Italia
- December 14th-15th, 2011: Conference "Sysbiohealth Symposium", Bologna, Italy

Publications

- E. Ceccolini, I. Gerardy, J. Ròdenas, M. Van Dycke, S. Gallardo, D. Mostacci, MCNP modelling of vaginal and uterine applicators used in intracavitary brachytherapy and comparison with radiochromic film measurements, Radiation Effect and Defects in Solids, 319-324
- I. Gerardy, J. Ròdenas, M. van Dycke, S. Gallardo, Elisa Ceccolini, Dosimetric characterization of a brachytherapy applicator using MCNP5 modelisation and in-phantom measurements, Applied Radiation and Isotopes 68 (2010) 735-737
- J. Ròdenas, S. Gallardo, E. Ceccolini, W. Hansen, Validation of the Monte Carlo model developed to estimate in the neutron activation of stainless steel in a nuclear reactor, presentato Joint International Conference on Supercomputing in Nuclear Applications and Monte Carlo, 2010 (SNA + MC2010), October, Japan
- E. Ceccolini, F. Rocchi, D. Mostacci, M. Sumini, and A. Tartari, A range-based method to calibrate a magnetic spectrometer measuring the energy spectrum of the backward electron beam of a plasma focus, Review of scientific Instruments, 82 (2011), 085103
- E. Ceccolini, F. Rocchi, D. Mostacci, M. Sumini, A. Tartari, Monte Carlo Simulation of the Conversion X-Rays from the Electron Beam of PFMA-3, AIP Proceeding 11th International Conference on Applications of Nuclear Techniques, 2011, Crete, Greece

- A. Virelli, E. Gavoci, I. Zironi, E. Cecccolini, F. Rocchi, M. Sumini, E. Belligotti, G. Castellani, A system Biology Approach to Ionizing Radiation Response by mammalian cell lines, Sysbiohealth Symposium 2011, 14-15 December 2011, Bologna. Conference proceedings: System Medicine Interfacing Physics, Mathematics and Medicine, edited by G. Castellani, C. Franceschi, L. Milanesi and D. Remondini, pp. 99-104

Research periods abroad

- 01/09/2007 - 01/03/2008: Institute Supèrieur Industriel de Bruxelles (ISIB), Belgium, for the master degree thesis.
- 01/12/2009 - 28/02/2010: Chemical and Nuclear Department in the University of Valencia (UPV), Spain (MCNP code), Ph.D. period
- 01/04/2011 - 01/07/2011: Physical Department in the University of Coimbra, Portugal (Geant code), Ph.D. period

Teaching experiences

- 2004/2005: Teaching assistantship for the course "Rapioprotezione L" held by Prof. Domiziano Mostacci, University of Bologna, Italy.